We may not be master of our daily
work, but we are at least master
of the heart in which we do it.

(Hugh Black)

THE BEHAVIOUR OF DIMPLED DROPS

Tom Wairegi

Department of Chemical Engineering

McGill University

Montreal, Canada

Presented in Partial Fulfillment of M.Eng. Requirement

ACKNOWLEDGEMENT

The assistance of Professor J.R. Grace in the experiments and his thoughtful guidance in all aspects of this work are sincerely appreciated. May his shadow never grow smaller.

Also, discussions with Professor R.G. Cox have been very encouraging and useful.

ABSTRACT

There are many parallels between the behaviour of gas or vapour bubbles, solid particles, and liquid drops. It has been found only recently that under certain circumstances liquid drops may take up shapes very much like spherical-capped bubbles. This area has received little attention in the past. It may be important as a limiting case for drops in liquid-liquid extractors and for separators used with distillation columns.

The motion of drops of four grades of silicone oil, paraffin oil, o-diethyl phthalate, o-dichlorobenzene, 1.2 - dichloroethane, and 1,1,1- trichloroethane through a 70% by weight aqueous sugar solution has been studied. Three theoretical and one semi-empirical approach have been presented for quantitatively determining the terminal velocity of these drops. The first two approaches assume creeping flow outside and inside a drop. The third approach uses semi-empirical relations, and the fourth assumes potential flow outside and inviscid motion inside a drop. The theoretical predictions are compared with the experimental results. The results show that the creeping flow analysis predicts too strong a dependence of velocity on equivalent diameter, while the potential flow approach leads to results which agree very well with the experimental data. The semi-empirical approach turns out to be unfruitful.

Several different shapes have been distinguished. it has been noted that a change in drag is always preceded by a change in shape. The analysis is further complicated by the occurrence of skirts for larger drops. Waves and skirt instability have been observed under certain conditions. A crude model to predict the length of a skirt has been given. The predicted and the measured length of skirt show poor agreement. However, it appears that the crude model contains the main physical features consistent with the actual case. Conditions for the onset of skirt formation are presented graphically and a qualitative model has been proposed to account for the formation and growth of skirts.

LIST OF FIGURES

LIST OF TABLES

CONTENTS

CHAPTER I

INTRODUCTION

1.0 General

Two phase flows are of great importance in many branches of Engineering and Physics. For example, in liquid-liquid extraction, boiling, sedimentation, distillation and in meteorology two distinct phases, a continuous and a dispersed phase, are always present. The dispersed phase may be in the form of gas or vapour bubbles, solid particles, or liquid drops. A common aim is to increase the interfacial area in order to maximize the rate of heat or mass transfer. The flow patterns in both phases are important in all these cases for two reasons. Firstly, the capacity of the equipment depends on the terminal velocity of the dispersed phase. Secondly, the convective rate of heat or mass transfer between the dispersed and continuous phases is determined by the fluid flow inside and around the dispersed particles.

The analysis of the nature of flow for dispersed flows of bubbles, drops and particles is a hydrodynamical problem which has been under investigation since the time of Stokes (1850). The problem is complex and many assumptions have to be made in order to devise analytical solutions. In the case of solid particles, sufficient assumptions have been established to bring solutions valid at sufficiently low Reynolds numbers for certain shapes. However, the problem becomes more complicated with bubbles and with drops. This is due to the fact that there is internal circulation and deformability for bubbles and drops. Moreover, for liquid drops the dispersed phase fluid generally has appreciable density and viscosity which affect the flow patterns.

1.1 Short Review of Some Early Work on Liquid Drops

When the size of a liquid drop rising or falling in another liquid is sufficiently small, interfacial tension forces predominate and both the hydrostatic and hydrodynamic forces are negligible in the determination of the shape of the drop. In such cases, the drop assumes a spherical shape or it is distorted to such a small degree that its accentricity is not observable. Drops of this shape have been investigated quite thoroughly. Analytical solutions were developed by Rybczinski (1911) and independently by Hadamard (1911) for creeping flow in both phases and a perfectly mobile interface. Boussinesq (1913) extended this treatment by postulating that a thin layer of higher viscosity exists near a liquid interface. This assumption of the existence of surface viscosity has generally been accepted, although its importance for liquid drops and gas bubbles is slight, Harper, Moore and Pearson (1967). In most systems of practical importance, mobility of the interface is impeded to a greater or lesser extent by surface tension gradients due to the presence of surface active impurities and the shear stress at the interface.

In many cases, the interface is then totally rigid and the fluid particle acts like a solid sphere. Intermediate cases where the interface is partially immobilized have been treated by Savic (1953).

As the size of the drop is increased, the dynamic forces due to the flow of the external and internal liquids begin to affect the shape of the drop. The shape changes from spherical to nearly oblate ellipsoidal, with the amount of deformation depending on the physical properties of the two liquids. Drops of this particular shape have also been studied. Their original treatment was due to Oberbeck (1876). Saito (1913) showed that a prolate shape is possible if $\rho \ll \rho'$ and $\mu \ll \mu'$, e.g. for liquid metal drops falling through air, Hughes and Gilliland (1952).

In some cases, again depending on the physical properties of the two liquids, the shape does not change from spherical to ellipsoidal. Instead, as the drop size is increased above some critical value, a dimple begins to form at the rear of the drop. So far as we know, this type of drop has received little attention up to the present time. However, it may be important as a limiting case for drops in industrial processes mentioned earlier. This study would also help to resolve certain problems associated with the behaviour of spherical-cap bubbles in liquids and in fluidized beds. For example, it is very difficult to visualize the internal flow patterns for bubbles, but flow visualization in large liquid drops is feasible.

CHAPTER 2

PREVIOUS WORK ON DIMPLED DROPS

2.0 The Occurrence of Dimpled Drops

Dimpled drops have received very little study by other workers. Garner *et al.* (1957) reported this shape for chloroform drops descending through a continuous phase of glycerine. It was observed that as the size of the drop was increased, the drop remained spherical until a Reynolds number of about 0.1 was reached. After this, the rear of the drop began to flatten. For still higher Reynolds numbers, the rear surface was found to fold inwards causing an indentation or cavity at the upper surface of the drop. It was concluded that the distortion of drops at relatively low Reynolds numbers (of order 1) depends on the relative changes in the outside hydrodynamic pressure and the inside pressure due to circulation.

While carrying out investigations of the nature of flow and shape of drops in non-Newtonian liquids, Fararoui and Kintner (1961) found it desirable to compare the shapes of large drops moving through non-Newtonian liquids with drops of similar size moving in comparable Newtonian liquids. In the latter systems with a nitrobenzene-tetrachloroethane mixture as the dispersed phase and corn syrup as the continuous liquid, they obtained a series of photographs of dimpled drops. These drops had sphere equivalent diameters ranging from 0.46 cm to 5.22 cm. For drops falling through non-Newtonian liquids, they noted that as the drop size was increased to some critical value, the shape might change from tear-drop shape to one with a concave upper surface.

Dimpled drops have also been reported by Shoemaker and Chazal (1969) for 2-butanone, acetone, hexane, 2-ethyl-1-hexanol, and 145 cP paraffin oil drops dispersed in glycerol. Using paraffin oil as the continuous phase, dimples were observed also with two dispersed liquids: glycerol and water. A chamber 71.6 cm high and 26.5 cm in diameter was used in order to avoid end and wall effects. Published photographs of the drops show the dimples, stable skirts attached at the edge of the concave region, and ragged skirts (not axially symmetrical).. The assymmetry was said to have been due to vortex shedding.

2.1 Internal Circulation and Dimple Formation

Garner et al. (1957) also investigated the onset of internal circulation and its effect on dimple formation for small drops falling through Newtonian liquids. With carbon tetrachloride dispersed in glycerol, it was found that internal circulation begins at Reynolds numbers as low as 3×10^{-4} to 10^{-3} (diameters ranging from 10^{-1} cm to 3×10^{-3} cm). However, the dimple at the upper surface of the drop did not form until the Reynolds number was greater than about 0.1. Their explanation for this was that for smaller drops, the "Hydrodynamic suction" is very low and there is no distortion. With increasing drop size, the outside hydrodynamic suction and the inside circulation pressure change in accordance with the Hadamard (1911) solution so that the excess pressure (pressure inside less pressure outside) remains equal to $2\sigma/R_o$, i.e. $P_{hs} - P_{hd} = 2\sigma/R_o$. Here σ is the interfacial tension, R_o is the local radius of curvature at the rear of the drop, Phs is the hydrostatic pressure, and Phd is the hydrodynamic suction.

At Reynolds number greater than 0.1, the hydrodynamic pressure progressively increases over that indicated by the excess pressure $2\sigma/R_o$. Hence, the radius of curvature at the rear stagnation point must increase to maintain the pressure balance as the drop becomes increasingly flattened at the rear surface. As the Reynolds number is increased even more, the excess pressure becomes negative and the drop starts to become concave. To back up their explanation, Garner et al. (1957) plotted Reynolds number against $2\sigma/R_o$ for each drop of carbon tetrachloride falling through glycerol. The results are consistent with their proposed explanation.

Shoemaker and Chazal (1969) suggested that the formation of dimples and skirts was due to stable vortices in the wake of the drop and to internal circulation. Their reasoning was based on the two-dimensional bubble wake studies of Collins (1966) and Crabtree and Bridgwater (1967), and the three-dimensional spherical drop wake studies of Magarvey and

MacLatchey (1968). Shoemaker and Chazal also postulated that the toroidal circulation in the wake of a large drop can increase the stability of the dimple or skirt, significantly delaying the onset of vortex shedding. Skirt formation has only been observed with a continuous phase of high viscosity.

2.2 Interaction and Coalescence Between Dimpled Drops

The interaction between dimpled drops has been observed to be different from the behaviour of spherical drops by Shoemaker and Chazal (1969). If two drops are formed a fraction of a second apart with the second drop slightly larger, they will rise independently until the second drop reaches the circulation region below the first drop. The lower drop then begins to lengthen as it is accelerated into the expanding dimple of the upper drop. This is clearly shown in their photographs of 2-butanone drops rising through glycerol. Some of the photographs also indicate that the overtaking drop elongates considerably as it enters the skirted region of the leading drop. Coalescence of two such drops was also demonstrated in their photographs. This process of coalescence is similar to that shown by bubbles in fluidized beds as noted by Clift and Grace (1970).

CHAPTER 3

EXPERIMENTAL EQUIPMENT AND PROCEDURE

3.0 Experimental Equipment

The equipment is shown schematically in Figs. 3.0 and 3.1. It includes a large tank, A, a dispersion tank, B, and a leakage control gate, F. The system of drop injection pipes, P, valves, V, and a compressed air cylinder, C, are also shown.

3.1 Large Tank

The tank of height 200 cm and cross-section 122 x 122 cm, constructed of cast iron framework with plexiglass windows, permits visual and photographic observation. The supporting framework is necessary in view of the capacity of the tank and the hydrostatic head of the liquid filling the tank. With such a large tank, experiments can be conducted with wall effects negligible. In the inside of the tank, the metal framework has safety-green paint applied in order to prevent rusting or reaction with liquids filling the tank.

3.1.1 Dispersion Tank

Situated beside the large tank is a cylindrical dispersing vessel of capacity 25.450 cm^3, made of stainless steel and with cast iron legs. The vessel can withstand pressures of at least 60 psig. On the upper part of the vessel there are three pipes, each fitted with a valve. One is used to introduce the liquid into the vessel; the second allows compressed air into the vessel, while the third serves to release the compressed air at the completion of the experiment.

3.1.2 Drop Injection Pipes

Six short pipes of inside diameter 3/8", 5/8", 3/4", 1", 1 1/2" and 2" are fitted at the bottom of the large tank in order to produce drops of varying sizes. Three of these pipes are fixed at an angle of 135^{o} to the vertical by means of elbows in order to minimize leakage due to the displacement of the light discontinuous liquid by the more dense continuous liquid. These pipes are also protected with safety-green paint.

3.1.3 Leakage-Control Gate

The leakage-control gate was constructed of plexiglass. A sliding plexiglass gate ($\frac{1}{4}$" thick) was attached to the upper surface of a rectangular frame. The gate is controlled by a bimba air cylinder and energised through a double-stroke solenoid valve.

3.1.4 System Connecting the Dispersion Tank to the Large Tank

This consists of a pipe of 3/8" I.D. leading from the bottom of the dispersion tank. The pipe is made of cast iron. Fitted onto it are a relief valve, a check valve, and a length of transparent plastic tubing. The release valve is made of cast iron and requires a maximum pressure of 50 psig before opening automatically. With judicious setting of this valve, it is possible to generate reproducible drops of a desired size. The check valve serves to prevent the continuous liquid from running out of the tank; the transparent plastic tubing enables visualization of the dispersed liquid during drop generation. The 3/8" pipe is made so that it can easily be connected to any of the six injection pipes at the base of the large tank.

3.2 Technique for Photographing Liquid Drops

The photographic technique is based upon backlighting of the field of interest through the plexiglass window. A white translucent sheet of paper flush with the outer back surface of the column diffuses light from a pair of flood lights. This gives each drop a dark outline sharply silhouetted against the bright background. The flood lamps were kept far enough away to minimize heating of the liquid in the tank.

Motion pictures of the rising drops were taken using 16 mm Tri-X or Plus-X reversal film with a Bolex reflex cine camera. Various lens and filming speeds were employed. In order to minimize distorted images caused by shadows and reflections, the camera was aligned at right angles to the face of the tank, and at a distance of 20 feet.

ARRANGEMENT OF EXPERIMENTAL APPARATUS

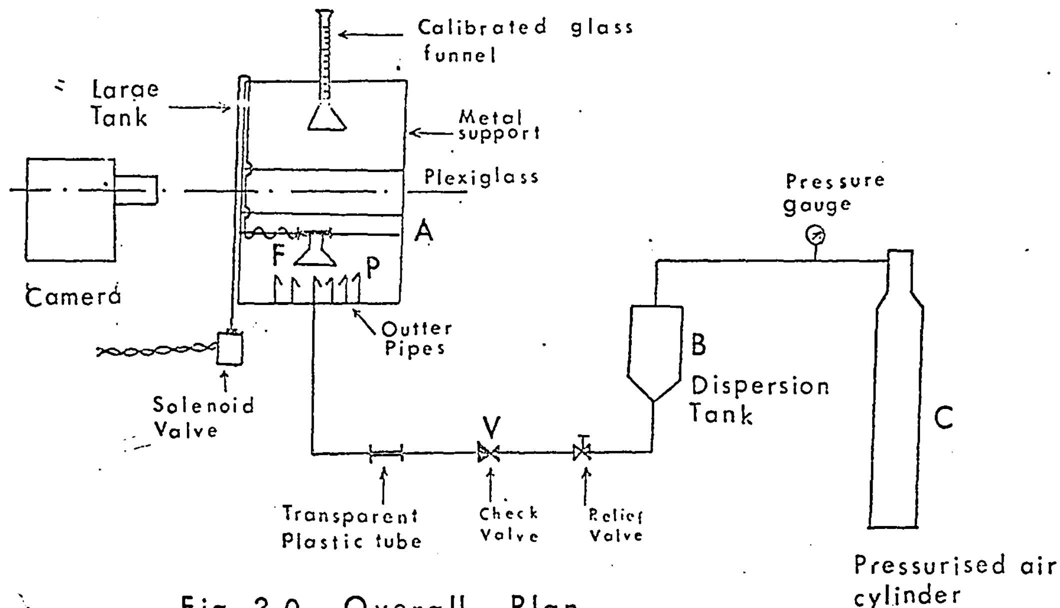

Fig. 3.0 Overall Plan

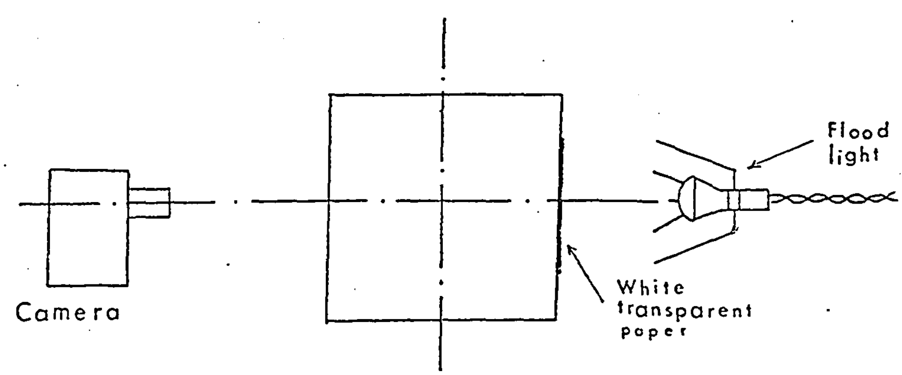

Fig. 3.1 Side View

3.3 Measuring Techniques

The various methods employed in the measurement of volume, velocity, shape of the liquid drops, and the physical properties of the liquids are discussed in the following sections.

3.3.1 Measurement of Drop Volume

The volume of each drop was measured by trapping it as it rose to the top of the large tank in a calibrated glass funnel. Two sizes of glass funnels were available with stems of internal cross-sectional area 19.64 cm^2 and 3.14 cm^2. The former was found convenient for large drops while the latter proved more accurate with smaller drops. The level of the liquid in the funnel was recorded before and after collecting the drop. From these two levels, the displacement, and hence the volume of the drop, was calculated. The level of liquid in the collecting funnel could be controlled by sucking liquid off with a press-ball vacuum pump. In this way, the dispersed liquid was recovered for re-use. The liquids were mutually saturated and their physical properties are given in Table A. A 70% by weight aqueous sugar solution was used as the continuous phase in all the experiments reported here.

3.3.2 Measurement of Drop Velocities

Two methods of determining drop velocities were employed. One was to measure the time taken by the drop to move through a height of 45.7 cm with a stopwatch with a ten second sweep. To avoid end effects, the drops were allowed to rise nearly 100 cm before the 0.1 sec stopwatch was started. The upper extreme of the timing section was about 30 cm below the top surface of the continuous liquid in the test tank. The second method of measuring velocity was to count the number of frames from the cine-film for a known filming rate for the drop to traverse a known distance.

3.3.3 Measurement of Drop Shape

The outline of the drop as seen in the films was drawn on transparent paper where the film had been projected onto a horizontal surface using mirrors. For liquids of high viscosity moving through liquids of low viscosity, a different system* comprised of mirrors was employed. From

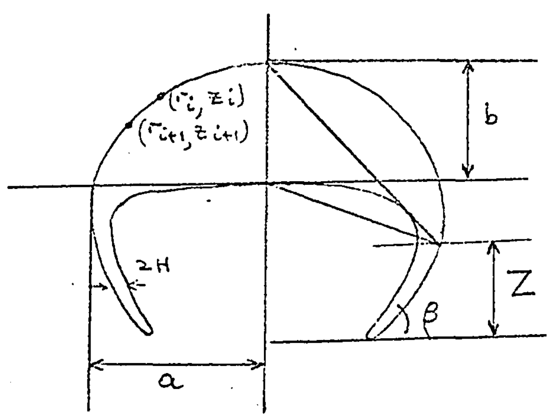

Fig.3.2. Dimensions of Interest

*This consisted of a set of two adjustable mirrors and spotlights. These were introduced into the tank. In this way, it is possible to photograph the same drop from two viewpoints simultaneously as it moves through the continuous liquid.

each trace, the shape and dimensions of the drop were determined. The dimensions of interest (Fig. 3.2), included the semi-major and -minor axes, the length of the skirt, the radius of curvature at the skirt interface, and the coordinates of different points on the projected boundary of the drop.

3.4 Measurement of the Liquid Physical Properties

The experiments were carried out at temperatures varying from 24°C to 30°C. Measurements of density, viscosity, interfacial tension, and refractive index were performed as a function of temperature over the range 18°C — 40°C. The results for the liquids used are plotted in Figs. 3.4.1 - 3.4.4., for viscosity. The density, interfacial tension, and refractive indices were found to be very weak functions of temperature.

The density was determined with calibrated hydrometers, and the interfacial tension was measured by means of a ring tensiomat. The two phases were completely saturated before the measurements were taken. A Brookfield synchroelectric rotational viscometer and a constant temperature bath with cannon-fenske capillary viscometers were used to measure the viscosity of the liquids. The refractive index was determined by using a Zeiss Refractometer with a temperature controlling device consisting of a thermometer and a Haake water-jacket.

3.5 Procedure

The experimental procedure was as follows:
The Large tank was filled with about 8000 lb of aqueous sugar solution which contained 70% sugar by weight. 200 gm of hyamine (Dodecylmethylbenzyl-trimethylammoniumchloride) were dispersed in the solution in order to prevent bacterial growth.

The dispersion vessel was half-filled with the liquid to be dispersed. This liquid had already been saturated with the continuous liquid by stirring a 50:50 mixture of the two liquids and then leaving it to settle for 24 hours. A pressure of 10-15 psig was then applied from the compressed air cylinder to the dispersion vessel. The stationary photographic equipment, the lighting system, the stopwatch, and the calibrated collecting funnel (supported from the top of the tank) were then positioned and prepared for use. After an aluminum block had been photographed to provide a frame of reference, drops of the required size were injected by a controlled opening of the relief valve. After the drop had been filmed, its volume was read from the collecting funnel and recorded. The above procedure was repeated for various sizes of drops, each time making sure that the accumulation of the dispersed liquid in the collecting funnel was not excessive.

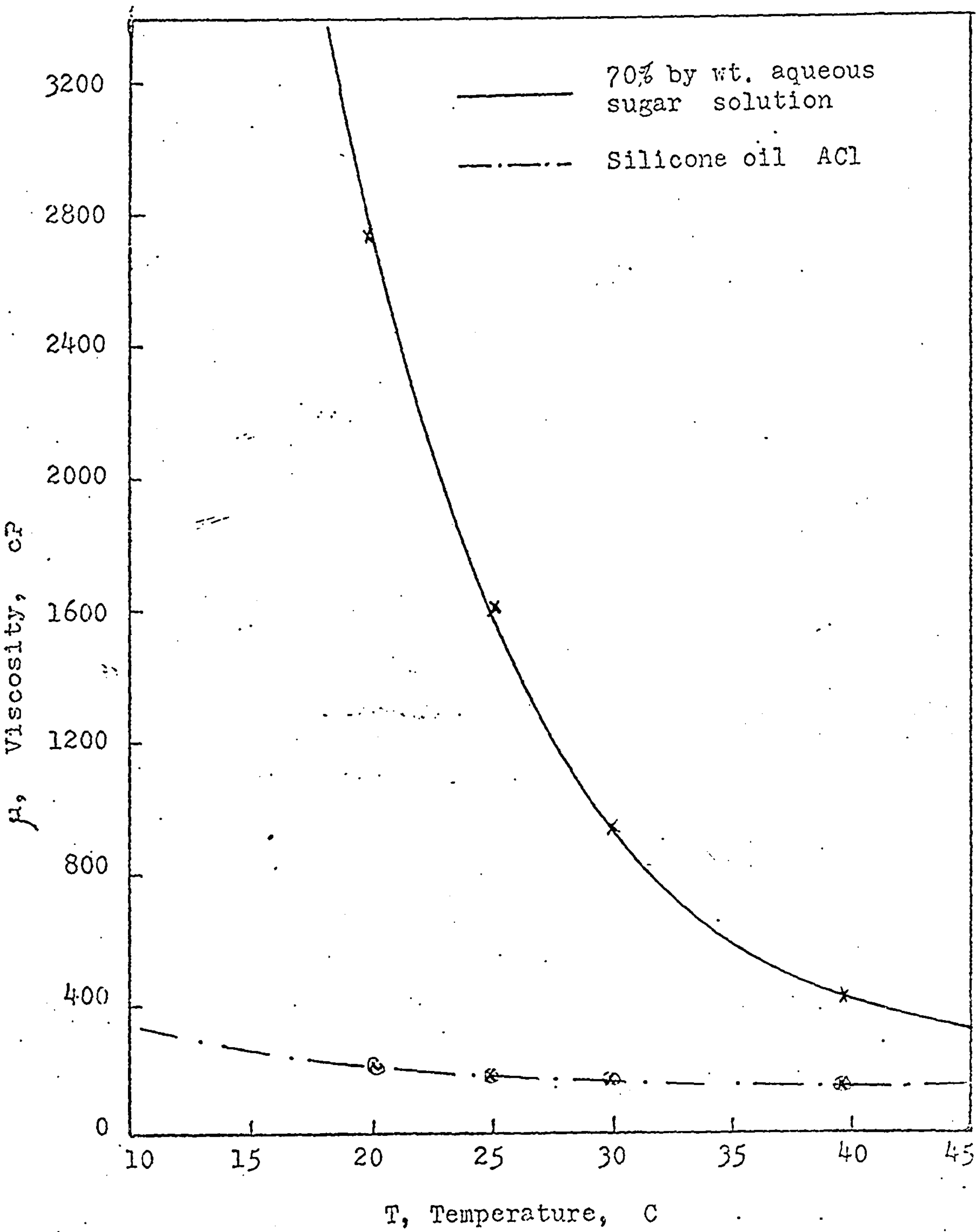

Fig. 3.4.1. Variation of viscosity with temperature.

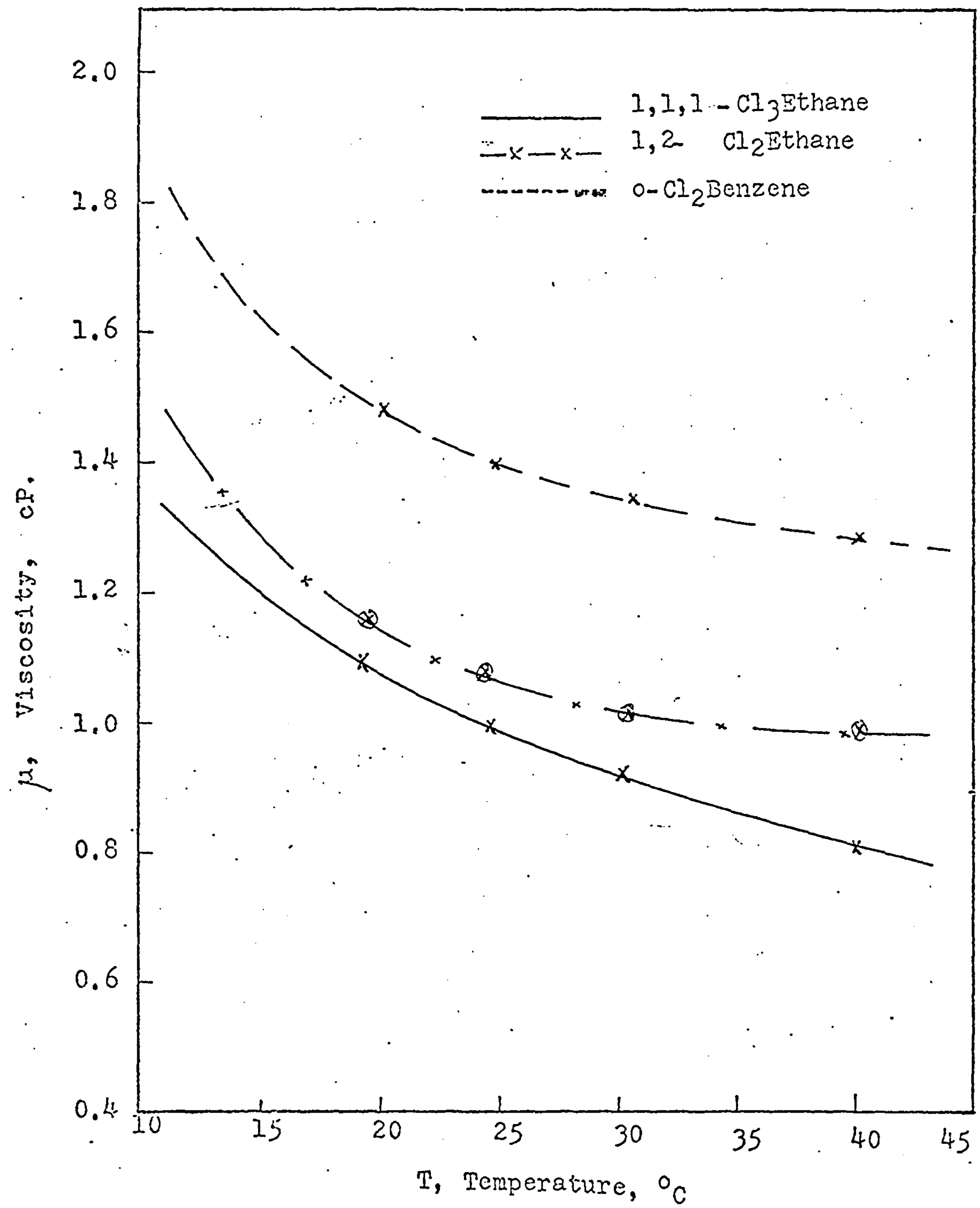

Fig. 3.4.2. Variation of viscosity with temperature.

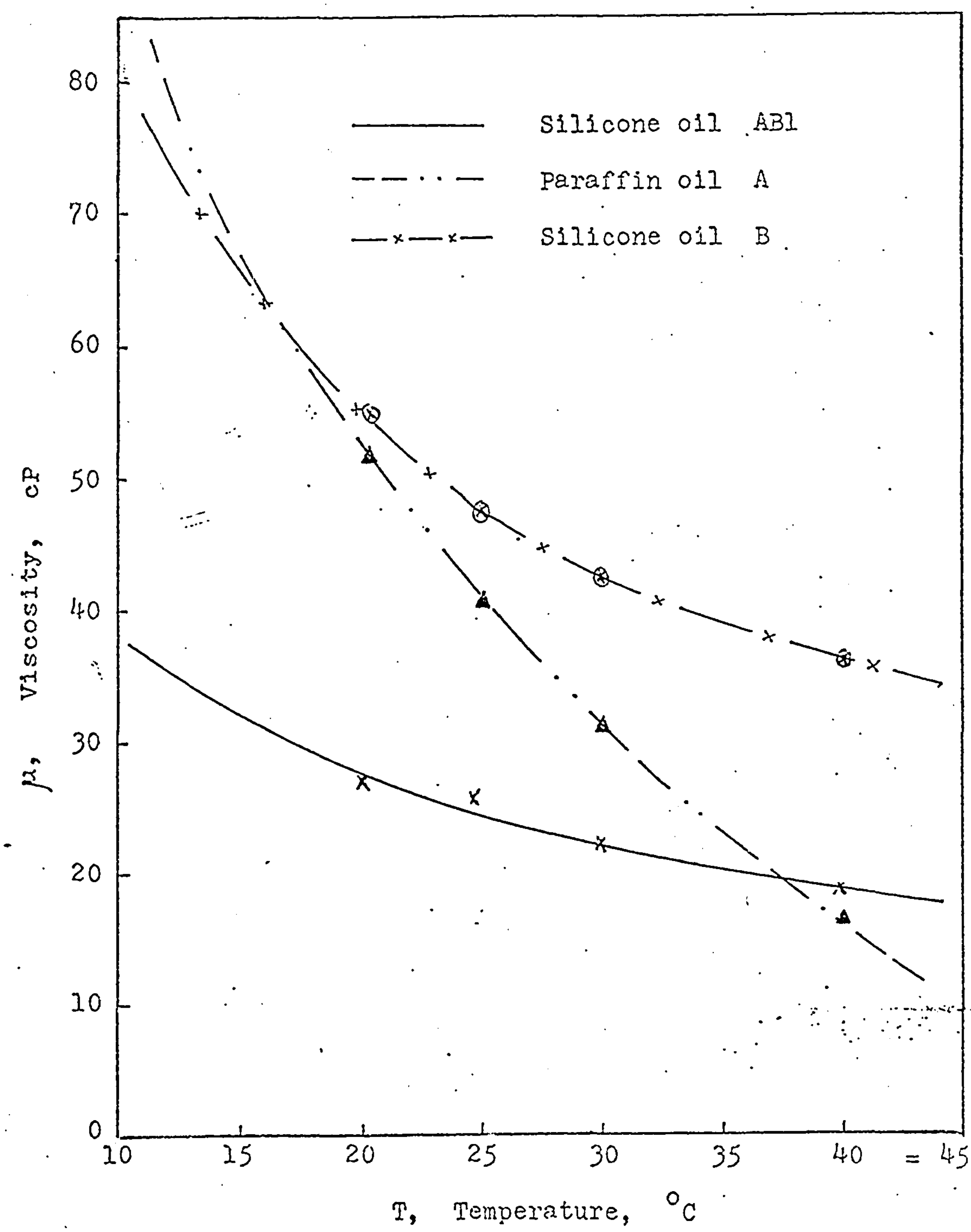

Fig. 3.4.3. Variation of viscosity with temperature.

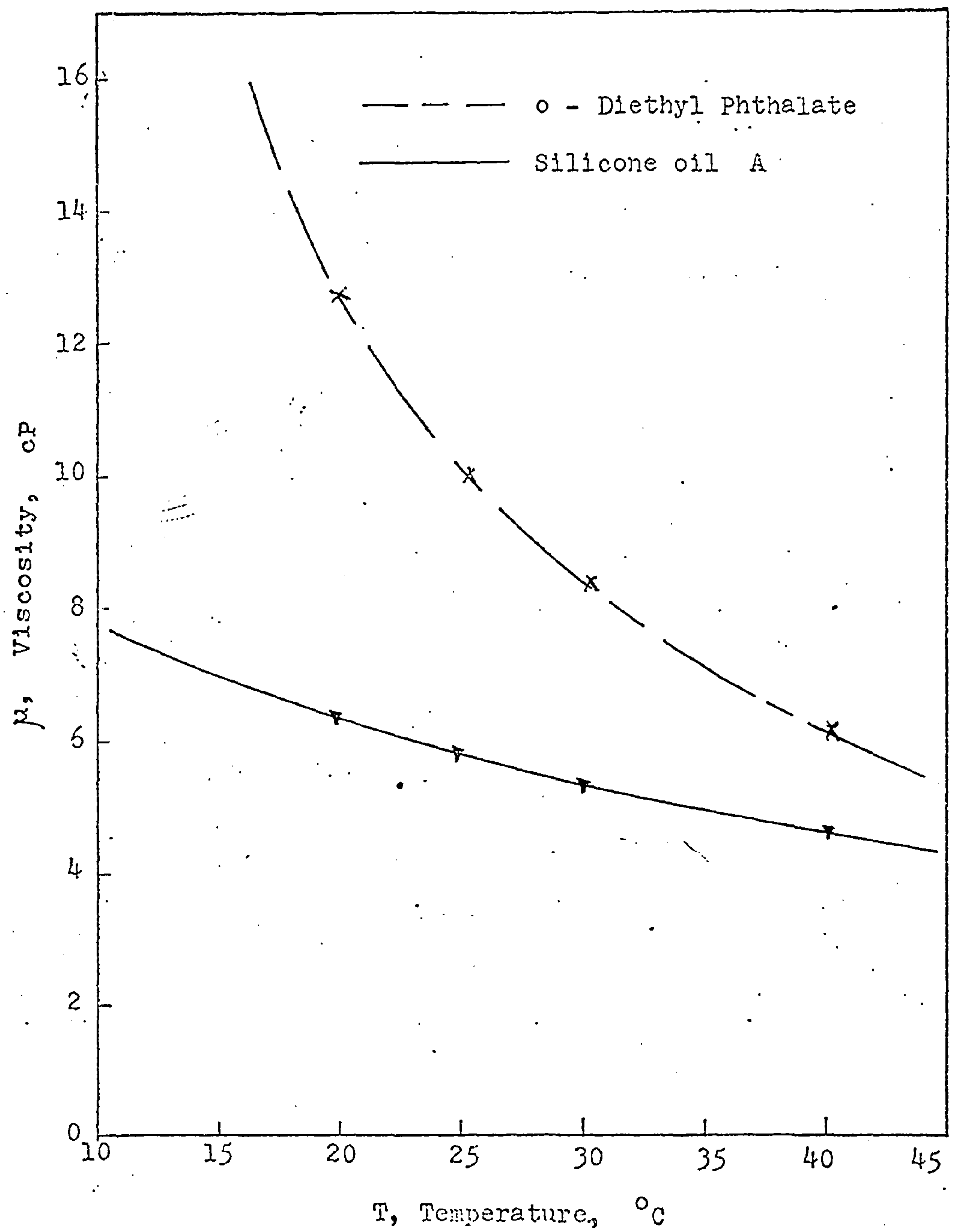

Fig. 3.4.4. Variation of viscosity with temperature.

TABLE A. Systems Studied and Physical Properties

System No.	Dispersed phase	Viscosity continuous phase μ (cp)	Viscosity dispersed phase μ' (cp)	Density continuous phase (g/c.c.)	Density dispersed phase (g/c.c.)	Inter-facial tension (dyne/cm)	Refractive index
1	Silicone oil A at 27.5°C	1160	5.45	1.385	0.92	53.49	1.403
2	Silicone oil B at 25.4°C	1460	46.5	1.385	0.958	53.90	1.404
3	Silicone oil AB1 at 27.8°C	1120	23.20	1.385	0.944	53.50	1.403
4	Silicone oil AC1 at 27.8°C	1120	190	1.385	0.936	50.63	1.405
5	Paraffin oil A at 26.5	1300	38.5	1.385	0.860	53.41	1.471
6	o-diethyl phthalate at 27.8°C	1120	8.9	1.385	1.115	29.40	---
7	o-dichlorobenzene at 27.8°C	1120	1.37	1.385	1.288	36.75	---
8	1,2-Dichloroethane at 27.5°C	1160	1.04	1.385	1.247	34.55	----
9	1,1,1- Trichloroethane at 27.5°C	1160	0.96	1.385	1.316	57.98	---

CHAPTER 4
SHAPES OF DIMPLED DROPS

4.0 Previous Hypotheses

It has been known for some time that large liquid drops do not possess symmetry about a horizontal plane. As already stated, Garner et al. (1957), Fararoui and Kintner (1961), and Shoemaker and Chazal (1969) revealed, instead, that a large liquid drop of low viscosity rising or falling through a high viscosity medium exhibits a marked cavity at its rear and smooth rounded curvature at its front. This lack of fore and aft symmetry has never been adequately explained, and only a few attempts to elucidate this matter have been undertaken.

4.1 Present Approach

In the present study an attempt has been made to gain a better understanding of the role of interfacial tension, hydrodynamic pressure, hydrostatic pressure, internal circulation and the wake region. Furthermore, the possible significance of the internal hydrostatic pressure gradients, boundary layer separation, and steady eddies in the wake region has been considered.

Surface forces at the liquid-liquid interface continually try to minimize the interfacial area. When interfacial tension forces are predominant, as for very small liquid drops, the drop assumes the shape of a sphere. Deformation begins to occur when other forces (e.g. inertial forces) are no longer negligible with respect to interfacial tension forces. In general, the problem of finding the shape of a free boundary is a very difficult one.

However, here it is felt that by using a semi-empirical approach, it might be possible to compute the pressure distribution with acceptable accuracy and hence deduct the shape.

4.1.1 Interfacial Tension

As a result of the net inward attraction exerted on the surface molecules by the molecules lying deeper within the drop, the interfacial tension of the dispersed liquid produces an increase of pressure within the drop over and above that prevailing in the field liquid adjacent to the interface. This increment in pressure, P_σ, at a given point on the drop is given by $P_\sigma = \sigma(1/R_1 + 1/R_2)$. This interfacial pressure increment can be positive or negative. Here we will adopt the convention that P_σ is positive for a case where the interface is convex as viewed from the field liquid and negative if the interface is concave. At the rear or frontal stagnation point, $R_1 = R_2 = R_0$ assuming axial symmetry, i.e. the drop surface can locally be considered a portion of a sphere of radius R_0 at these points. Hence, $P_\sigma = 2\sigma/R_0$. The technique for determining the two principle radii of curvature of a volute has been well established, Adam (1949). One of these radii, say $R_1(x)$, turns out to be simply the radius of curvature of a meridional profile at the height x, (Fig. 4.1). To measure this,

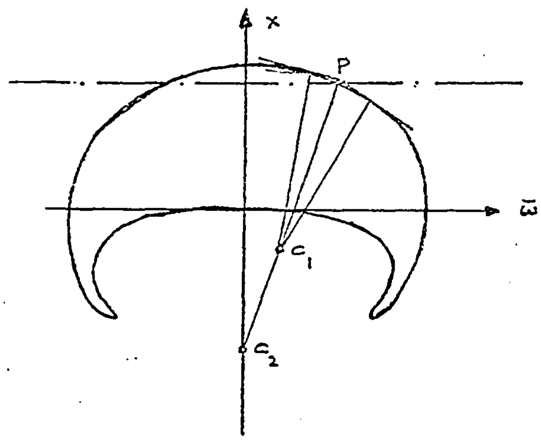

Fig.4.1. Definition sketch for determining the principal radii of curvature from any point P on the profile of the drop.

one constructs normals to the profile curve at each of a fairly dense series of points spaced regularly along the profile, and from there, the value of $R_1(x)$ can be determined by measuring the distance along the normal at P to the point of intersection with the normal drawn from the next adjoining point on the profile. In Fig. 4.1, $R_1(x)$ is shown as PC_1.

$R_2(x)$ is even more easily determined, since this second principal radius of curvature, for a surface of revolution, can be shown to be simply the distance from the profile at x to the axis of revolution measured along the local normal to the profile at x. In Fig. 4.1, $R_2(x)$ is shown as PC_2. The normals already constructed in the process of finding $R_1(x)$ facilitate rapid determination of $R_2(x)$.

4.1.2 Internal Hydrostatic Pressure

For a drop moving at its terminal velocity, there exists a vertical pressure gradient as for any mass of liquid in a gravitational field. This hydrostatic pressure gradient plays a major role in determining the shape of the drop.

4.1.3 Hydrodynamic Pressure Distribution

To evaluate the hydrodynamic pressure distribution on the exterior of a deformed liquid drop is an extremely difficult task. The hydrodynamic pressure distribution over a surface depends on the shape of the surface as well as on the Reynolds number and rigidity of the surface. Thus, it is impossible to calculate the pressure distribution unless we know the drop shape, which is, of course, what we wish to determine. One could only proceed here, in principle, by some method of successive approximations. For example, each hydrodynamic pressure calculation (based on the previous iterative approximation to the equilibrium shape) would be used to deduce a modified shape consistent with the surface tension, internal circulation and hydrostatic pressure requirements. Then this new shape would have to be used in the next iteration to recalculate the hydrodynamic pressure, and so on.

Unfortunately, there exists no general method for calculating analytically the pressure pattern about a surface of arbitrary shape. Superposition of a suitable array of sources and sinks, which is sometimes useful in treating potential flow around revolutes, is only sufficiently convergent to be practicable in the limit of very elongated bodies.

4.1.4 Internal Circulation

At an interface between two fluids, the condition of no slip implies that the surface layers of liquid on either side of the interface are moving with the same velocity. Since the outer fluid tends to be in motion at the interface of a drop, it thereby tries to induce axisymmetric circulation within the drop, Figure 4.2.

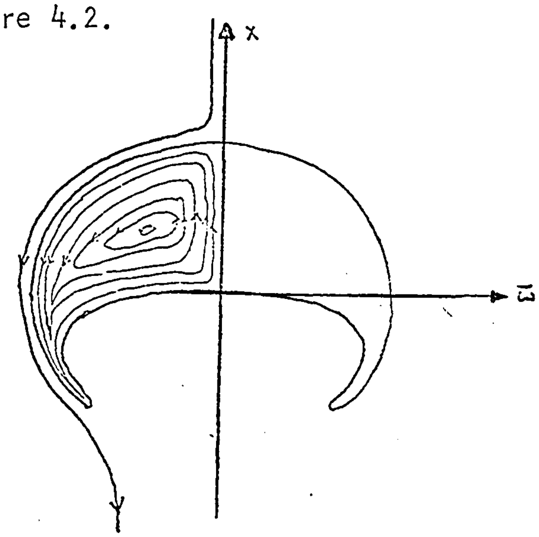

Fig.4.2. Internal Circulation

The existence of such internal motions has been observed for drops which are sufficiently large or uncontaminated by surface active molecules and, as we shall see, the internal motion contributes to the occurrence of dimpled shapes. In any analysis that will follow, it will be necessary to know whether the pressure at a point on the vertical axis of a drop is equal to that at the same height below the nose of the drop but lying just inside the drop surface. Consequently, it becomes necessary here to obtain some estimate of the intensity of internal circulation.

It is well known that the internal circulation does not depend simply on the external Reynolds numbers, but also on the viscosity ratio, K, Bond (1927), and on the degree of contamination of the interface. If K is very small, the effect of the internal viscosity can be neglected.

For the drops studied in this work the Reynolds number was typically of order 10. Thus the drops were such that inertial forces and viscous forces are of comparable magnitude and neither of the extremes cases (creeping flow where inertia forces are neglected nor inviscid flow) is expected to give good results. Nevertheless, these two cases can be regarded as limiting cases for certain purposes.

For the time being we may neglect the droplet deformation and any contamination of the interface. For the inviscid flow extreme, the flow pattern is then potential flow outside the spherical drop and Hill's spherical vortex inside. The maximum velocity is then $3/2\ U_0$ (at $r = R$ and $\theta = \pi/2$) relative to the drop. For the creeping flow case, the Hadamard-Rybczinski result holds with the result that the maximum circulation velocity (for $\kappa = \mu'/\mu \ll 1$) is $U_0/2$ (again at $r = R$ and $\theta = \pi/2$). To the extent that surface active impurities are present, this will cause a damping of the internal circulation; however, for the large drops considered here, this is not expected to be a significant factor. While droplet deformation no doubt causes distortion of the internal flow pattern, it seems unlikely that the actual range of internal velocity will change greatly from the corresponding spherical case. Thus, the internal velocity for the distorted drops studied here are expected to be of order U_0 relative to the drop. Thus the internal circulation is clearly important in establishing the internal pressure and hence the shape of the drop. This case may be contrasted with the case of a liquid drop falling through air where $\mu'/\mu \gg 1$ and internal circulation is negligible. In the latter case, Pruppacher (1972) has had some success in predicting droplet shapes by simply considering the hydrostatic pressure, surface tension pressure increment and the hydrodynamic pressure due to the external flow. It is clear that no such procedure is possible in our case.

4.2.0 Experimental Results, Shapes of Dimpled Drops

As noted in the previous section, the determination of drop shape, analytically or even empirically, is virtually impossible. This is due to several reasons:

i We are dealing with a range of Reynolds numbers where neither creeping flow nor potential flow models can be applied correctly.

ii In liquid drops the effect of viscosity and density for the internal liquid cannot, in general, be ignored. Compare the case of gas bubbles where both may be ignored, in general.

iii A complete understanding of the internal vortical circulation is necessary to be able to predict shapes for deformed drops.

iv An expression to predict the hydrodynamic pressure distribution at every point along the interface must be available. Since the shape changes as the size of the drop varies, general relationships are required.

v The nature of the wake, the dimple at the rear surface and the effects of the skirts formed at the edge of the concave region must be clearly understood.

Despite all these problems, an attempt was made to derive an equation for pressure distribution by solving the equations of motion in creeping flow. Needless to say, this did not prove fruitful. Firstly, we know that creeping flow equations are only valid for $Re < O(1)$. Secondly, we know that for cases where inertial terms can be neglected, there is no tendency for deformation to occur, no matter how small the surface tension, Batchelor (1967). Typical drop shapes observed in our experiments are shown in Fig. 4.3.

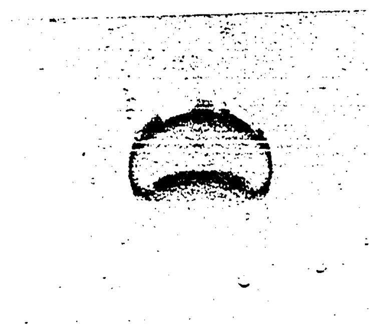

Silicone oil d=3.07 cm U_o=13.0 cm/sec

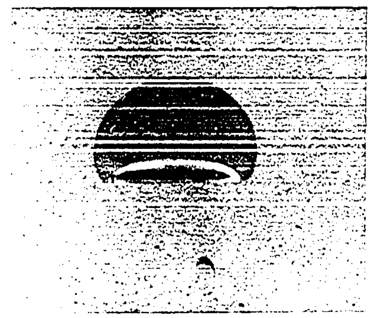

o-Cl_2benzene d=5.09 cm U_o=10.0 cm/sec

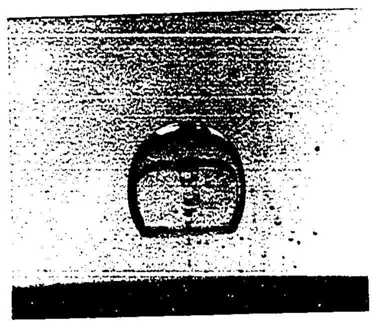

Silicone oil d=4.32 cm U_o=19.0 cm/sec

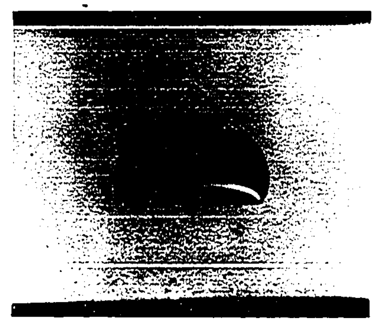

o-Cl_2benzene d=5.72 cm U_o=10.4 cm/sec

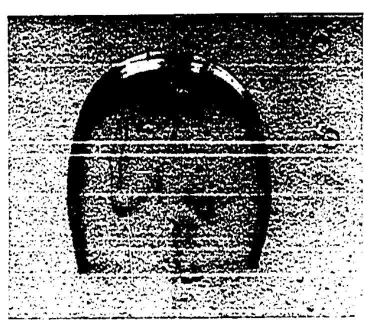

Silicone oil d=4.83 cm U_o=20.0 cm/sec

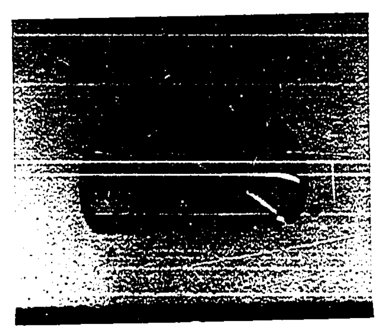

o-Cl_2benzene d=6.81 cm U_o=11.0 cm/sec

Fig.4.3. Typical Shapes of Large Dimpled Drops.

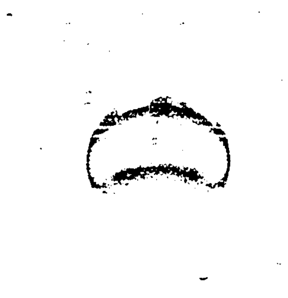

Silicone oil d=3.07 cm
U_o=13.0 cm/sec

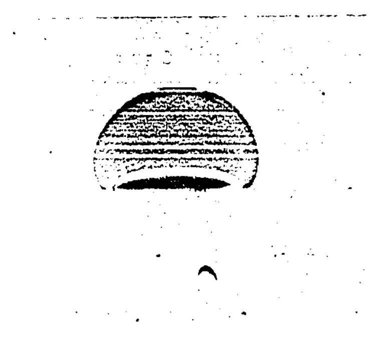

o-Cl_2benzene d=5.09 cm
U_o=10.0 cm/sec

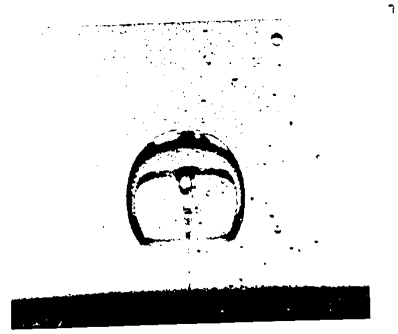

Silicone oil d=4.32 cm
U_o=19.0 cm/sec

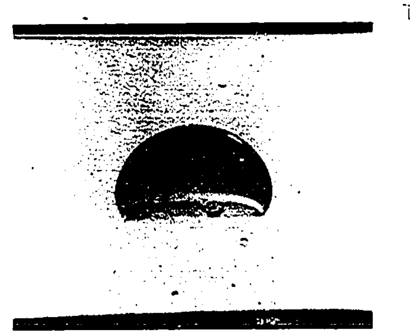

o-Cl_2benzene d=5.72 cm
U_o=10.4 cm/sec

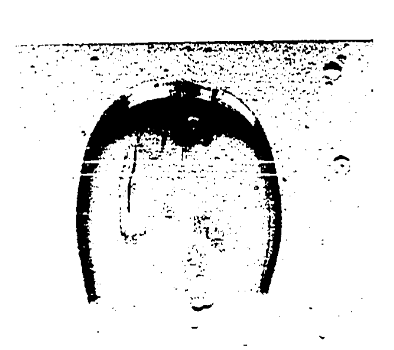

Silicone oil d=4.83 cm
U_o=20.0 cm/sec

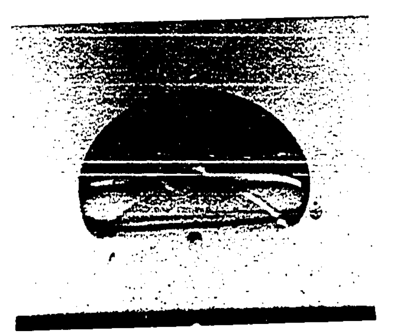

o-Cl_2benzene d=6.81 cm
U_o=11.0 cm/sec

Fig.4.3. Typical Shapes of Large Dimpled Drops.

In view of the formidable analytical problems discussed above and the extent of the deformations (which make perturbation analyses useless), it is not feasible to arrive at quantitative predictions of drop shape. The best that can be hoped for is a consistent qualitative explanation for the phenomena observed.

It is clear from the above that the drop shape, flow patterns, drag coefficient, etc. are all interrelated. A plot of drag coefficient, C_D,* against Reynolds number, Re**, is shown in Fig. 4.4. The corresponding shapes are included on each line. From the graph, we can see that C_D first decreases with increasing Re. This corresponds to the region where the shape of the drop changes little. At some critical value, depending on the physical properties of the system, C_D reaches a minimum and then begins to increase. This minimum point corresponds to the region where the skirts straighten downwards and waves are observed to travel down the skirts relative to the drops. Taylor (1960) has distinguished two types of wave motion ("symmetric" and "antisymmetric") for waves travelling along thin sheets of one fluid in another. The waves observed in the liquid skirts in our investigation appeared to be of the symmetric type. The fact that the wave

---

* $C_D = \dfrac{\Delta \rho g V}{\frac{1}{2}\rho U_0^2 . \pi a^2}$ where V is the volume of the drop

** $Re = \dfrac{d U_0}{\nu}$

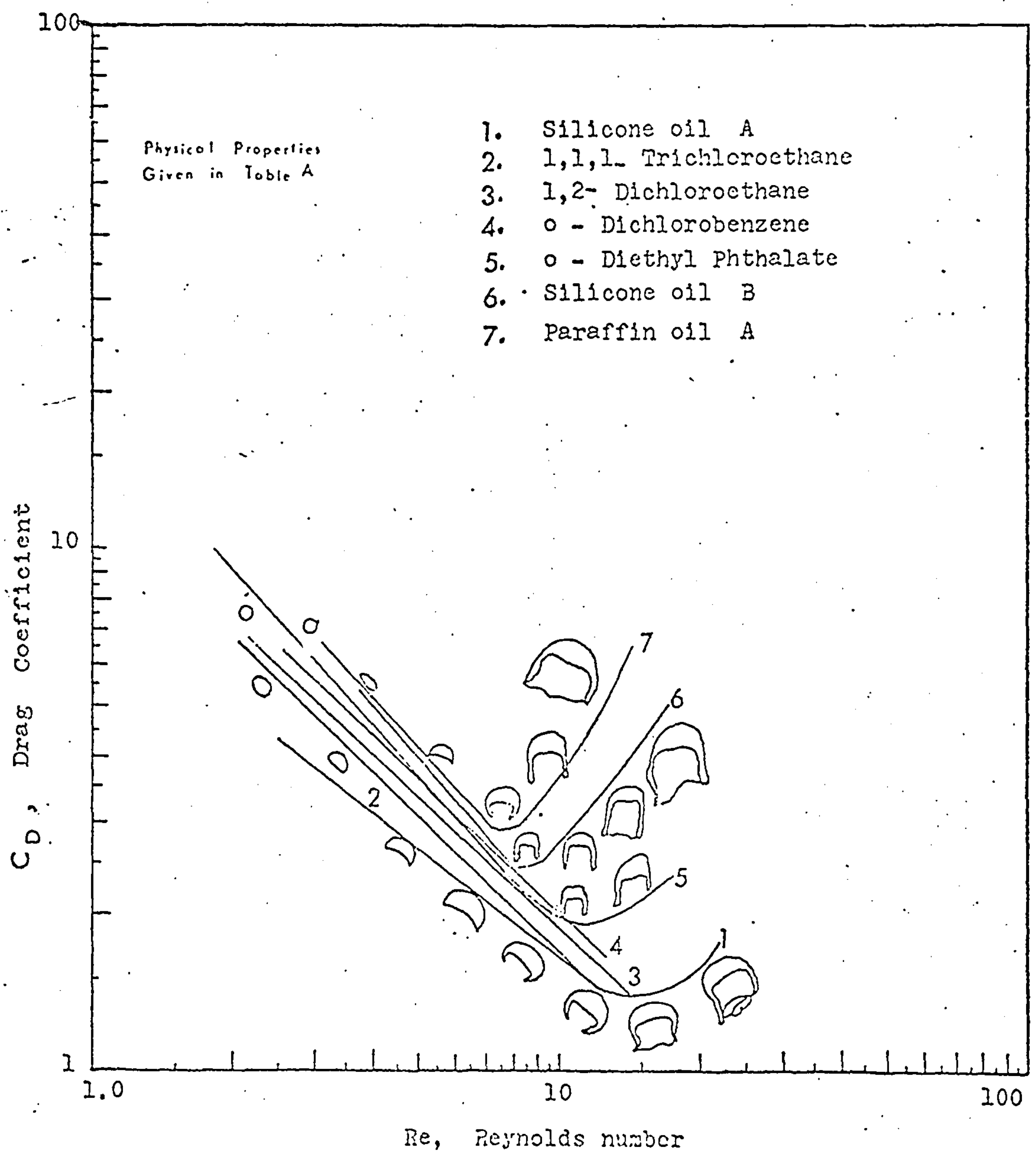

Fig. 4.4., Variation of drag coefficient with Reynolds number.

motion was symmetric, however, does not imply that the skirts themselves were always axisymmetric. For very large drops (e.g. for $d = 4$ cm for silicone oil A), the skirts were unbalanced as shown in Figure 4.5.

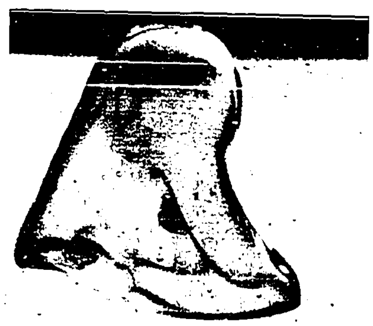

Fig.4.5. Large drop in silicone oil A (unbalanced skirt)
$d = 6.39$ cm, $U_o = 20.0$ cm/sec

The skirt then widens out and becomes asymmetric and unstable, growing in length as the drop rises. This corresponds to the region where C_D increases with increasing Re.

This increase in drag coefficient is probably due to the increase in the length and "roughness" of the skirt which is bound to increase the form and frictional drag and lead to induced drag.

The variation of Eötvos number, Eö*, with Reynolds number, Re, is plotted in Figure 4.6. As we can see from the graph, the points for o-diethyl phthalate, paraffin oil A, and silicone oil B fall on the same line. Immediately below them are those for silicone oil A and 1, 2- dichloroethane, on another common line. Separate curves for o-dichlorobenzene and 1, 1, 1 - trichloroethane fall at lower Eötvos number. Efforts were made to correlate these results using the physical property groups, M_1** and M_2***, (Morton numbers, commonly used in bubble studies) and P**** (commonly used in correlating data for small drops). These efforts were unsuccessful. The full data on the shapes of drops and their velocities are given in Tables B1 - B8 at the end of this chapter.

---

* $E_0 = \frac{\Delta\rho g d^2}{\sigma}$

** $M_1 = g\mu^4/\rho\sigma^3$

*** $M_2 = g\mu^4/\ \sigma^3$

**** $P = \frac{\rho^2\sigma^3}{\Delta\rho g\mu^4}$

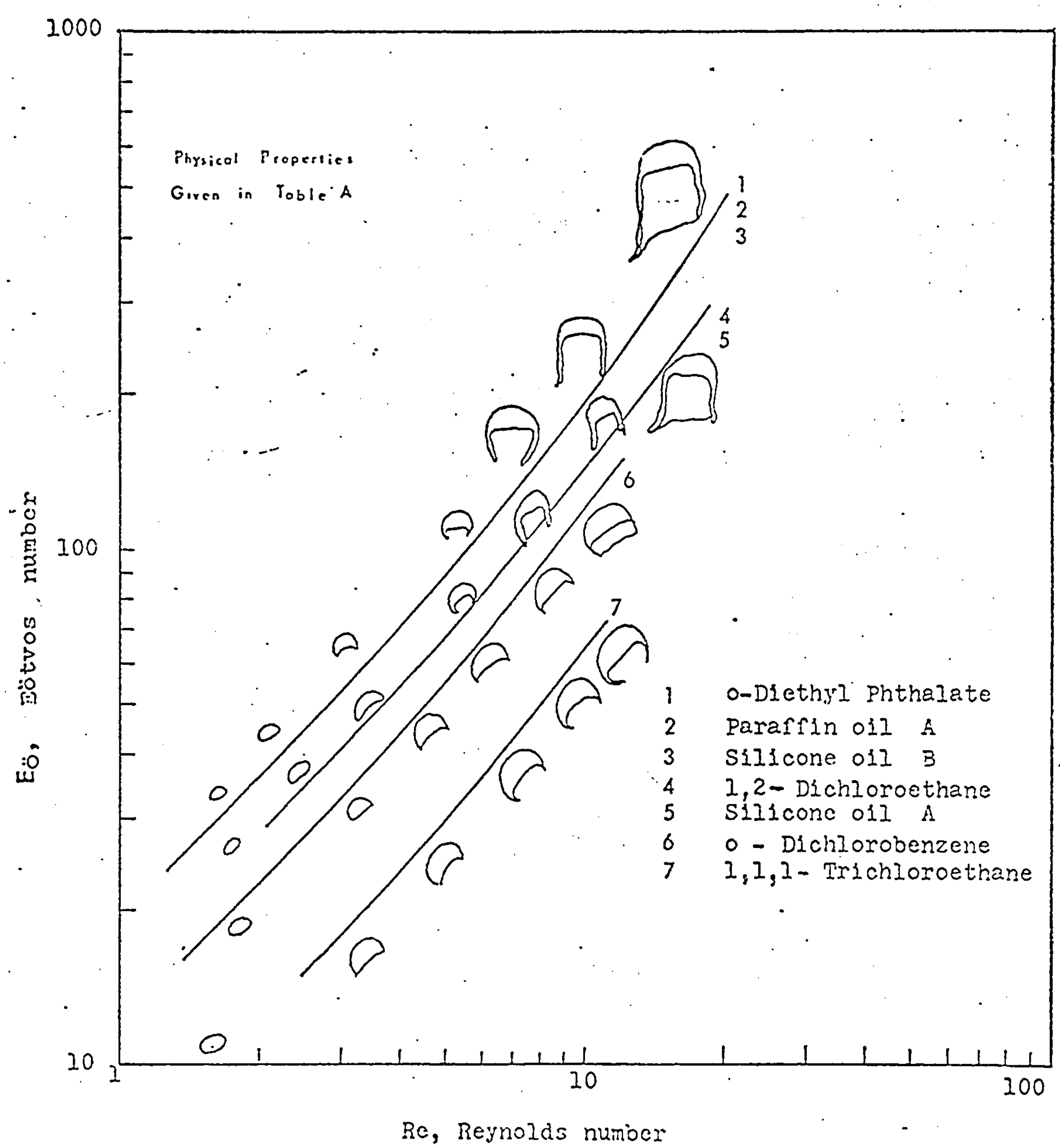

Fig. 4.6. Variation of Eötvos number with Reynolds number.

TABLE B1. Full Data on the Shapes of Drops and Their Velocities

Silicone Oil A - 27.5°C

un	Equivalent Diameter d, cm	Semi-major axis a, cm	Semi-minor axis b, cm	Eccentricity e=c/a	Aspect Ratio b/a	Terminal Velocity U_0, cm/sec	Reynolds Number Re	Eötvos Number Eo	Skirt Number Sk	Jeffrey's Number Je	Drag Coeff. C_D	Skirt Length z, cm	Angle Max
1	2.35	1.66	1.11	0.74	0.67	13.86	3.89	47.05	3.03	15.65	2.68	0.0	45.0
2	3.08	2.16	1.25	0.82	0.58	17.32	6.37	80.82	3.07	21.52	2.28	0.0	50.0
3	4.32	3.42	1.78	0.85	0.52	22.00	11.35	158.99	4.76	33.33	1.57	4.90	55.0
4	4.38	3.57	1.91	0.84	0.54	22.34	11.68	163.44	4.76	33.74	1.45	5.30	56.0
5	4.74	3.78	2.03	0.84	0.54	23.18	13.12	191.41	5.00	38.08	1.53	7.10	56.0
6	4.79	3.94	2.12	0.84	0.54	24.09	13.78	195.47	5.26	37.42	1.34	7.10	56.0
7	5.02	4.06	1.54	0.93	0.38	24.69	14.80	214.69	5.26	40.10	1.38	8.50	56.0
8	5.66	4.62	2.52	0.84	0.55	26.29	17.77	272.92	5.56	47.87	1.35	8.00	59.0
9	5.95	4.68	2.46	0.85	0.53	26.29	18.68	301.61	5.56	52.90	1.52	9.30	56.0
10	6.50	4.98	2.34	0.88	0.47	26.78	20.78	359.94	5.88	61.98	1.70	11.00	60.0

TABLE B2. Full Data on the Shapes of Drops and Their Velocities

Silicone Oil ABl - 27.8°C

n	Equivalent Diameter d, cm	Semi-major axis a, cm	Semi-minor axis b, cm	Eccentricity e=c/a	Aspect Ratio b/a	Terminal Velocity U_0, cm/sec	Reynolds Number Re	Eötvos Number Eo	Skirt Number Sk	Jeffrey's Number Je	Drag Coeff. C_D	Skirt Length z, cm	Angle Max
1	3.08	1.85	1.35	0.68	0.73	13.99	5.43	76.63	2.86	26.64	4.52	0.00	55.0
2	4.10	3.20	1.72	0.84	0.54	20.45	10.56	135.79	4.17	32.30	1.57	4.40	——
3	4.32	3.13	1.97	0.78	0.63	18.48	10.05	150.76	3.85	39.68	2.51	3.20	40.0
4	4.38	2.95	1.72	0.81	0.58	18.73	10.33	154.97	3.85	40.24	2.87	3.40	52.0
5	4.84	3.13	1.48	0.88	0.47	19.75	12.04	189.24	4.00	46.60	3.08	5.50	55.0
6	5.10	3.39	1.78	0.85	0.53	20.87	13.40	210.11	4.35	48.97	2.76	0.00	——
7	5.34	3.20	1.66	0.85	0.52	20.45	13.75	230.35	4.17	54.79	0.55	7.00	52.0
8	6.10	3.08	1.54	0.87	0.50	20.14	15.47	300.59	4.17	72.59	6.12	6.80	52.0
9	6.21	3.57	1.97	0.83	0.55	21.66	16.94	311.53	4.35	67.95	4.16	0.00	55.0

TABLE B3. Full Data on the Shapes of Drops and Their Velocities

Paraffin Oil A - 26.5°C

Run	Equivalent Diameter d, cm	Semi-major axis a, cm	Semi-minor axis b, cm	Eccentricity e=c/a	Aspect Ratio b/a	Terminal Velocity U_0, cm/sec	Reynolds Number Re	Eötvos Number Eo	Skirt Number Sk	Jeffrey's Number Je	Drag Coeff. C_D	Skirt Length z, cm	Angle Max
1	2.53	1.40	1.22	0.49	0.87	13.12	3.54	61.66	3.23	19.31	5.94	0.00	40
2	3.08	1.92	1.41	0.68	0.73	16.48	5.41	91.38	4.00	22.78	3.60	0.18	45
3	3.78	2.52	1.43	0.82	0.57	19.26	7.65	134.02	4.76	28.59	2.72	1.90	50
4	3.88	2.62	1.64	0.78	0.63	19.49	8.06	145.02	4.76	30.57	2.71	2.20	50
5	4.49	2.77	1.57	0.82	0.57	21.03	10.06	194.20	5.00	37.94	3.31	3.90	54
6	4.60	2.86	1.29	0.89	0.45	21.35	10.46	203.84	5.26	39.23	3.22	4.80	55
7	5.06	2.68	1.33	0.87	0.50	21.80	11.75	246.64	5.26	46.48	4.69	5.30	50
8	5.14	2.65	1.23	0.89	0.46	21.80	11.94	254.50	5.26	47.96	5.04	8.80	55
9	5.18	2.80	1.41	0.86	0.50	21.80	12.03	258.48	5.26	48.71	4.62	3.00	55
10	5.22	2.83	1.41	0.87	0.50	21.80	12.12	262.48	5.26	49.47	4.63	6.60	55
11	5.66	2.68	1.35	0.86	0.50	21.80	13.15	308.60	5.26	58.16	6.57	9.80	55
12	6.21	3.26	1.75	0.84	0.54	23.02	15.23	371.49	5.56	66.30	5.26		55
13	6.12	3.08	1.35	0.90	0.44	22.16	14.45	360.79	5.26	66.89	6.11	4.30	55

TABLE B4. Full Data on the Shapes of Drops and Their Velocities

o-Diethyl Phthalate - 27.8°C

Run	Equivalent Diameter d, cm	Semi-major axis a, cm	Semi-minor axis b, cm	Eccentricity e=c/a	Aspect Ratio b/a	Terminal Velocity U0, cm/sec	Reynolds Number Re	Eötvos Number Eo	Skirt Number Sk	Jeffrey's Number Je	Drag Coeff. C_D	Skirt Length z, cm	Angle Max
1	1.86	1.16	1.03	0.46	0.89	7.43	1.71	13.14	2.86	11.00	5.55	0.00	—
2	2.13	1.33	1.28	0.26	0.96	8.54	2.25	40.83	3.23	12.55	4.79	0.00	—
3	2.35	1.35	1.06	0.62	0.79	9.65	2.80	49.70	3.70	13.52	4.86	0.00	—
4	2.96	1.63	1.37	0.54	0.84	10.37	3.80	78.85	4.00	19.96	5.77	0.00	—
5	3.39	2.05	1.69	0.57	0.82	13.49	5.66	103.43	5.00	20.13	3.23	0.50	44
6	4.08	2.95	2.02	0.73	0.68	16.30	8.22	149.82	6.25	24.13	1.87	2.10	52
7	4.27	3.04	1.92	0.78	0.63	16.09	8.50	164.10	6.25	26.77	2.07	2.70	50
8	4.32	3.34	1.88	0.83	0.56	17.43	9.31	167.96	6.67	25.30	1.52	3.80	52
9	4.38	3.06	1.88	0.79	0.61	16.30	8.83	172.66	6.25	27.81	2.15	2.90	50
10	4.54	3.41	1.92	0.83	0.56	16.96	9.52	185.51	6.25	28.71	1.79	4.10	52
11	4.88	3.73	1.92	0.86	0.51	18.73	11.30	214.33	7.14	30.04	1.52	7.40	55
12	5.34	3.66	2.05	0.83	0.56	19.02	12.56	256.64	7.14	35.42	2.00	7.20	55
13	6.01	3.94	2.36	0.80	0.60	20.24	15.04	325.08	7.69	42.16	2.17	7.70	53
14	6.73	4.35	2.48	0.82	0.57	20.92	17.41	407.64	7.69	51.15	2.34	5.60	—
15	6.79	4.62	2.57	0.83	0.56	22.02	18.49	414.94	8.33	49.47	1.93	9.20	55

TABLE B5. Full Data on the Shapes of Drops and Their Velocities

Silicone Oil ACI - 27.8°C

Run	Equivalent Diameter d, cm	Semi-major axis a, cm	Semi-minor axis b, cm	Eccentricity e=c/a	Aspect Ratio b/a	Terminal Velocity U_0, cm/sec	Reynolds Number Re	Eötvos Number Eo	Skirt Number Sk	Jeffrey's Number Je	Drag Coeff. C_D	Skirt Length z, cm	Angle Max
1	1.86	1.02	0.92	0.43	0.90	7.85	1.81	30.07	1.72	17.32	10.69	——	——
2	3.08	1.96	1.30	0.75	0.66	13.16	5.01	82.45	2.94	28.32	4.62	——	——
3	3.19	2.09	1.29	0.79	0.62	13.65	5.38	88.44	3.03	29.29	4.21	——	——
4	4.10	3.11	1.29	0.91	0.41	15.37	7.79	146.09	3.45	42.97	3.00	——	——
5	4.60	3.39	1.29	0.92	0.38	15.80	8.99	183.90	3.45	52.62	3.58	——	——
6	4.30	2.71	1.35	0.87	0.50	16.05	10.52	244.13	3.57	68.76	8.33	——	——
7	5.69	3.08	1.41	0.89	0.46	16.05	11.29	281.38	3.57	79.25	7.99	——	——

TABLE B6. Full Data on the Shapes of Drops and Their Velocities

Silicone Oil B - 25.4°C

Run	Equivalent Diameter d, cm	Semi-major axis a, cm	Semi-minor axis b, cm	Eccentricity e=c/a	Aspect Ratio b/a	Terminal Velocity U_0, cm/sec	Reynolds Number Re	Eötvos Number Eo	Skirt Number Sk	Jeffrey's Number Je	Drag Coeff. C_D	Skirt Length z, cm	Angle Max
1	1.86	1.08	—	—	—	—	1.63	28.86	2.50	10.75	6.57	—	50
2	2.13	1.05	0.92	0.48	0.88	9.30	1.88	35.22	2.50	13.98	10.25	0.00	48
3	2.53	1.36	1.23	0.43	0.90	11.62	2.79	49.69	3.13	15.79	6.52	0.00	—
4	2.96	1.85	1.50	0.59	0.81	14.57	4.09	68.02	4.00	17.24	3.59	0.10	40
5	3.13	1.85	1.32	0.70	0.71	14.91	4.43	76.06	4.00	18.83	4.07	0.00	40
6	3.29	1.85	1.48	0.60	0.80	14.91	4.65	84.03	4.00	20.81	4.71	0.00	42
7	3.80	2.52	1.85	0.68	0.73	18.03	6.50	84.03	4.76	21.95	2.68	0.40	40
8	4.01	2.65	1.99	0.66	0.75	18.89	7.18	124.84	5.00	24.42	2.61	1.00	42
9	4.27	2.95	1.85	0.78	0.63	19.79	8.02	141.55	5.26	26.41	2.30	1.80	54
10	4.44	2.83	1.81	0.77	0.64	19.79	8.33	153.50	5.26	25.51	2.80	0.00	50
11	4.88	3.20	1.89	0.81	0.58	21.10	9.77	184.89	5.56	32.35	2.57	0.40	50
12	5.41	3.17	1.60	0.86	0.50	21.92	11.25	227.23	8.88	38.27	3.31	8.30	52
13	5.73	3.32	1.78	0.84	0.54	22.81	12.40	254.90	6.25	41.27	3.30	7.10	50
14	6.18	3.59	1.72	0.88	0.48	23.66	13.87	396.51	6.25	46.27	3.33	10.20	55
15	6.75	3.14	1.59	0.86	0.51	24.17	15.48	353.73	6.67	54.03	2.61	6.70	50

TABLE B7. Full Data on the Shapes of Drops and Their Velocities

o-Dichlorobenzene - 27.8^{o}C

Run	Equivalent Diameter d, cm	Semi-major axis a, cm	Semi-minor axis b, cm	Eccentricity e=c/a	Aspect Ratio b/a	Terminal Velocity U_0, cm/sec	Reynolds Number Re	Eötvos Number Eo	Skirt Number Sk	Jeffrey's Number Je	Drag Coeff. C_D	Skirt Length z, cm	Angle Max
1	———	———	———	———	———	———	1.54	17.62	0.08	0.69	27.27	———	———
2	3.72	2.18	1.88	0.51	0.86	7.21	3.33	35.99	2.17	16.38	4.79	0.00	40
3	4.21	2.57	1.90	0.67	0.74	7.95	4.14	45.85	2.44	18.92	4.08	0.00	40
4	4.38	2.61	2.34	0.44	0.90	8.31	4.50	49.62	2.50	19.59	4.09	0.00	38
5	———	———	———	———	———	———	6.05	68.34	2.86	23.58	3.38	———	43
6	5.25	3.29	2.57	0.62	0.78	10.46	6.79	71.30	3.23	22.37	2.81	0.00	40
7	5.56	3.68	2.91	0.61	0.79	10.29	7.08	79.96	3.13	25.50	2.74	0.00	45
8	2.59	3.59	2.65	0.67	0.74	10.20	7.05	80.83	3.13	26.00	2.98	0.00	43
9	6.17	4.28	3.04	0.70	0.71	11.11	8.48	98.47	3.03	29.08	2.37	0.10	45
10	6.31	4.19	3.04	0.69	0.73	11.21	8.75	102.99	3.45	30.15	2.60	0.00	45
11	6.33	4.49	3.59	0.60	0.80	11.21	8.78	103.65	3.45	30.34	2.29	0.30	44
12	6.74	4.92	2.82	0.82	0.57	11.73	9.98	117.51	3.57	32.87	2.10	0.00	52
13	6.90	5.18	3.08	0.80	0.59	12.30	10.50	123.15	3.70	32.85	1.85	2.50	52
14	6.93	5.13	3.39	0.75	0.66	11.95	10.24	124.22	3.57	34.11	2.03	0.70	52
15	7.11	5.65	3.76	0.75	0.67	12.55	11.03	130.76	3.85	34.19	1.63	2.40	50

TABLE B8. Full Data on the Shapes of Drops and Their Velocities

1,2 - Dichloroethane - 27.5°C

Run	Equivalent Diameter d, cm	Semi-major axis a, cm	Semi-minor axis b, cm	Eccentricity e=c/a	Aspect Ratio b/a	Terminal Velocity U_0, cm/sec	Reynolds Number Re	Eötvos Number Eo	Skirt Number Sk	Jeffrey's Number Je	Drag Coeff. C_D	Skirt Length z, cm	Angle Max
1	1.69	0.94	0.86	0.40	0.91	3.39	0.68	11.18	1.14	9.82	15.55	0.00	—
2	2.13	1.41	1.20	0.53	0.85	6.00	1.45	17.76	2.00	8.82	4.41	0.00	40
3	3.08	1.67	1.37	0.57	0.82	7.02	2.58	37.13	2.38	15.76	6.90	0.00	40
4	3.19	1.80	1.37	0.65	0.76	8.31	3.17	39.83	2.78	14.28	4.71	0.00	38
5	3.48	2.10	1.71	0.58	0.81	8.60	3.57	47.40	2.86	16.42	4.20	0.00	40
6	4.01	2.44	1.88	0.64	0.77	9.80	4.69	62.94	3.03	19.13	3.68	0.00	40
7	4.14	2.57	2.05	0.60	0.80	10.37	5.13	67.09	3.45	19.27	3.26	0.00	42
8	4.44	2.82	2.22	0.62	0.79	10.63	5.64	77.17	3.57	21.62	3.16	0.00	40
9	4.79	3.08	2.26	0.68	0.73	11.51	6.46	86.47	3.85	22.38	2.68	0.00	41
10	5.59	4.02	2.85	0.71	0.71	12.94	8.64	122.32	4.35	28.15	2.10	1.50	50
11	5.89	4.15	2.43	0.81	0.59	13.21	9.29	135.80	4.35	30.62	2.21	1.70	40
12	6.40	4.88	2.82	0.82	0.58	14.77	11.29	160.33	5.00	32.33	1.64	4.30	54
13	6.63	5.35	3.93	0.68	0.73	14.94	11.83	172.06	5.00	34.30	1.48	3.40	50
14	7.15	5.73	3.06	0.85	0.53	15.69	13.39	200.11	5.26	37.99	1.47	6.00	55

TABLE B9. Full Data on the Shapes of Drops and Their Velocities

1,1,1-Trichloroethane - 27.5°C

Run	Equivalent Diameter d, cm	Semi-major axis a, cm	Semi-minor axis b, cm	Eccentricity e=c/a	Aspect Ratio b/a	Terminal Velocity U_0, cm/sec	Reynolds Number Re	Eötvos Number Eo	Skirt Number Sk	Jeffrey's Number Je	Drag Coeff. C_D	Skirt Length z, cm	Angle Max
1	2.44	1.20	1.03	0.51	0.86	3.59	1.05	6.94	0.72	9.67	12.77	0.00	—
2	2.96	1.44	1.20	0.55	0.83	4.10	1.45	10.22	0.82	12.46	12.08	0.00	36
3	—	—	—	—	—	—	3.03	16.84	1.33	12.62	4.05	—	36
4	4.44	2.65	2.14	0.59	0.81	4.70	2.49	22.99	0.94	24.45	9.16	0.00	38
5	4.79	2.83	2.48	0.48	0.88	7.79	4.46	26.76	1.56	17.17	3.68	0.00	45
6	5.18	3.15	2.57	0.58	0.82	8.77	5.52	31.29	1.75	17.84	2.97	0.00	42
7	6.04	3.94	2.91	0.67	0.74	9.88	7.13	42.55	1.96	21.53	2.36	0.50	45
8	6.12	4.17	2.14	0.75	0.66	9.80	7.16	43.68	1.96	22.28	2.24	0.00	50
9	6.21	4.19	2.70	0.76	0.64	10.04	7.44	44.98	2.00	22.39	2.20	2.10	50
10	6.37	4.45	3.04	0.73	0.68	10.37	7.89	47.32	2.08	22.81	1.98	2.20	50
11	6.55	4.62	2.87	0.78	0.62	10.37	8.11	50.04	2.08	24.12	2.00	2.20	50
12	6.65	4.72	3.10	0.75	0.66	10.73	8.52	51.58	2.13	24.03	1.87	1.70	50
13	7.09	5.13	3.39	0.75	0.66	11.10	9.40	58.63	2.22	26.40	1.79	2.40	52

CHAPTER 5

INVESTIGATION OF TERMINAL VELOCITY AND EXPERIMENTAL RESULTS

5.0 Basic Problems

The investigation of the motion of a dimpled drop in a liquid presents theoretical problems of such remarkable complexity, that rigorous solutions for the equations of motion are almost impossible. Some of these complexities include;

i As we have seen in the previous chapter, the shape of the drop can not be predicted reliably. Experiments have shown that small drops in viscous liquids are almost spherical in shape with a dimple at the rear while larger sized drops have an oblate-capped shape. At larger sizes still, the shapes take complex forms as shown on page 89.

ii Internal circulation occurs.

iii The nature of the flow patterns are difficult to establish.

iv The complete interfacial conditions are not easily characterized.

v The nature of the wake, the concavity at the rear surface, and the effect of the skirts formed at the edge of the concave region, are not easily characterized.

With the hope of establishing the form of an expression suitable for the calculation of drop terminal velocities, the following four limiting cases have been examined;

i Ellipsoidal coordinate approach with specific assumptions including creeping flow in the continuous phase.

ii Spherical coordinate approach with specific assumptions as in (i).

iii Semi-empirical method by combining the results obtained in (ii) with the knowledge of flow past a spherical body in the Reynolds number range of interest.

iv Oblate spheroid method assuming potential flow.

Methods (i), (ii) and (iii) all involve the assumption of creeping flow. A complete solution to the creeping equation would be of the form;

$$\psi(r,\theta) = \sum_{2}^{\infty} C_n^{-\frac{1}{2}} \cos\theta [A_n r^2 + B_n \frac{1}{r^{n-1}} + C_n r^{n+2} + D_n \frac{1}{r^{n-3}}]$$

where the use of the stream function automatically satisfies the Continuity equation. A set of boundary conditions which accounts for the indented base of the drop (without, however, including the effect of skirts) (see Figure 5.0) is the following:

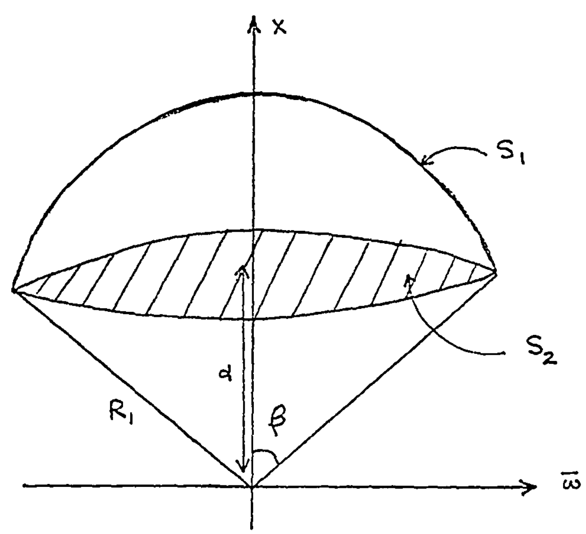

Fig.5.0. Definition sketch for complete boundary conditions on surfaces S_1 and S_2

Far from the drop at $r = \infty$

$$v_r = - U_o \cos \theta$$

and $$v_\theta = U_o \sin \theta.$$

On surface S_1, where $r = R_1$, $\theta \leq \beta$: the boundary conditions are;

$$v_r = v'_r = 0$$

$$v_\theta = v'_\theta \neq 0$$

$$\left(\frac{1}{r}\frac{\partial v_r}{\partial \theta} + \frac{\partial v_\theta}{\partial r} - \frac{v_\theta}{r}\right) = K\left(\frac{1}{r}\frac{\partial v'_r}{\partial \theta} + \frac{\partial v'_\theta}{\partial r} - \frac{v'_\theta}{r}\right).$$

On surface S_2, where $r \cos \theta = d_1$, $\theta \leq \beta$:

$$v_r \cos \theta - v_\theta \sin \theta = 0,$$

$$v'_r \cos \theta - v'_\theta \sin \theta = 0,$$

$$v_r \sin \theta - v_\theta \cos \theta = v'_r \sin \theta + v'_\theta \cos \theta, \text{ and}$$

$$\frac{\partial}{\partial x}(v_r \sin \theta + v_\theta \cos \theta) = K \frac{\partial}{\partial x}(v'_r \sin \theta + v'_\theta \cos \theta)$$

where $$\frac{\partial}{\partial x} = \cos \theta \frac{\partial}{\partial r} - \frac{\sin \theta}{r}\frac{\partial}{\partial \theta}.$$

However, it must be borne in mind that for a liquid drop (or for a bubble), the assumption of creeping flow is not consistent with the deformed shapes implied by the boundary conditions (and observed in practice). As shown by Taylor and Acrivos (1964), a spherical (undeformed) shape is consistent with the complete neglect of the inertia terms in the equation of motion. Therefore, it seemed to us advisable to adopt simpler conditions (methods (i) to (ii)) than the above purely to allow us to test whether any useful result might follow from the low Reynolds number extreme. The actual range of Reynolds number investigated here is $2 \leq Re \leq 20$.

Although the equations obtained using methods (i), (ii) and (iii) fail to predict the terminal velocity correctly, the equation derived by using potential flow assumptions leads to results which agree very well with the experimental results as shown later. This is somewhat surprising in view of the relatively low Reynolds numbers ($2 \leq Re \leq 20$) encountered in this study.

5.1 Method (i), Ellipsoidal Coordinate Approach (Creeping Flow)

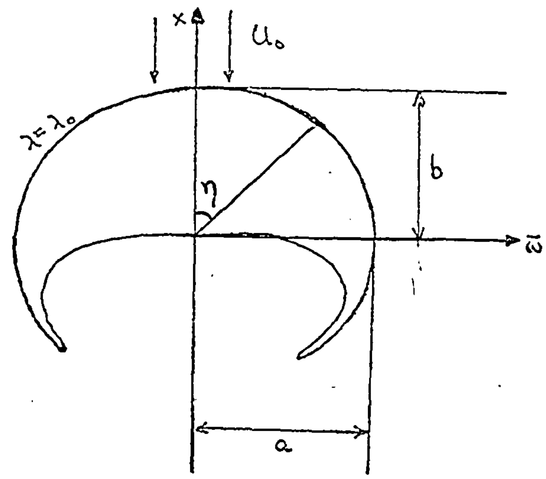

Fig.5.1. Definition sketch for ellipsoidal coordinate method

5.1.1 Assumptions

i The liquids are incompressible.

ii The liquids are Newtonian.

iii Inertia terms are negligible.

iv Axial symmetry is assumed.

v The surface of the drop is ellipsoidal and is given by $\lambda = \lambda_0$, $0 \leq \eta \leq \pi$.

vi Relative to coordinates fixed on the drop, the system is at steady state.

The coordinates (λ, η) are shown in Figure 5.1.

5.1.2 Boundary Conditions

$$\psi = \psi' = 0 \quad \text{at} \quad \lambda = \lambda_0 \tag{1}$$

$$\frac{\partial\psi}{\partial\lambda} = \frac{\partial\psi'}{\partial\lambda} \quad \text{at} \quad \lambda = \lambda_0 \tag{2}$$

$$\left.\begin{aligned} \frac{\partial\psi}{\partial\lambda} &= 0 \\ \frac{\partial\psi'}{\partial\lambda} &= 0 \end{aligned}\right\}^{*} \quad \begin{aligned} \text{at} \quad \lambda &= \lambda_0 \quad \text{and} \\ \eta &= \frac{\pi}{2} M \end{aligned} \tag{3}$$

$$\lim_{\lambda \to \infty} \psi(\overline{\omega}, x) = \frac{1}{2} U_0 c^2(\lambda^2+1)(1-t^2). \tag{4}$$

These boundary conditions correspond physically to no flow across the drop surface, no slip at the interface, no singular point at the corner, and uniform stream flow at infinity.

5.1.3 Solution

The shape of the drop has been approximated by an oblate ellipsoid, Figure 5.1.

Let $z = c \cosh \zeta$ (5)

where $z = x + i\overline{\omega}$

$\zeta = \xi + i\eta$

Then $x = c \cosh \xi \cos \eta$ (6)

$\overline{\omega} = c \sinh \xi \sin \eta$ (7)

---

* This boundary condition is discussed in more detail in 5.2.2., $0 \leq M \leq 2$.

From (6) and (7), since $\sin^2\eta + \cos^2\eta = 1$, we obtain,

$$\frac{\bar{\omega}^2}{c^2\sinh^2\xi} + \frac{x^2}{c^2\cosh^2\xi} = 1 \tag{8}$$

Hence, for constant ξ, we get a confocal family of oblate spheroids whose centre is at the origin. For simplicity, we will write $\sinh\xi = \lambda$ and $\cos\eta = t$.

Now we wish to solve the equation of motion for steady creeping flow, i.e.

$$E^4\psi = 0 \tag{9}$$

where

$$E^2 = \bar{\omega}h^2\left\{\frac{\partial}{\partial\xi}\left(\frac{1}{\bar{\omega}}\frac{\partial}{\partial\xi}\right) + \frac{\partial}{\partial\eta}\left(\frac{1}{\bar{\omega}}\frac{\partial}{\partial\eta}\right)\right\} \tag{10}$$

with

$$h = h_\xi = h_\eta$$

being the usual scaling factors.

It may be shown that a more useful form of Equation (10) is

$$E^2 = \frac{1}{c^2(\lambda^2 + t^2)}\left\{(\lambda^2 + 1)\frac{\partial^2}{\partial\lambda^2} + (1 - t^2)\frac{\partial^2}{\partial t^2}\right\} \tag{11}$$

From boundary condition (4), it is reasonable to assume a solution of the following form,

$$\psi = (1-t^2)f(\lambda) \tag{12}$$

Substituting this in (9), we obtain,

$$E^4\psi = \frac{(\lambda^2+1)(1-t^2)}{c^4(\lambda^2+t^2)}\left\{4(F-\lambda F')+(\lambda^2+t^2)F''\right\} \tag{13}$$

where

$$F = (\lambda^2+1)f'' - 2f$$

After a lengthy but elementary calculation (Appendix A) we get for the external and internal stream functions the following relations,

$$\psi = -(1-t^2)\left\{\frac{1}{2}c_1\lambda - \frac{1}{2}c_2[\lambda - (\lambda^2+1)\cot^{-1}\lambda] - c_3(\lambda^2+1)\right\}$$

.........(14)

and

$$\psi' = -(1-t^2)\left\{\frac{1}{2}c_1'\lambda - \frac{1}{2}c_2'[\lambda - (\lambda^2+1)\cot^{-1}\lambda] - c_3'(\lambda^2+1)\right\}$$

.........(15)

Applying boundary conditions (1), (2), (3), and (4), we can determine the coefficients c_1, c_2, and c_3. The final expression for the external stream function, ψ, becomes

$$\psi = -\frac{1}{2}U_0c^2(1-t^2)\left\{\frac{2\lambda}{K_0} - \frac{\lambda(1-\lambda_0^2)}{K_0} + \frac{(1-\lambda_0^2)(\lambda^2+1)\cot^{-1}\lambda(1-\lambda^2)}{K_0}\right\}$$

$$= -\frac{1}{2}U_0\bar{\omega}^2\left\{\frac{2\lambda}{K_0(1+\lambda^2)} - \frac{\lambda(1-\lambda_0^2)}{K_0(1+\lambda^2)} + \frac{(1-\lambda_0^2)\cot^{-1}\lambda}{K_0} - 1\right\}$$

where

$$K_0 = \lambda_0 - (\lambda_0^2-1)\cot^{-1}\lambda_0$$

The corresponding stream function for an oblated spheroid translating with velocity U_0 in the positive x-direction may be obtained by subtracting the stream function for a uniform stream, $\frac{1}{2}U_0\bar{\omega}^2$,

i.e. $$\psi = -\frac{1}{2}U_0\bar{\omega}^2\left\{\frac{2\lambda}{K_0(1+\lambda^2)} - \frac{\lambda(1-\lambda_0^2)}{K_0(1+\lambda^2)} + \frac{(1-\lambda_0^2)\cot^{-1}\lambda}{K_0}\right\}$$

.......(16)

This solution is similar to that obtained by Payne and Pell (1960) for a rigid ellipsoid. Note that the internal fluid properties do not appear in Equation (16). This is due to boundary condition (3) which imposes zero velocity at a point on the surface; because of the form of solution (Equation 12), zero velocity results over the entire surface as from the "no slip" condition for a rigid body.

The drag force exerted on a complete oblate drop in the fluid, Payne and Pell (1960), is then given by

$$F = 8\pi\mu c \lim_{\lambda\to\infty}\frac{\lambda\psi}{\bar{\omega}^2} - \frac{8\pi\mu c U_0}{K_0} \qquad (17)$$

When the velocity of the drop has reached its steady state value, the only forces acting on the drop are the above drag forces and gravity (buoyancy-weight) forces. Thus, we get for U_0,

$$U_0 = \frac{\Delta\rho\, gabK_1}{6\mu} \tag{18}$$

where $K_1 = \frac{1}{e^2}[\sqrt{1-e^2} - (\frac{1-2e^2}{e})\sin^{-1}e]$

since $\cosh\xi_0 = \frac{1}{e}$, $\sinh\xi_o = \sqrt{\frac{1-e^2}{e^2}}$, and

$$\cot^{-1}\sinh\xi_0 = \sin^{-1}e.$$

where $e = \sqrt{1-(b/a)^2}$.

In the limiting case for a sphere,

$$\lim_{e \to 0} K_1 = \frac{4}{3}$$

as shown in Appendix B. In addition, a = b = sphere radius for e = 0 so that Equation (18) gives the Stoke's rise velocity as a limiting case.

5.2 Method (ii). Spherical Coordinate Approach (Creeping Flow)

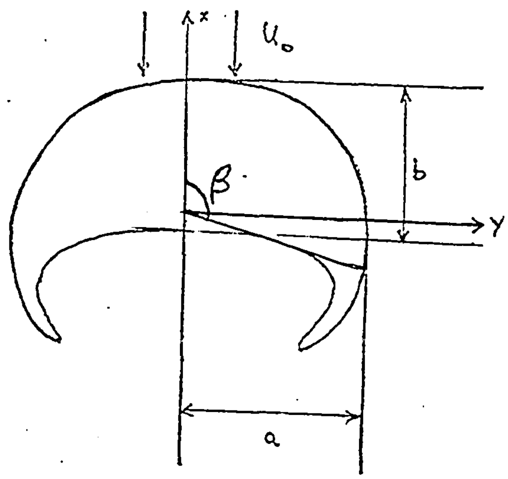

Fig. 5.2. Definition sketch for spherical coordinate method

5.2.1 Assumptions

i The liquids are incompressible.

ii The liquids are Newtonian.

iii Inertia terms are negligible.

iv The system has axial symmetry.

v The surface of the drop is given by $r = R$, $0 \leq \theta \leq \beta$.

vi Relative to coordinates fixed to the rising drop, the system is at steady state.

vii Interfacial tension effects are negligible.

5.2.2 Boundary Conditions*

$$v_r = -U_0 \cos\theta \text{ and } v_\theta = U_0 \sin\theta \text{ at } r = \infty \quad (1)$$

$$v_r = v_r' = 0 \text{ at } r = R \quad (2)$$

$$v_\theta = v_\theta' \neq 0 \text{ at } r = R \text{ and } 0 < \theta < \beta \quad (3)$$

$$\tau_{rr} = \tau_{rr}' \text{ at } r = R \quad (4)$$

$$\tau_{r\theta} = \tau_{r\theta}' \text{ at } r = R \quad (5)$$

$$\left.\begin{array}{l} v_\theta = 0 \\ v_\theta' = 0 \end{array}\right\}^{**} \text{ at } r = R \text{ and } \theta = \beta \quad (6)$$

5.2.3 Solution

Let us assume that gravity is the driving force. The drop is rising vertically in the positive x-direction. To hold the drop stationary, let us apply a force in the negative x-direction to counterbalance the net gravity force. (This is Batchelor's use of a "modified pressure".)

$$F = -\Delta\rho g V \quad (7)$$

---

* We take the coordinates to move with the centre of the rising drop.

** We require the absolute magnitude of the velocity components in the vertical direction at the base (assumed horizontal) to vanish. This then requires that $v_r \sin\theta + v_\theta \cos\theta = \theta$ at every point on the base surface. Therefore, at the singularity point $\theta = \beta$, $r = R$, where $v_r = 0$ and $v_r' = 0$, we must also have $v_\theta = 0$ and $v_\theta' = 0$.

For the outside fluid, the creeping flow equation is

$$\bar{\nabla} p = \mu \nabla^2 \underline{v} - \Delta\rho \, \underline{g} \tag{8}$$

For the inside fluid,

$$\bar{\nabla} p' = \mu' \nabla^2 \underline{v}' \tag{9}$$

The equation of continuity is satisfied for both fluids, i.e.

$$\bar{\nabla} \underline{v} = 0 \tag{10a}$$

$$\bar{\nabla} \underline{v}' = 0 \tag{10b}$$

It is convenient to write

$$\pi = - \Delta\rho g x = \frac{F x}{V}$$

where x is a vertical length coordinate, so that

$$\bar{\nabla} \pi = - \Delta\rho \, \underline{g}$$

and

$$\bar{\nabla}(p - \pi) = \mu \nabla^2 \underline{v} \tag{11}$$

Here we can see that the similarity of (11) and (9) simplifies the computation. Now $\underline{v}$, $\underline{v}'$, p, and p' in Equations (9), (10) and (11) must be solved subject to the appropriate boundary conditions.

In spherical coordinates, (11) becomes

$$\frac{\partial}{\partial r}(p - \pi) = \mu\left\{\frac{\partial^2 v_r}{\partial r^2} + \frac{1}{r^2}\frac{\partial^2 v_r}{\partial \theta^2} + \frac{2}{r}\frac{\partial v_r}{\partial r} + \frac{\cot\theta}{r^2}\frac{\partial v_r}{\partial \theta} - \frac{2v_r}{r^2} - \frac{2\cot\theta v_\theta}{r^2}\right\} \quad .....(12)$$

$$\frac{1}{r}\frac{\partial(p-\pi)}{\partial \theta} = \mu\left\{\frac{\partial^2 v_\theta}{\partial r^2} + \frac{1}{r^2}\frac{\partial^2 v_\theta}{\partial \theta^2} + \frac{2}{r}\frac{\partial v_\theta}{\partial r} + \frac{\cot\theta}{r^2}\frac{\partial v_\theta}{\partial \theta} + \frac{2}{r^2}\frac{\partial v_r}{\partial \theta} - \frac{v_\theta}{r^2\sin^2\theta}\right\} \quad .....(13)$$

while Equation (10a) becomes

$$\frac{\partial v_r}{\partial r} + \frac{1}{r}\frac{\partial v_\theta}{\partial \theta} + \frac{2v_r}{r} + \frac{v_\theta}{r}\cot\theta = 0 \quad (14)$$

The equations of motion and continuity for the inner fluids have the same form.

We try a solution of the following form,

$$v_r = \chi_1(r)\cos\theta \quad (15a)$$

$$v_\theta = \chi_2(r)\sin\theta \quad (15b)$$

$$p - \pi = \mu\chi_3(r)\cos\theta \quad (15c)$$

$$v_r' = \chi_1'(r)\cos\theta \tag{15d}$$

$$v_\theta' = \chi_2'(r)\sin\theta \tag{15e}$$

$$P' = \mu'\chi_3'(r)\cos\theta \tag{15f}$$

Substituting these equations into equations (12), (13), and (14), and with a few assumptions (Appendix C), we obtain

$$v_r = \left(\frac{c_1}{r^3} + \frac{c_2}{r} + c_3 + c_4 r^2\right)\cos\theta \tag{16a}$$

$$v_\theta = \left(\frac{c_1}{2r^3} - \frac{c_2}{2r} - c_3 - 2c_4 r^2\right)\sin\theta \tag{16b}$$

$$P-\pi = \mu\left(\frac{c_2}{r^2} + (10c_4 r\right)\cos\theta \tag{16c}$$

$$v_r' = \left(\frac{c_1'}{r^3} + \frac{c_2'}{r} + c_3' + c_4' r^2\right)\cos\theta \tag{16d}$$

$$v_\theta' = \left(\frac{c_1'}{2r^3} - \frac{c_2'}{2r} - c_3' - 2c_4' r^2\right)\sin\theta \tag{16e}$$

$$P' = \mu'(10c_4' r)\cos\theta \tag{16f}$$

Equation (16) contains eight unknown constants whereas we have nine boundary conditions from Equations (11) to (6), so that one boundary condition is superfluous. If (6) is applied, then because of the form of (15b) and (15e), then v_θ and v_θ' must be 0 for all θ at $r = R$. Then, if the normal stress boundary condition, Equation (4), is left aside as being the superfluous one, it is obvious that we obtain Stoke's solution for a solid sphere.

i.e.
$$U_0 = \frac{2}{9}\frac{\Delta\rho g R^2}{\mu} \tag{17}$$

If, on the other hand, Equation (4) is used and Equation (5) is left aside, the terminal velocity turns out to be

$$U_0 = \frac{6}{19}\frac{\Delta\rho g R^2}{\mu} \tag{18}$$

5.3 <u>Experimental Results, Methods (i) and (ii)</u>

The uniformity of the velocity of rise of the liquid drops may be judged from Figure 5.2.1 where the vertical displacement, x, of the nose of seven drops is plotted against frame number. It is clear that the points for each case are well fitted by straight lines so that any acceleration or deceleration of the drops (eg. caused by unsteady growth of the wake) is negligible. Thus, the velocity of rise, U_0, for all seven drops is reasonably constant over the intervals measured.

The velocities calculated using methods (i) and (ii) * and the corresponding measured velocities are compared in Figure 5.2.2 for diethyl phthalate as the dispersed phase. The results obtained show too steep a slope. This applies also to all the other systems. All the data is tabulated in Tables C1 - C9. From the graph, it appears as if for high U_{calc}

* From equation 18 above

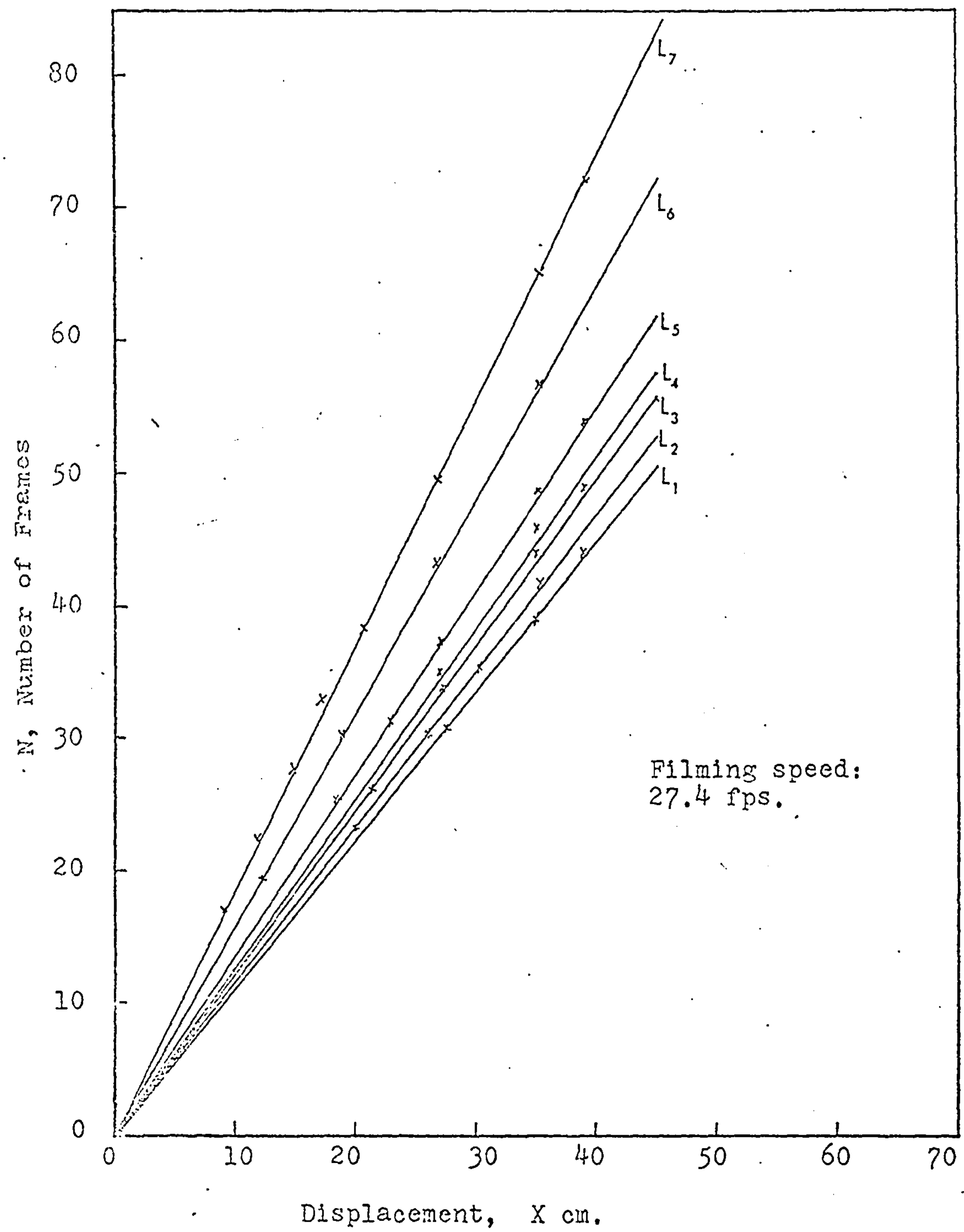

Fig. 5.2.1. Displacement - time curves deduced from photographs of rising drops.

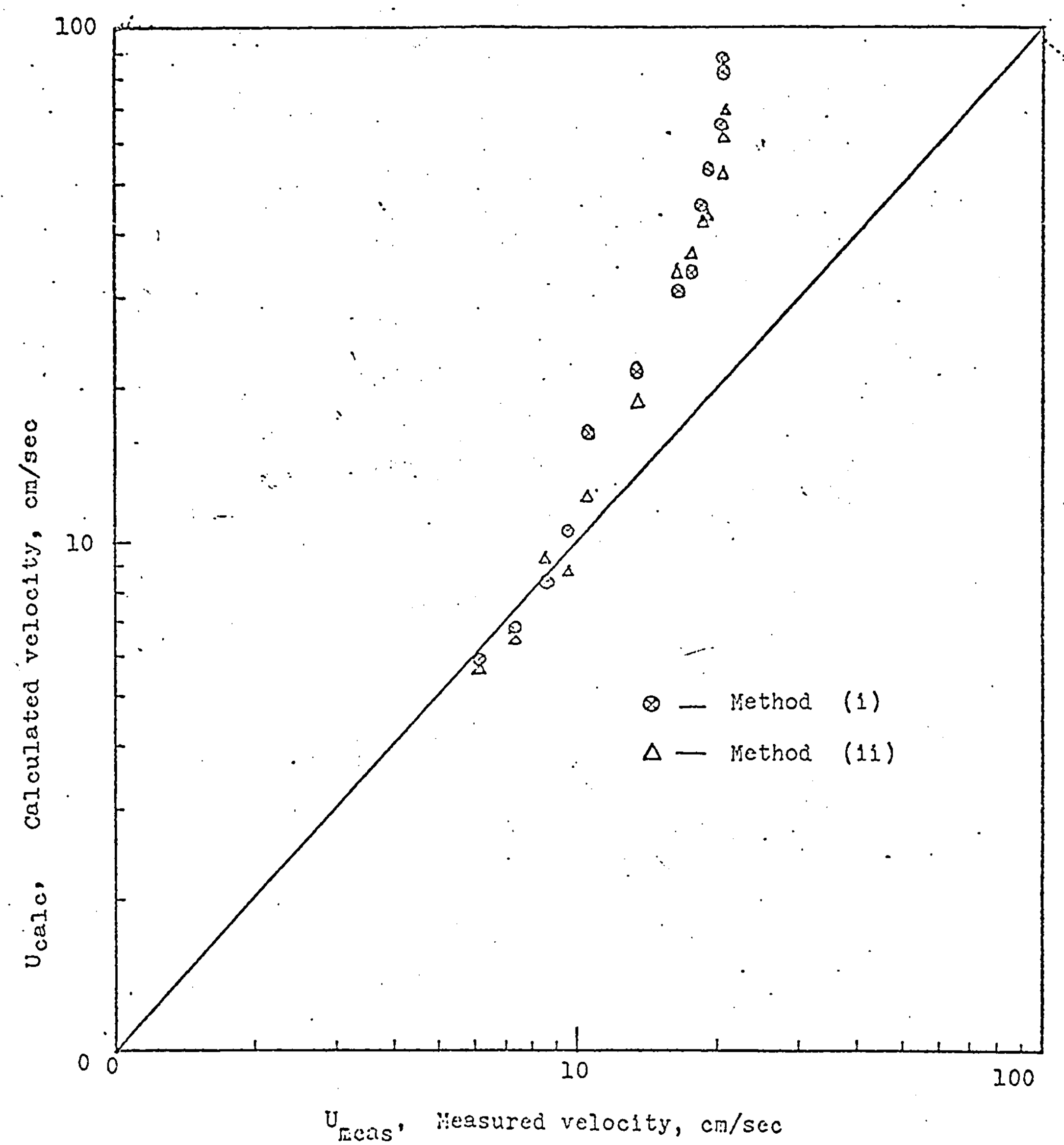

Fig. 5.2.2. Comparison between measured and calculated velocities for o - Diethyl Phthalate drops (27.5°C) in suc. soln.

TABLE C1. Experimental and Calculated Drop Terminal Velocities

1,1,1-Trichloroethane - 27.5°C

Run	Equivalent Diameter d, cm	Measured Velocity U_0, cm/sec	Calculated Velocity Meth(i) U, cm/sec	Calculated Velocity Meth(ii) U, cm/sec	Calculated Velocity Meth(iv) U, cm/sec
1	2.44	3.59	1.65	2.74	5.16
2	2.96	4.10	2.31	2.36	5.67
3	——	——	——	——	——
4	4.44	4.70	7.64	7.33	7.70
5	4.79	7.79	9.32	10.58	7.92
6	5.18	8.77	10.88	12.35	8.39
7	6.04	9.88	15.65	12.40	9.41
8	6.12	9.80	15.86	22.06	9.68
9	6.21	10.04	15.74	17.72	9.70
10	6.37	10.37	18.68	18.64	10.01
11	6.55	10.37	18.53	19.77	10.18
12	6.65	10.37	20.31	20.32	10.30
13	7.09	10.10	24.12	23.10	10.74

TABLE C2. Experimental and Calculated Drop Terminal Velocities

o-Dichlorobenzene - 27.8^{o}C

Run	Equivalent Diameter d, cm	Measured Velocity U_0, cm/sec	Calculated Velocity Meth(i) U, cm/sec	Calculated Velocity Meth(ii) U, cm/sec	Calculated Velocity Meth(iv) U, cm/sec
1	———	———	———	———	———
2	3.72	7.21	7.95	9.30	8.25
3	4.21	7.95	9.71	11.90	9.01
4	4.38	8.31	11.76	12.86	9.01
5	———	———	———	———	———
6	5.25	10.46	16.67	18.50	10.18
7	5.56	10.29	21.07	20.71	10.76
8	2.59	10.20	18.91	9.74	10.65
9	6.17	11.11	26.01	25.55	11.63
10	6.31	11.21	25.39	26.72	11.51
11	6.33	11.21	21.65	26.89	11.89
12	6.74	11.73	28.50	30.44	12.40
13	6.90	12.30	32.64	31.90	12.75
14	6.93	11.95	35.11	32.22	12.73
15	7.11	12.55	42.85	33.92	13.36

TABLE C3. Experimental and Calculated Drop Terminal Velocities

1,2-Dichloroethane - 27.5°C

Run	Equivalent Diameter d, cm	Measured Velocity U_0, cm/sec	Calculated Velocity Meth(i) U, cm/sec	Calculated Velocity Meth(ii) U, cm/sec	Calculated Velocity Meth(iv) U, cm/sec
1	1.69	3.39	2.13	2.65	6.44
2	2.13	6.00	4.52	4.20	7.92
3	3.08	7.02	6.15	8.73	8.64
4	3.19	8.31	6.70	9.34	8.99
5	3.48	8.60	9.66	11.14	9.69
6	4.01	9.80	12.45	14.84	10.46
7	4.14	10.37	14.22	16.08	10.73
8	4.14	10.63	16.93	18.14	11.24
9	4.70	11.51	19.03	20.33	11.77
10	5.59	12.94	31.47	28.82	13.45
11	5.89	13.21	28.39	31.99	13.61
12	6.40	13.77	38.80	37.70	14.75
13	6.63	14.94	57.46	39.67	15.51
14	7.15	15.69	49.85	47.12	15.90

TABLE C4. Experimental and Calculated Drop Terminal Velocities

o-Diethyl Phthalate - 27.8°C

Run	Equivalent Diameter d, cm	Measured Velocity U_0, cm/sec	Calculated Velocity Meth(i) U, cm/sec	Calculated Velocity Meth(ii) U, cm/sec	Calculated Velocity Meth(iv) U, cm/sec
1	1.86	7.43	6.42	6.46	10.02
2	2.13	8.54	9.01	8.50	10.67
3	2.35	9.65	7.84	10.34	10.88
4	2.96	10.37	12.11	16.34	11.92
5	3.39	13.49	18.84	21.50	13.38
6	4.08	16.30	33.33	31.04	16.11
7	4.27	16.09	32.99	34.08	16.34
8	4.32	17.43	35.98	34.81	47.04
9	4.38	16.30	32.63	35.79	16.38
10	4.54	16.96	32.51	38.45	17.22
11	4.88	18.73	41.41	44.42	17.89
12	5.34	19.02	43.01	53.19	17.83
13	6.31	20.24	52.90	67.48	18.56
14	6.73	20.92	61.72	84.60	19.46
15	6.79	22.02	68.12	86.09	20.02

TABLE C5. Experimental and Calculated Drop Terminal Velocities

Paraffin Oil A - 26.5°C

Run	Equivalent Diameter d, cm	Measured Velocity U_0, cm/sec	Calculated Velocity Meth(i) U, cm/sec	Calculated Velocity Meth(ii) U, cm/sec	Calculated Velocity Meth(iv) U, cm/sec
1	2.53	13.12	15.41	20.08	15.37
2	3.08	16.48	25.12	29.64	18.12
3	3.73	19.26	34.56	43.59	20.65
4	3.88	19.49	40.73	45.84	21.14
5	4.49	21.03	41.71	62.05	21.65
6	4.60	21.35	36.17	66.11	21.56
7	5.06	21.80	34.65	79.66	21.08
8	5.14	21.80	31.88	82.55	20.82
9	5.18	21.80	38.33	77.36	21.58
10	5.22	21.80	38.78	85.13	21.67
11	5.66	21.80	35.12	100.10	21.11
12	6.21	23.02	55.03	120.69	23.40
13	6.12	22.16	40.86	117.03	22.30

TABLE C6. Experimental and Calculated Drop Terminal Velocities

Silicone Oil B - 25.4°C

Run	Equivalent Diameter d, cm	Measured Velocity U_0, cm/sec	Calculated Velocity Meth(i) U, cm/sec	Calculated Velocity Meth(ii) U, cm/sec	Calculated Velocity Meth(iv) U, cm/sec
1	1.86	———	———	———	———
2	2.13	9.30	6.31	10.32	12.00
3	2.53	11.62	10.86	14.54	13.63
4	2.96	14.59	18.36	19.82	16.00
5	3.13	14.91	16.48	22.24	16.05
6	3.29	14.91	18.15	24.57	16.01
7	3.80	18.03	31.32	32.67	18.72
8	4.01	18.89	35.31	36.47	19.19
9	4.27	19.79	37.46	41.35	20.23
10	4.44	19.79	35.07	44.61	19.83
11	4.88	21.10	41.42	53.32	21.02
12	5.41	21.92	35.65	66.34	20.71
13	5.73	22.81	41.21	74.17	21.30
14	6.18	23.66	———	———	———
15	6.75	24.17	35.08	94.07	20.62

TABLE C7. Experimental and Calculated Drop Terminal Velocities

Silicone Oil ACI - 27.8^{o}C

Run	Equivalent Diameter d, cm	Measured Velocity U_0, cm/sec	Calculated Velocity Meth(i) U, cm/sec	Calculated Velocity Meth(ii) U, cm/sec	Calculated Velocity Meth(iv) U, cm/sec
1	1.86	7.85	8.36	10.74	12.11
2	3.08	13.16	23.80	35.16	16.93
3	3.19	13.65	25.42	31.67	17.46
4	4.10	15.37	39.30	52.90	20.57
5	4.60	15.80	43.10	66.63	21.21
6	4.30	16.05	35.29	71.01	19.61
7	5.69	16.05	42.21	100.60	20.73

TABLE C8. Experimental and Calculated Drop Terminal Velocities

Silicone Oil ABI - 27.8^{o}C

Run	Equivalent Diameter d, cm	Measured Velocity U_0, cm/sec	Calculated Velocity Meth(i) U, cm/sec	Calculated Velocity Meth(ii) U, cm/sec	Calculated Velocity Meth(iv) U, cm/sec
1	3.08	13.99	23.02	29.42	16.30
2	4.10	20.45	52.70	52.14	21.25
3	4.32	18.48	57.99	57.88	21.18
4	4.38	18.73	48.16	59.51	20.50
5	4.84	19.75	44.90	72.67	20.78
6	5.10	20.87	57.92	80.68	21.84
7	5.34	20.45	51.05	88.45	21.20
8.	6.10	20.14	45.74	115.42	20.73
9	6.21	21.66	67.16	119.42	22.49

TABLE C9. Experimental and Calculated Drop Terminal Velocities

Silicone Oil A - 27.5°C

Run	Equivalent Diameter d, cm	Measured Velocity U_0, cm/sec	Calculated Velocity Meth(i) U, cm/sec	Calculated Velocity Meth(ii) U, cm/sec	Calculated Velocity Meth(iv) U, cm/sec
1	2.35	13.86	17.19	17.20	15.86
2	3.08	17.32	25.64	29.42	18.01
3	4.32	22.00	58.47	57.88	22.51
4	4.38	22.34	65.31	59.50	23.04
5	4.74	23.18	73.47	69.68	23.72
6	4.79	24.09	79.96	74.28	24.22
7	5.02	24.69	61.63	78.15	23.61
8	5.66	26.29	111.30	88.82	26.25
9	5.95	26.29	110.48	109.98	26.35
10	6.50	26.78	113.01	131.03	26.90

the measured velocities begin to veer upwards while for small $U_{calc.}$, the velocities differ only slightly. This suggests that for drops of small diameter, these equations may be used to estimate the rising velocity; however, as the drop diameter increases, agreement becomes poor. This agrees with the earlier warning that our assumptions are only valid for spherical drops at low Reynolds numbers. These conditions do not apply in our systems.

5.4 Method (iii), Semi-Empirical Approach

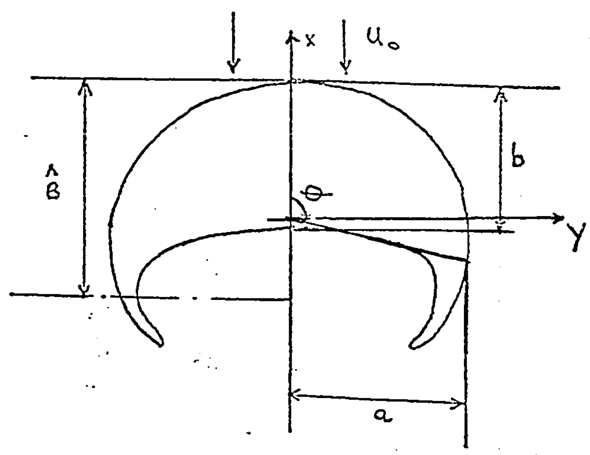

Fig.5.3. Definition sketch for semi-empirical method

Using spherical coordinates and oblate coordinates, for creeping flow, we have obtained expressions for the terminal velocity of the following forms;

$$U_0 \propto \frac{\Delta\rho g R^2}{\mu} \tag{1}$$

$$U_0 \propto \frac{\Delta\rho g}{\mu} K_1 ab \tag{2}$$

where K_1 was defined in Section 5.1.3. It may be noted that the Hadamard solution is also of the form of (1).

In view of the above, it is reasonable to assume a general expression (for creeping flow) of the following form;

$$U_0 \propto \frac{\Delta\rho g}{\mu} L^2 \tag{3}$$

where L is a characteristic length. We can assume that the constant of proportionality is a function of shape. With the hope of establishing a relationship between the constant of proportionality and expression (3), the following three approaches have been considered;

(i) Sphericity, ψ_s = $\dfrac{\text{Area of spherical drop of equivalent volume}}{\text{Actual surface area of drop}}$

(ii) Drop shape parameter, $\psi_\phi = \left(\dfrac{a+b}{\hat{B}}\right)^{\frac{1}{2}}$

where $\hat{B}$ is as shown in Figure 5.3.

(iii) Circularity, ψ_c = $\dfrac{\text{Sphere equivalent diameter}}{\text{Diameter of a drop with same cross-sectional area as that of the particle projected in the direction of motion.}}$

Each of these parameters can be calculated from the photographs, although calculations of the drop surface area are rather tedious and require coordinates of a series of points. In each case, (3) leads to

$$\frac{\mu U_0}{\Delta\rho g L^2} = F(\psi) \qquad (4)$$

where ψ is the relevant shape parameter*.

In view of the discrepancy between the experimental results and methods (i) and (ii), and the fact that it is clear that no single parameter adequately represents the range of shapes observed in this work, this approach was not pursued any further.

Before applying either the sphericity of circularity method, the surface area and the volume of the drop must be obtained. One method of achieving this is by using a simple but suitable technique, the trapezoidal rule, (McCracken & Dorn, p.161).

The expressions for the surface area and the volume of the drop have been derived, Appendix D. They are;

$$A_s = \sum_{i=0}^{R-1} \pi(r_{i+1} + r_i)((z_{i+1} - z_i)^2 + (r_{i+1} - r_i)^2)^{\frac{1}{2}}$$

---

* $\frac{\mu U_0}{\Delta\rho g L^2}$ is the reciprocal of the Jeffrey number which is a ratio of gravity to viscous flow.

and $$V_d = \frac{\pi}{2} \sum_{i=0}^{n-1} (r_i^2 z_{i+1} - r_{i+1}^2 z_i)$$

A simple computer program has been written to perform these calculations. Only pairs of values of the position coordinates, z_i and r_i, are required as input data. From the diagram given in the appendix, it is seen that $r_0 = r_n = 0$.

In order to achieve a higher degree of accuracy, a correction for the truncation underestimates has also been derived and is given in Appendix D(c).

5.5 Oblate Spheroid Method (Potential Flow)

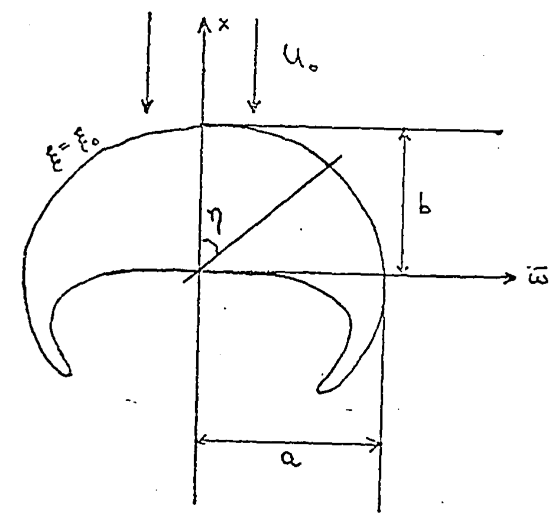

Fig.5.4. Definition sketch for oblate spheroid method

5.5.1 Assumptions

i The flow of the external liquid is irrotational.

ii The variation of pressure near the drop nose is negligible.

iii Surface tension forces are negligible.

iv The effect of the wake and the skirts at the concave region are negligible.

v Axial symmetry is assumed.

vi The system is assumed to be at steady state relative to an origin fixed on the drop.

vii The shape of the drop is assumed to be approximated by an oblate spheroid.

5.5.2 Solution

Let $Z = f(\zeta) = c \sinh\zeta$ (1)

where $z = x + i\bar{\omega}$ and $\zeta = \xi + i\eta$ (2)

Then, $x = c \sinh \xi \cos\eta$ (3)

$\bar{\omega} = c \cosh \xi \sin\eta$ (4)

An oblate ellipsoidal surface is then given by $\xi = \xi_o$

from where we find the semi-axes to be

$$a = c \cosh \xi_0 \quad \text{and} \quad b = c \sinh \xi_0$$

The stream function for an oblate ellipsoid moving with a velocity U_0 along the x-axis relative to stagnant fluid (Milne-Thomson, p.499) is given by,

$$\psi = \frac{-\frac{1}{2} U_0 c^2 (\sinh \xi - \cosh^2 \xi \cot^{-1} \sinh \xi) \sin^2 \eta}{K_3} \tag{5}$$

where $K_3 = e\sqrt{1-e^2} - \sin^{-1} e$

Milne-Thomson has derived an equation to enable the calculation of the tangential velocity, q_η;

$$q_\eta = \left(\frac{1}{J_{\overline{\omega}}} \frac{\partial \psi}{\partial \xi}\right)_\xi$$

$$\text{or} \quad q_0 = \left(\frac{1}{J_{\overline{\omega}}} \frac{\partial \psi}{\partial \xi}\right)_{\xi=\xi_0} \tag{6}$$

since the velocity normal to the drop surface is 0.

J is defined by;

$$J^2 = f'(z)\overline{f}'(\overline{z})$$

$$\text{Hence} \quad J = c(\cosh^2 \xi \cos^2 \eta + \sinh^2 \xi \sin^2 \eta)^{\frac{1}{2}} \tag{8}$$

By superimposing a uniform stream of velocity U_0 in the negative x-direction, we obtain for streaming past an oblate ellipsoid,

$$\psi = -\frac{U_0 c^2}{2K_3} \left\{K_3 \cosh^2 \xi - (\sinh \xi - \cosh^2 \xi \cot^{-1} \sinh \xi)\right\} \times \sin^2 \eta \tag{9}$$

Now
$$\frac{\partial\psi}{\partial\xi} = -\Lambda\left\{2K_3\cosh\xi\sinh\xi - \cosh\xi + 2\cosh\xi\ \sinh\xi\ \cot^{-1}\sinh\xi - \sinh\xi\right\} \qquad (10)$$

where
$$\Lambda = \frac{U_0c^2\sin^2\eta}{2K_3}$$

But
$$\frac{\partial}{\partial\xi}(\cot^{-1}\sinh\xi) = \left(\frac{-1}{1+\sinh^2\xi}\right)\cosh\xi$$

Therefore
$$\frac{\partial\psi}{\partial\xi} = -2\Lambda\cosh\xi\left\{K_3\sinh\xi - 1 + \sinh\xi\cot^{-1}\sinh\xi\right\} \qquad \ldots\ldots.(11)$$

which, on substituting into (6) gives,

$$q_0 = \frac{-2\Lambda\sinh\xi_0\left\{K_3\sinh\xi_0 - 1 + \sinh\xi_0\cot^{-1}\sinh\xi_0\right\}}{c\,(\cosh^2\xi_0\cos^2\eta + \sinh^2\xi_0\sin^2\eta)^{\frac{1}{2}}c\,\cosh\xi_0\sin\eta} \qquad \ldots\ldots.(12)$$

But
$$\cosh\xi_0 = \frac{1}{e}, \quad \sinh\xi_0 = \sqrt{\frac{1-e^2}{e^2}}, \quad \text{and}$$

$$\cot^{-1}\sinh\xi_0 = \sin^{-1}e$$

Therefore
$$q_0^{\,2} = \frac{-U_0^{\,2}e^6\sin^2\eta}{(K_3)^2\left\{(1-e^2)\sin^2\eta + \cos^2\eta\right\}} \qquad (13)$$

Application of Bernoulli's equation to the outside fluid between the stagnation point at the nose and another point on the surface yields,

$$p = p_s + \rho g b(1 - \cos\eta) - \frac{\rho q_0^2}{2} \tag{14}$$

where p_s is the pressure at the stagnation point. For $K = \mu'/\mu \ll 1$, the Reynolds number for the internal motion is much greater than that for the external motion, $Re' = \rho' U_0 de/\mu' \gg 1$. Thus, it is reasonable to think in terms of a thin interior boundary layer (see Harper and Moore, 1968) upon which the pressure is imposed by the interior fluid which is moving slowly. As a reasonable approximation then, we may take the pressure distribution on the inside surface of the drop as corresponding to the hydrostatic pressure variation of the interior fluid. Thus, we may write

$$p = p_s + \rho' g b(1 - \cos\eta) \tag{15}$$

Combining (14) and (15), we may write

$$q_0^2 = 2 \frac{\Delta\rho}{\rho} g b(1 - \cos\eta) \tag{16}$$

where $\Delta\rho = \rho - \rho'$. It may be noted that Harrison et al (1961) arrived at a similar result by assuming the dispersed phase fluid to be stagnant, a condition which would violate continuity of fluid velocity at the interface. Here we assume that the interior pressure is the same as for a stagnant fluid without implying that the dispersed fluid is actually stationary relative to axes moving with the drop.

We may now combine (14) and (16) and require that the resulting equation be satisfied in the limit as $\eta \to 0$ (analogous to the well-known Davies and Taylor, 1951, treatment for spherical-cap bubbles and to the Grace and Harrison, 1967, solution for prolate ellipsoidal-cap bubbles). Thus,

$$U_0^2 = \lim_{\eta \to 0} 2gb \frac{\Delta\rho}{\rho} \frac{K_3^2}{e^6} \left(\frac{1-\cos\eta}{\sin^2\eta}\right) \left\{(1-e^2)\sin^2\eta + \cos^2\eta\right\}$$

so that $$U_0 = K_3^b \left(gb \frac{\Delta\rho}{\rho}\right)^{\frac{1}{2}} \tag{17}$$

or $$U_0 = K_3^a \left(ga \frac{\Delta\rho}{\rho}\right)^{\frac{1}{2}} \tag{18}$$

where $$K_3^b = \frac{1}{e^3}\left(\sin^{-1}e - e\sqrt{1-e^2}\right) \tag{19}$$

and $$K_3^a = \sqrt[4]{1-e^2}\, K_3^b \tag{20}$$

In the limiting case as $e \to 0$ (or $b \to a$), then $K_3^b = K_3^a = 2/3$ as shown in Appendix E.

5.5.3 Experimental Results, Method (iv)

A comparison of the velocities calculated from method (iv) and the measured velocities is shown in Figure 5.4.1 for eight dispersed fluids: silicone oils A, B, and AB1, paraffin oil A, o-diethyl phthalate, 1,2-dichloroethane, o-dichlorobenzene, and 1,1,1-trichloroethane.

It is clear that the calculated velocities show remarkably good agreement with the measured values despite the arbitrary assumption that the flow can be described as irrotational and despite the fact that the stream function was calculated for a complete oblate spheroid. Furthermore, no allowance has been made for the presence of dimples and skirts at the rear of the drop.

For large drops where surface tension forces are negligible and where the internal fluid viscosity is much less than the field fluid viscosity, the external fluid encounters little resistance at the interface. Thus there is non-zero velocity at the drop surface (as for potential flow past a body) and vorticity generation is relatively small. This no doubt accounts for the fact that the potential flow model applies down to such relatively low Reynolds numbers, just as the Davies and Taylor model applies for bubbles down to similar Reynolds numbers, Davenport et al (1967).

Also, it will be noted in Figure 5.4.~~4~~1 that agreement is most favourable for larger liquid drops. For the smaller drops, the equation, $U_0 = K_3 b(\frac{\Delta\rho}{\rho} gb)^{\frac{1}{2}}$, overestimates the velocities. We would expect the potential flow assumption to be more valid at higher Reynolds numbers and this is borne out by the results shown in the figure.

Finally, it must be pointed out that the characteristic lengths a and b were not well-defined in some cases, and hence the eccentricity e is subject to considerable experimental error. Nevertheless, the final agreement for U_0 is so favourable that Equation (17) can be accepted for large drops rising in systems where $K = \mu'/\mu \ll 1$. For the systems covered in this investigation, $E_0 > 7$, $1 < Re < 20$, $K < 0.03$ and $\gamma = \rho'/\rho < 0.94$. Finally, it should be noted that Equation (17) allows calculation of the drop terminal rising velocity, but only if one already knows the shape. In this sense, again it is similar to results for large spherical-cap bubbles rising in liquids. The full results, including the measured shape parameters, are presented in Tables B1 - B9.*

It is also possible to fit results of Fararoui and Kintner (1961) using Equation (17). However, a certain amount of guesswork is involved in interpreting their data. In particular, they have not given the scale of their photographs. In addition, the results of Shoemaker and Chazal (1969) are at higher Reynolds numbers than ours and the physical properties of the liquids are not clearly specified so that a direct comparison is impossible.

* The data in Table C7 exhibited the poorest agreement. As shown in Table A, silicone oil AC1 which has the highest viscosity produced unsteady drops. These drops were unsuitable for measuring a and b and hence were not plotted

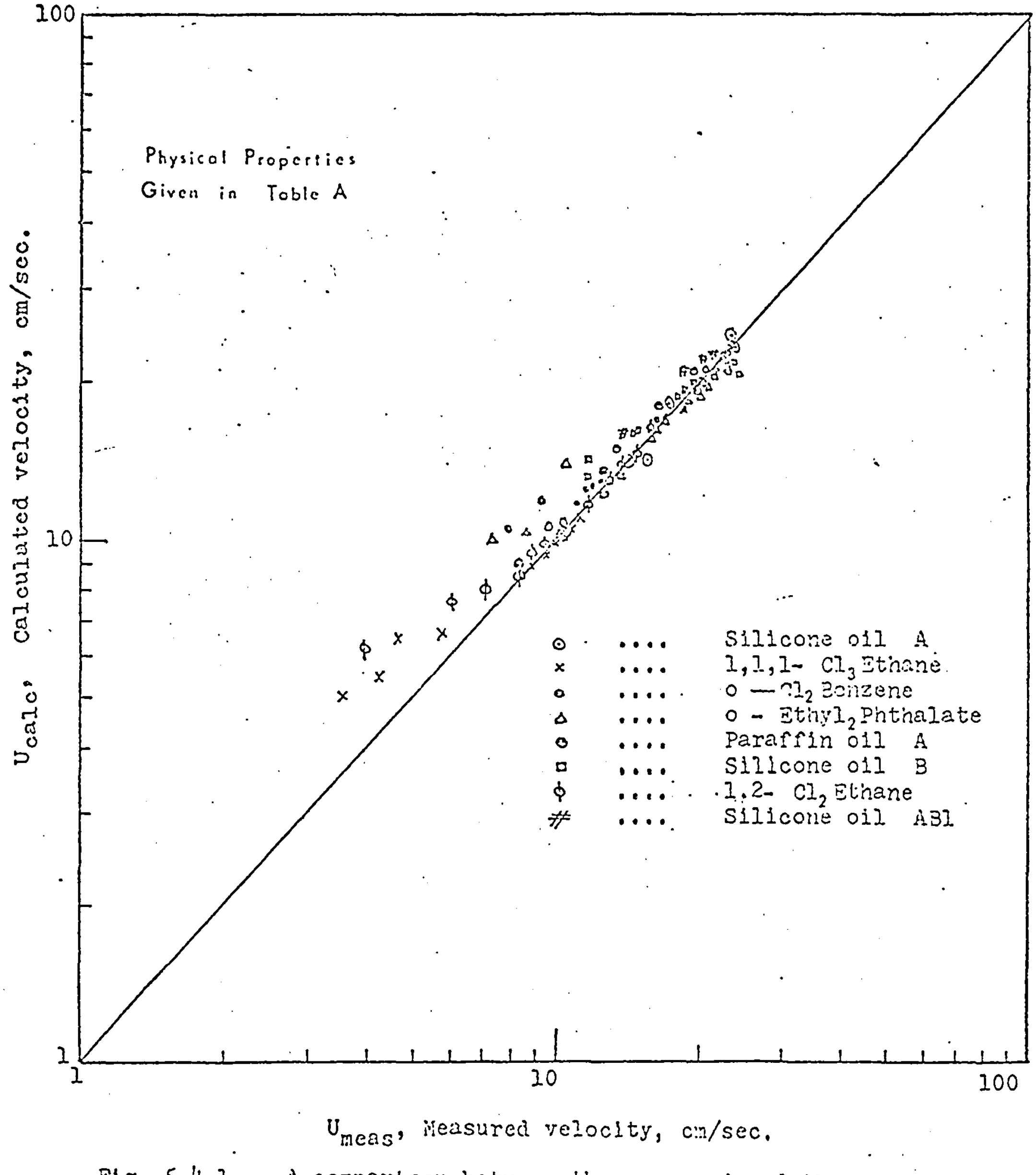

Fig. 5.4.1. A comparison between the measured and the calculated velocities for eight systems.

CHAPTER 6

DIMPLE FORMATION AND THE DEVELOPMENT OF SKIRTS

6.0 Earlier Speculations

In an attempt to explain the causes of flattening and dimpling at the rear of a liquid drop moving through another liquid of higher viscosity, Garner *et al.* (1957) based their argument on the pressure balance between interfacial tension, hydrostatic pressure, and the hydrodynamic pressure due to the external liquid. They did not mention the effect of the wake region behind the drop which may well play an important part in the dimple formation and the development of skirts at the rear of the drop. Furthermore, they only considered Reynolds numbers ranging from 0.0001 to 1.6 which is too small a range for any generalizations on dimpled drops to be made.

On the other hand, Shoemaker and Chazal (1969) believed that dimples and skirts found at the trailing end of large drops moving in high viscosity media were due to stable vortices in the wake of the drop and to internal circulation within the drop. Neither Garner *et al.* nor Shoemaker and Chazal attempted to offer any explanation of why liquid drops moving through a fluid of lower viscosity (e.g. raindrops falling through air) have a flattened surface at their nose instead of at their rear. This interesting question does not appear to have received any attention.

6.1 Qualitative Explanation for the Difference in Shape Between Cases Where $\mu' \ll \mu$ and $\mu' \gg \mu$

The main difference here is the Reynolds number for the two cases. In our system where $\mu' \ll \mu$, the typical range of Reynolds numbers was between 2 and 20. On the other hand, a raindrop falling through air attains Reynolds number of about 7,000. In addition, the Eötvos number for falling drops never exceeds about 20, Merrington and Richardson (1947) , whereas for our case, the Eötvos number was always greater than 7 and commonly greater than 40. Thus surface tension forces continue to play a significant role for deformed drops falling through a gas whereas interfacial tension forces are negligible for the dimpled drops encountered here in liquid-liquid systems. In view of the large difference in Reynolds numbers, we would expect large differences in flow patterns and hydrodynamic pressure distributions even if the shapes were identical, LeClair (1970). For example, it is reasonable to expect boundary layer separation for the high Re case but not at Reynolds numbers of the order of 20 or smaller. Hence, it is not surprising that the equilibrium shapes differ widely in the two cases.

6.2 The Case where $\mu' \ll \mu$

Here, as we have already mentioned, it has been extremely difficult to conceive what factors are controlling the formation of dimples and skirts. Firstly, the range of Reynolds number is too low to think in terms of boundary layer separation. Secondly, the appearance of dimples is observed at such low Reynolds numbers that the development of a wake cannot be attributed to it. For example, as stated above, a standing eddy for flow past a solid sphere does not occur until a Reynolds number of about 20. In addition, as the drop size is increased, the shape of the rear changes from spherical (1) to one with a flattened rear (2). The curvature then becomes negative (3) and skirts begin to form. This is then followed by concave surfaces with smooth curved skirts (4). The waves then set in as the downward skirts straighten (5), and finally the drop motion becomes unsteady and the skirts wobbly (6), Figure 6.1. Bearing these factors in mind, we hope to explain the course of these shape changes in a simple but reasonable qualitative manner. Although the shapes exhibited by a drop can be categorised by some convenient dimensionless groups, it is rather difficult to devise groups for liquid drops, Grace (1972), and we have chosen to classify them according to the nature of the shape observed from the experiments, Figures 6.1. and 6.2.

6.2.1 Spherical or Almost Spherical Drops

This is the case where the interfacial tension forces or viscous forces predominate. The drop assumes a spherical shape or it is distorted to such a small degree that non-zero eccentricity is not observable. As stated before, drops of this shape have been thoroughly examined analytically and experimentally.

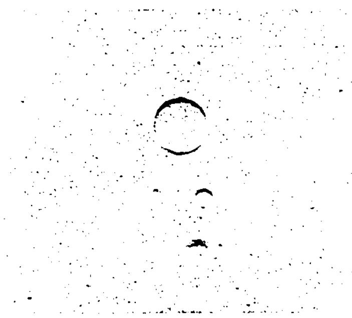

(1) Spherical

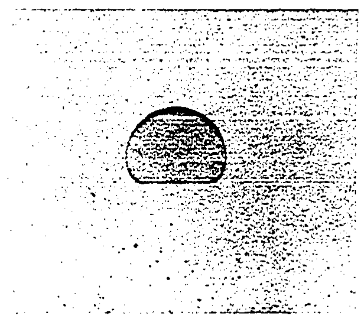

(2) Flattened Rear

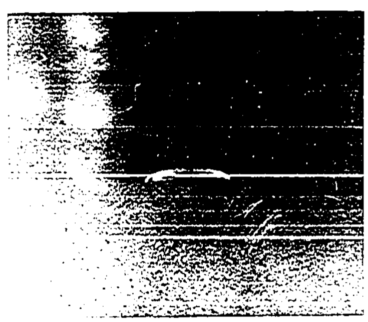

(3) Indented Drop

(4) Smooth Curved Skirt

(5) Skirt Straightened Downwards

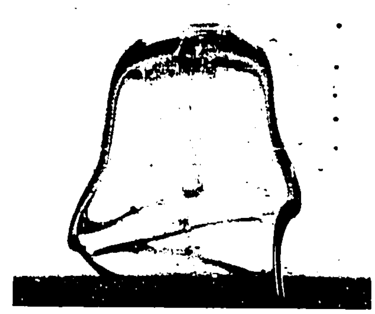

(6) Unsteady and Wobbly Skirt

Fig.6.1. Typical shape of large drops of o-diethyl phthalate rising through aqueous sugar solution.

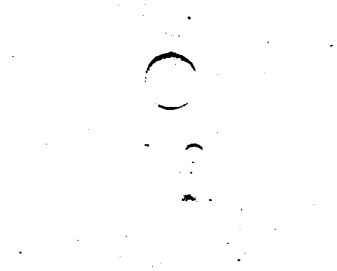

(1) Spherical

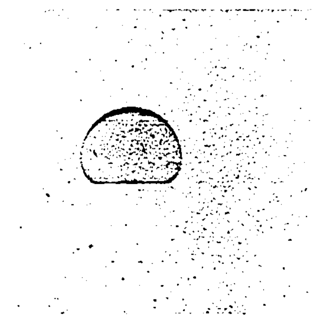

(2) Flattened Rear

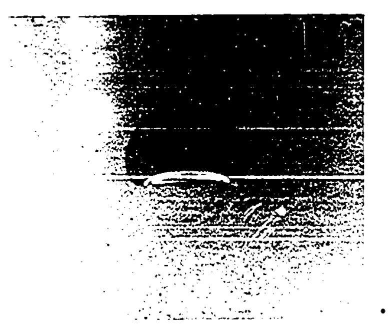

(3) Indented Drop

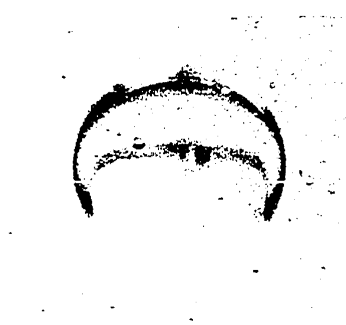

(4) Smooth Curved Skirt

(5) Skirt Straightened Downwards

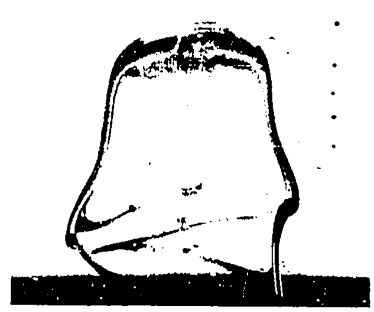

(6) Unsteady and Wobbly Skirt

Fig.6.1. Typical shape of large drops of o-diethyl phthalate rising through aqueous sugar solution.

6.2.2 Drops with Flattened Rear

Saito (1913) was the first person to predict that a drop moving through viscous fluid will deform into an oblate or prolate spheroid. He used the Hadamard-Rybczinski (1911) approach for low Reynolds numbers and took into account the non-linear inertia terms in the equation of motion and the capillary action. He obtained the following equation:

$$\Delta_s = \frac{dU_0^2}{32\sigma(1+K)^3}\left[\frac{\rho'}{3}(1+K) - \rho\left(\frac{K}{20}\right)^3 + \frac{37}{5}K^2 + \frac{319}{20}K + \frac{10}{3}\right]$$

The drop will deform into an oblate or prolate spheroid depending on whether $\Delta_s' < 0$ or $\Delta_s' > 0$ where Δ_s' is the term in the square brackets. This same problem was revised by Taylor and Acrivos (1964) who found a fundamental error in Saito's work. In their approach, Taylor and Acrivos showed that as the Weber number increases, the drop will deform first into an oblate spheroid (which qualitatively but not quantitatively agrees with Saito's work) and then with a further increase in Weber number, into a geometry having a rounded top and flattened rear. They used a singular-perturbation solution of the axi-symmetric equation of motion and arrived at a final solution;

$$\Delta_{TA} = -\alpha We P_2(\xi) - \frac{3\alpha(11K+10)}{70(1+K)}\frac{We^2}{Re}P_3(\xi) + \ldots\ldots$$

where $$\alpha = \frac{1}{4(1+K)^3}\left\{\left(\frac{81}{80}K^3 + \frac{57}{20}K^2 + \frac{103}{40}K + \frac{3}{4}\right) - \frac{\gamma-1}{12}(1+K)\right\}$$

In our opinion, Taylor and Acrivos' explanation for the flattening of drops at the rear seems more convincing than the oversimplified one by Garner et al.. However, the solution is limited to small deviations from the spherical and to low Re and We so that it is unable to cope with the radical deformations observed in this study.

6.2.3 Onset of Skirt Formation

Seven distinct stages can be distinguished in the development of the shape of drops in the viscous liquid employed here. These stages are shown on the following page in Figure 6.2.

Figure 6.2 - Stages in drop shape development in viscous liquid:

(a) Spherical drop

(b) Nearly spherical but with flattening at rear pole.

(c) Dimpled drop

(d) Onset of skirt formation

(e) Fully developed skirt pinched inwards

(f) Skirt straightened downwards

(g) Unsteady skirt, growing with time and asymmetric.

In this section, a qualitative explanation for this evolution of drop shape is provided which is consistent with what evidence is available on the flow patterns and skirt formation. Further experimental work is required to confirm this qualitative picture and to allow quantitative predictions.

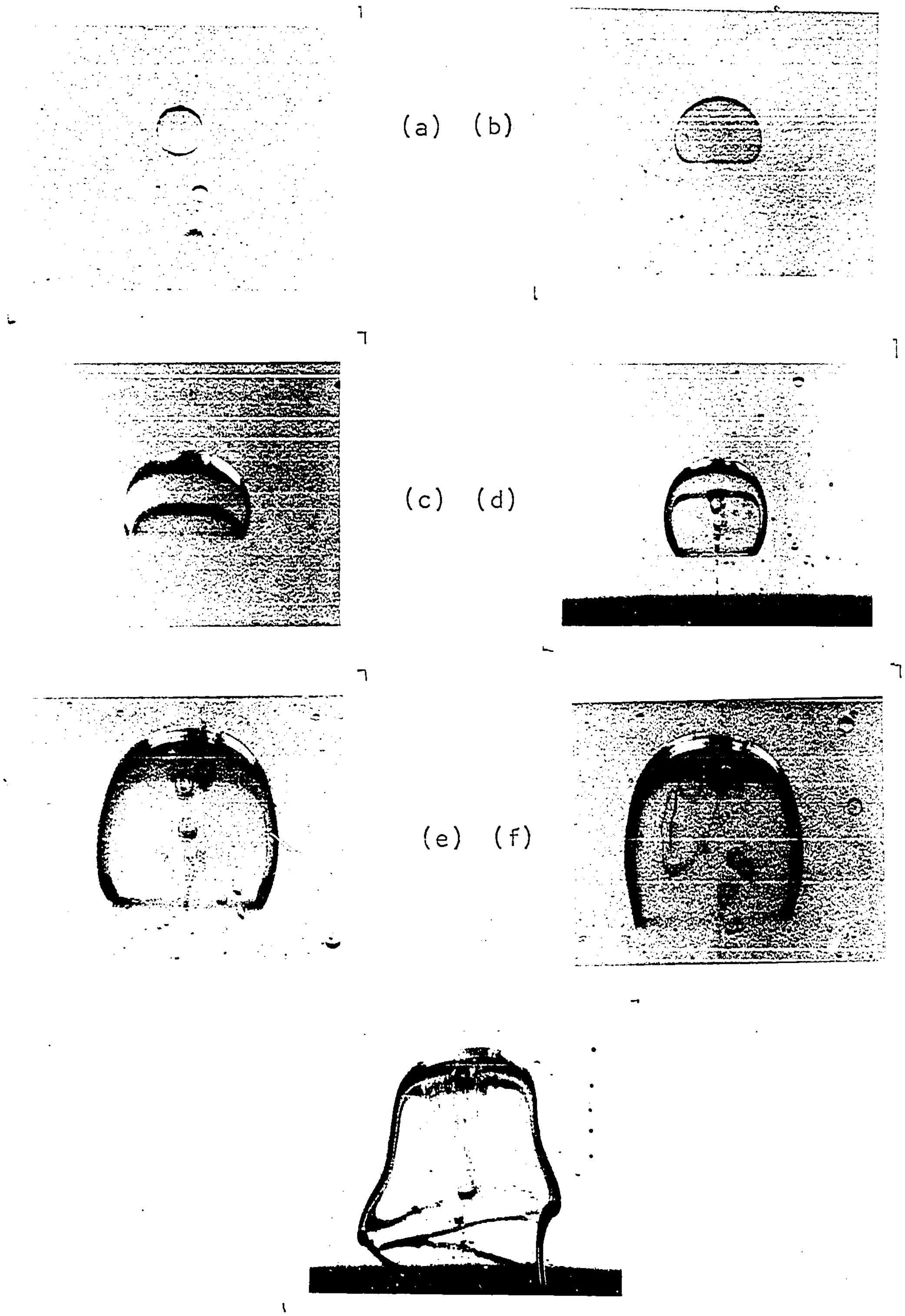

Fig. 6.2. Stages in drop shape development in viscous liquids.

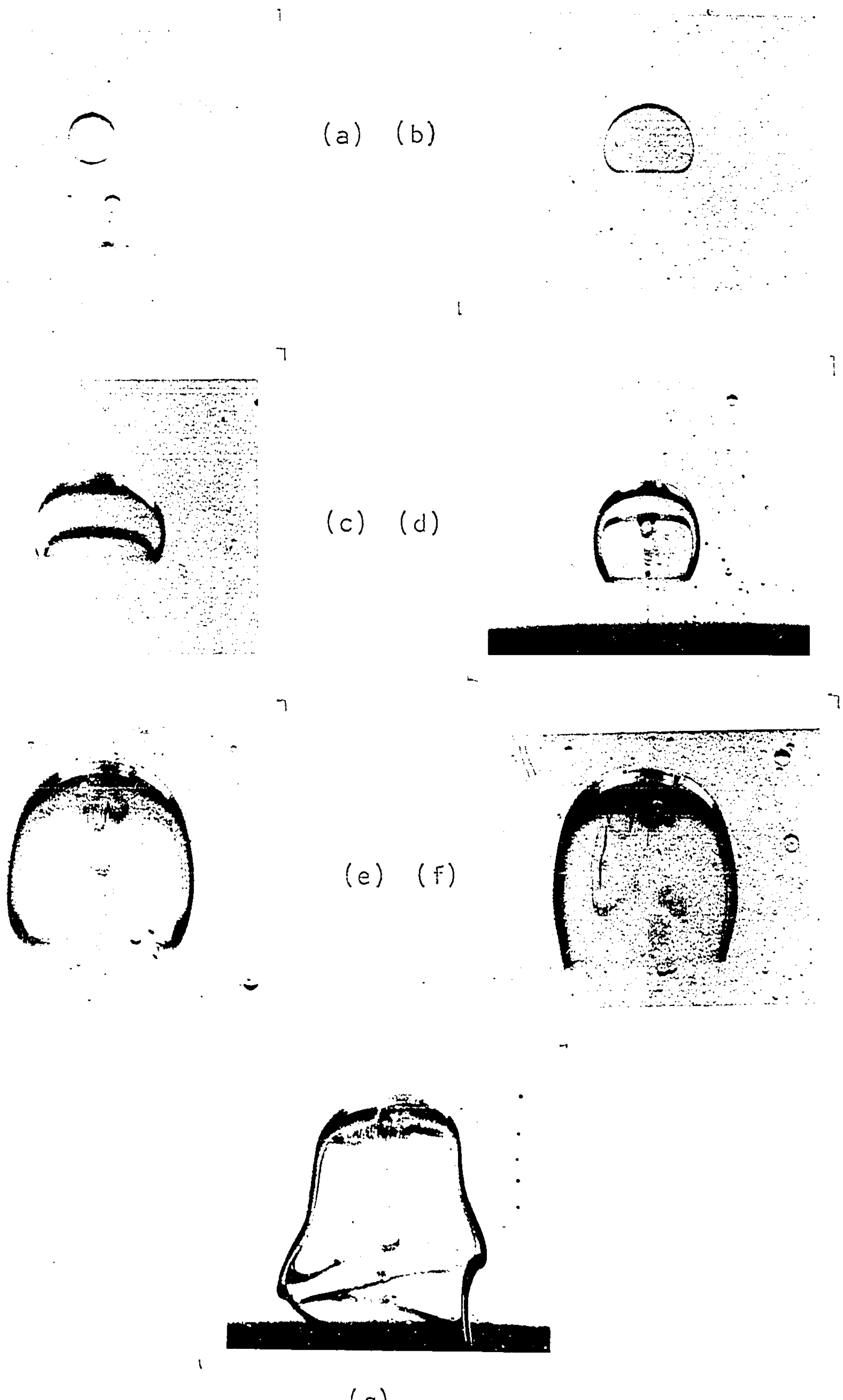

Fig. 6.2. Stages in drop shape development in viscous liquids.

Results have been plotted in Figure 6.3 for drops and bubbles ($K \ll 1$, $\gamma < 1$) to delineate the region where skirt formation occurs. The results are plotted as Sk vs Re. The open symbols correspond to drops or bubbles where no skirt formation was observed. The blocked-in symbols correspond to drops or bubbles with trailing skirts. Where a vertical line has been drawn through an open symbol, this denotes the critical condition corresponding to the onset of skirt formation. It will be recognized that the definition of this critical condition is rather arbitrary. Wegener et al. (1971) did not specify how they defined the critical condition for their bubble studies. In the present work, the onset was defined as shown in section 3.3.3 where Z in Figure 3.2 exceeds 0. For the Guthrie (1967) bubbles in a 6.1% PVA solution and for Shoemaker and Chazal (1969), photographs were reproduced and enough information was given to allow us to determine Sk and Re and whether or not there were skirts. Angelino (1966) also showed photographs of bubbles with skirts but did not give the dimensions of the bubbles. In the case of the Davenport et al. (1967) and Jones (1965) studies, conditions for the onset of skirt formation were quoted in the respective texts.

Figure 6.3 shows clearly that skirts do not form for drops having Reynolds numbers less than about 6 or skirt numbers (Sk) less than about 2. An approximate boundary separating the region of skirt formation from that of no skirt formation for drops is shown on the figure. The results for air bubbles are in qualitative agreement but the transition

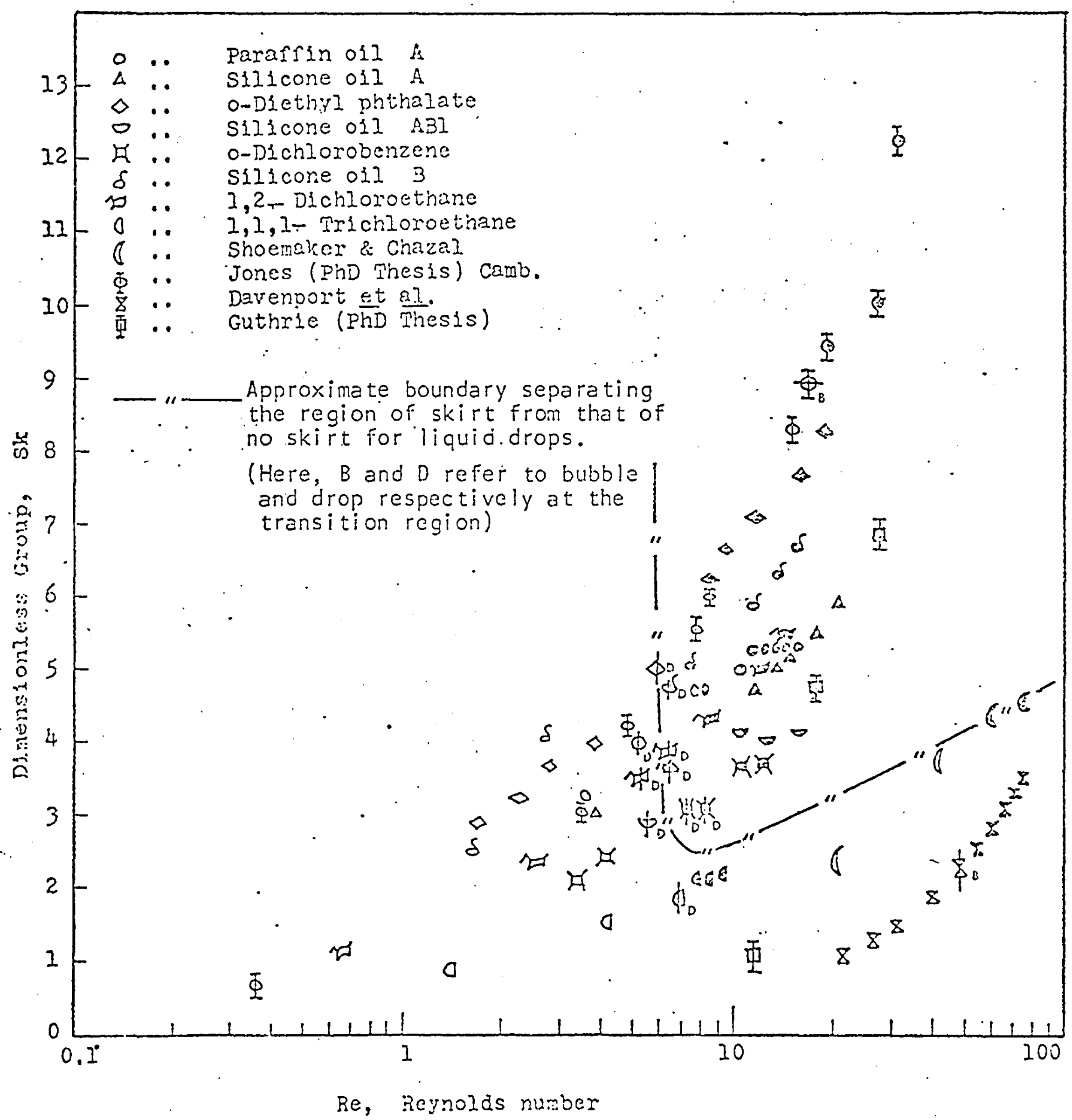

Fig. 6.3. Variation of dimensionless group, Sk, with Reynolds number, and the onset of skirt formation.

seems to take place for different values of Re and Sk. However, more data is certainly required to be able to make firm conclusions on this point. In addition, it is not clear from the data presented here how high the Re can be before skirts break down. Also, different size columns were used in the different experimental studies and, therefore, wall effects may account for some of the scatter in Figure 6.3.

As we have already seen, spherical drops have internal circulation if the accumulation of surface active contaminants at the interface is not excessive. For rigid spheres, a standing eddy develops at the rear for Re of the order of 20. For drops it is not clear when such a standing eddy should form, but it seems likely that the mobility of the interface will tend to delay the onset of a standing eddy, whereas the indentation at the base will tend to promote its formation. A qualitative sketch of the streamlines (relative to the drop) is shown in Figure 6.4 for an indented drop with a recirculating closed wake.

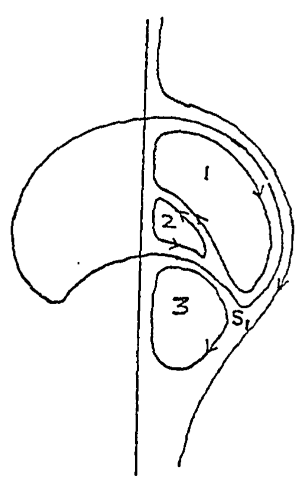

Fig.6.4. Streamlines for dimpled drop

Note that there must be three stable vortices (or at least an odd number). The second internal vortex (Vortex 2) is necessary in order to provide continuity of velocity everywhere. Such a second internal vortex has been observed by Pruppacher (1972) for water drops falling through air and has been predicted numerically by Hamielec and Johnson (1962).

The reason for the onset of skirts now becomes apparent. The viscous external liquid tends to pull the drop liquid at S_1 downward due to shear mainly from the external flow aided to some extent by Vortex 3. This tendency is resisted by interfacial tension forces trying to minimize the interfacial area and, to a much lesser extent for $K \ll 1$, by shear due to the internal circulation. The shearing force tending to extend the drop at S_1 would then be proportional to μU_0, while the resisting force is proportional to the interfacial tension, σ. Thus, we would expect skirt formation to depend on the dimensionless group $\mu U_0/\sigma$ (which we have given the symbol, Sk). In addition, we would expect Re to be important since at too low a Reynolds number, no standing eddy would be formed, while at too high a Reynolds number, the wake would be turbulent.

Once the onset of skirt formation has been achieved (Figure 6.2(d)), it appears likely that the flow pattern is modified so that for fully developed skirts, two vortices now appear in the external fluid and only one inside. This situation is sketched in Figure 6.5.

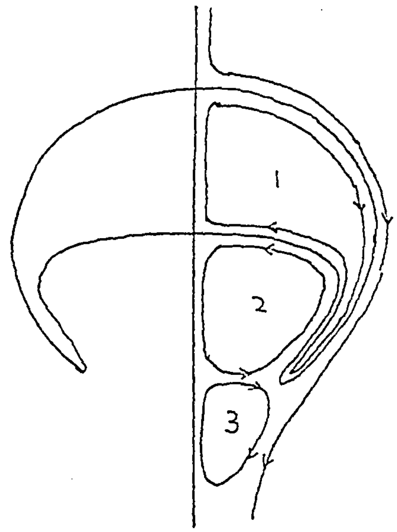

Fig.6.5. Streamlines for skirted drop

In the present work, 90% mesh aluminum particles were dispersed in silicone oil B before drop formation in a few cases to allow flow visualization. Observations confirmed that the motion inside the skirted drop was as shown in Figure 6.5 with the aluminum particles carried on the outside down to the bottom of the skirt and then upwards on the inside and finally back through the interior of the drop. It was also possible to distinguish a vortex with the direction of Vortex 2 protected by the skirt by observing tiny air bubbles trapped in the viscous sugar solution. It was not possible to confirm the existence of Vortex 3 by this means. No attempts have been made so far to photograph streaks due to tracer particles. Thus, the picture given above is plausible and consistent with observation, but further confirmation is required. One question that remains unanswered is how the transformation occurs from a situation where there are two vortices inside and one outside to the reverse situation where there are two outside and only one inside.

This qualitative picture of flow in the skirt helps to clarify the flow pattern postulated by Guthrie (1967, 1969) for bubble skirts. Guthrie proposed that the flow in the skirt could be either symmetric or asymmetrical (with respect to the centre line of the skirt). It would appear from the observations noted above that the actual flow pattern in the skirt is closer to the latter, but with non-zero velocity at the skirt/wake interface (relative to the skirt) since, at least for liquid drops, the enclosed wake is not stagnant as assumed by Guthrie.

With a further increase in drop size, the skirt straightens downwards and eventually becomes unstable as shown in Figure 6.2. These phenomena are no doubt complex and related to increased vorticity generation by the drop and to the stability of the thin trailing skirts. Further experimental and theoretical work is required in order to describe these later stages of skirt development.

6.3 Analytical Description of Flow in the Skirt

In order to arrive at analytical expressions for the prediction of skirt length, onset of wave formation, etc., it would be very useful to have an analytical description of the flow pattern. One such description that has been considered in some detail in this work follows from a solution of the creeping flow equations mentioned in passing by Batchelor, p.226.

This approach, though it leads to no directly useful results, is of some interest and is described briefly below.

A two-dimensional section through the skirt and enclosed vortex is considered as shown below. Point 0 is the tip of the skirt as shown in Figure 6.6. The skirt is considered to fill the entire wedge AOB in Figure 6.6, while the external liquid fills AOC. Motion below COB is not considered.

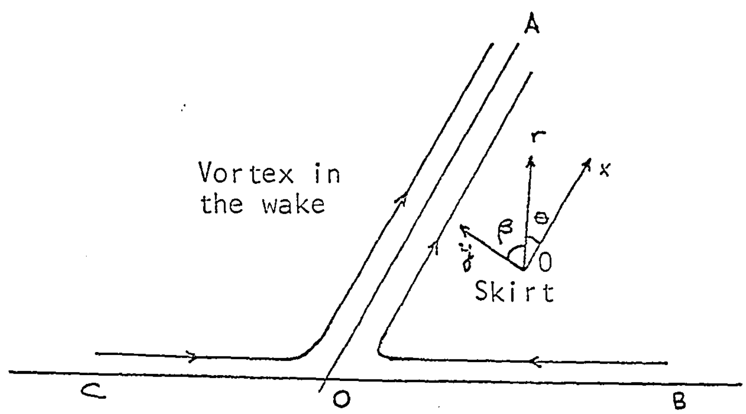

Fig.6.6. Sketch of the idealised skirt/eddy interface used in the model

Assumptions

i 0 is a stagnation point.

ii The tangential velocity at the interface, U_F, is finite; see Appendix F.

iii The skirt is very thin so that $\frac{\partial u_x}{\partial y} \gg \frac{\partial u_x}{\partial x}$.

iv The fluids are Newtonian.

v Both liquids are incompressible.

vi $U_z = 0$; i.e. the flow can be treated as two-dimensional.

vii Steady flow exists relative to the frame of reference.

viii Creeping flow is assumed in the skirt region.

Assume a solution of the form,

$$\psi = r^3 f(\theta) \tag{1}$$

A solution of this form is adopted because it gives flow patterns which resemble our physical situation at the wake/skirt interface. Now (1) must satisfy the equation of motion in creeping flow,

$$\nabla^4\psi = \nabla^2(\nabla^2\psi) = 0 \tag{2}$$

where the operator

$$\nabla^2 = \frac{\partial}{\partial r^2} + \frac{1}{r}\frac{\partial}{\partial r} + \frac{1}{r^2}\frac{\partial^2}{\partial \theta^2} \tag{3}$$

On substituting (1) and (3) into (2), and differentiating, we obtain

$$\nabla^4\psi = \frac{1}{r}(f^{iv} + 10f^{ii} + 9f) = 0$$

$$\text{i.e.} \quad f^{iv} + 10f^{ii} + 9f = 0 \tag{4}$$

The roots are then;

$$m = \pm j, \pm 3j$$

So that the solution becomes

$$f = a_0 \sin\theta + b_0 \cos\theta + c_0 \sin 3\theta + d_0 \cos 3\theta \qquad .....(5)$$

Boundary Conditions

(i) $f(0) = 0$ (6)

since the line $\theta = 0$ is a streamline.

(ii) At $r = Z$, $v_r = U_F$. But $v_r = \frac{1}{r}\frac{\partial\psi}{\partial\theta} = 3r^2 f'(\theta)$,

therefore, $f'(0) = \dfrac{U_F}{3Z^2}$ (7)

where $U_F = \frac{y}{Z}\left(\frac{\Delta\rho g}{\rho}\frac{V}{A}\sin\beta\right)^{\frac{1}{2}}$

where this expression is derived from an empirical result for thin liquid sheets in steady flow, Dombrowski and Fraser (1954). See Appendix F.

(iii) $f'(-\beta) = 0.$ (8)

This forces the normal velocity to vanish at $\theta = -\beta$.

(iv) $f''(-\beta) = 0.$ (9)

It is assumed that there is no transfer of momentum at the line $\theta = -\beta$.

After lengthy algebraic manipulation, the values of a_o, b_o, c_o and d_o can be calculated. For the special case of = $\pi/3$ (within the observed values), we get the simple solution,

$$\psi = \frac{U_F r^3}{9Z^2} \sin 3\theta \qquad (10)$$

The above solution contains some of the principle features of the actual flow situation. At the same time, however, we have had to adopt several assumptions which are not strictly valid.(e.g. boundary condition (iv), the empirical expression for U_F and the wedge shape approximation shown in Figure 6.6). This model provides a first approach to the description of the flow patterns, but further work is necessary before a completely satisfying model can be achieved.

6.4 Skirt Length: Experimental Measurements

For the drops where skirt formation occurred, skirt lengths (Z) were determined as shown in Figure 3.2. These results are in Tables D1 to D8. While various methods of plotting the data were tried in an effort to determine the dependence of Z on Re and Sk (or We = ReSk), there was very wide scatter. This was often because the skirts themselves were unsteady and asymmetric, especially for the systems with a large density difference, $\Delta\rho$. Thus, additional work is required to define the onset of skirt instability before meaningful plots of skirt length can be presented for those systems where steady skirts are formed.

TABLE D1. Experimental Results on Skirts For Rising Drops

Paraffin Oil - 26.5°C

No.	Dimension-less Skirt Length z/d	Skirt Length z,cm	Reynolds Number Re	Weber Number We	Skirt Number Sk	Presence of Skirt
1	——	——	3.54	11.29	3.23	0
2	0.06	0.18	5.01	21.69	4.00	x
3	0.51	1.90	7.65	35.88	4.76	+
4	0.57	2.20	8.06	31.22	4.76	+
5	0.87	3.90	10.06	51.09	5.00	+
6	1.04	4.80	10.46	54.37	5.26	+
7	1.05	5.30	11.75	62.36	5.26	+
8	1.71	8.80	11.94	63.34	5.26	+
9	0.58	3.00	12.03	63.84	5.26	+
10	1.26	6.60	12.12	64.33	5.26	+
11	1.73	9.80	13.15	79.75	5.26	+
12	——	——	15.23	85.33	5.26	+
13	0.7	4.30	14.45	77.93	5.26	+

0 = no skirt

x = onset of skirt

+ = presence of skirt

TABLE D2. Experimental Results on Skirts for Rising Drops

o-Diethyl Phthalate - 27.8°C

No.	Dimensionless Skirt Length z/d	Skirt Length z,cm	Reynolds Number Re	Weber Number We	Skirt Number Sk	Presence of Skirt
1	——	——	1.71	4.84	2.86	0
2	——	——	2.25	7.34	3.23	0
3	——	——	2.80	10.31	3.70	0
4	——	——	3.80	15.00	4.00	0
5	0.15	0.50	5.66	29.06	5.00	x
6	0.51	2.10	8.22	51.07	6.25	+
7	0.63	2.70	8.50	52.08	6.25	+
8	0.88	3.80	9.31	61.83	6.67	+
9	0.66	2.90	8.83	54.82	6.25	+
10	0.90	4.10	9.52	61.52	6.25	+
11	1.52	7.40	11.30	80.65	7.14	+
12	1.35	7.20	12.56	91.00	7.14	+
13	1.22	7.70	15.04	115.98	7.69	+
14	0.83	5.60	17.41	131.75	7.69	+
15	1.35	9.20	18.49	155.10	8.33	+

0 = no skirt

x = onset of skirt

\+ = presence of skirt

TABLE D3. Experimental Results on Skirts for Rising Drops

Silicone Oil A - 27.5°C

No.	Dimensionless Skirt Length z/d	Skirt Length z,cm	Reynolds Number Re	Weber Number We	Skirt Number Sk	Presence of Skirt
1	——	——	3.87	11.69	3.03	0
2	——	——	6.37	23.92	3.70	x
3	1.13	4.90	11.35	54.14	4.76	+
4	1.21	5.30	11.68	56.60	4.76	+
5	1.50	7.10	13.12	65.95	5.00	+
6	1.48	7.10	13.78	71.98	5.26	+
7	1.69	8.50	14.80	79.24	5.26	+
8	1.41	8.00	17.79	101.29	5.56	+
9	1.56	9.30	17.68	106.48	5.56	+
10	1.69	11.00	20.78	120.70	5.88	+

0 = no skirt

x = onset of skirt

\+ = presence of skirt

TABLE D4. Experimental Results on Skirts for Rising Drops

Silicone Oil AB1 - 27.8°C

No.	Dimension-less Skirt Length z/d	Skirt Length z, cm	Reynolds Number Re	Weber Number We	Skirt Number Sk	Presence of Skirt
1	——		5.43	15.60	2.86	x
2	1.07	4.4	10 56	44.37	4.17	+
3	0.74	3.20	10.05	38.19	3.85	+
4	0.78	3.40	10.33	37.78	3.85	+
5	1.17	5.40	12.04	68.87	4.00	+
6	——	——	13.04	57.50	4.35	——
7	1.31	7.80	13.75	57.81	4.17	+
8	1.11	6.80	15.47	64.05	4.17	+
9	——		16.94	75.02	4.35	——

0 = no skirt

x = onset of skirt

\+ = presence of skirt

TABLE D5. Experimental Results on Skirts for Rising Drops

o-Dichlorobenzene - 27.8°C

No.	Dimension-Less Skirt Length z/d	Skirt Length z, cm	Reynolds Number Re	Weber Number We	Skirt Number Sk	Presence of Skirt
1	——	——	1.54	2.24	0.08	0
2	——	——	3.33	7.31	2.17	0
3	——	——	4.14	10.03	2.44	0
4	——	——	4.50	11.40	2.50	0
5	——	——	6.05	17.52	2.86	0
6	——	——	6.79	21.45	3.23	x
7	——	——	7.08	22.19	3.13	——
8	——	——	7.05	21.41	3.13	——
9	0.02	0.10	8.48	28.70	3.03	x
10	——	——	8.75	29.88	3.45	x
11	0.05	0.30	8.78	29.88	3.45	+
12	——	——	9.98	34.95	3.57	——
13	0.38	2.60	10.50	37.34	3.70	+
14	0.10	0.70	10.24	37.30	3.57	+
15	0.34	2.40	11.03	42.20	3.85	+

0 = no skirt

x = onset of skirt

+ = presence of skirt

TABLE D6. Experimental Results on Skirts for Rising Drops

1,2-Dichloroethane - 27.5°C

No.	Dimension-Less Skirt Length z/d	Skirt Length z, cm	Reynolds Number Re	Weber Number We	Skirt Number Sk	Presence of Skirt
1	——	——	0.68	0.87	1.14	0
2	——	——	1.45	3.07	2.00	0
3	——	——	2.58	6.09	2.38	0
4	——	——	3.17	8.83	2.78	——
5	——	——	3.57	10.32	2.86	——
6	——	——	4.69	15.44	3.03	——
7	——	——	5.13	17.85	3.45	x
8	——	——	5.64	20.11	3.57	x
9	——	——	6.46	24.96	3.85	x
10	0.27	1.50	8.64	37.57	4.35	+
11	0.29	1.70	9.29	41.20	4.35	+
12	0.67	4.30	11.29	55.97	5.00	+
13	0.51	3.40	11.83	57.32	5.00	+
14	0.84	6.00	13.39	70.56	5.26	+

0 = no skirt

x = onset of skirt

+ = presence of skirt

TABLE D7. Experimental Results on Skirts for Rising Drops

Silicone Oil B - 25.4°C

No.	Dimension-Less Skirt Length z/d	Skirt Length z,cm	Reynolds Number Re	Weber Number We	Skirt Number Sk	Presence of Skirt
1	——	——	1.63	4.06	2.50	0
2	——	——	1.88	4.73	2.50	0
3	——	——	2.79	8.78	3.13	0
4	——	——	4.09	16.15	4.00	0
5	——	——	4.43	17.88	4.00	0
6	——	——	4.65	18.77	4.00	0
7	0.11	0.40	6.50	31.74	4.76	x
8	0.25	1.00	7.18	36.69	5.00	+
9	0.42	1.80	8.02	42.79	5.26	+
10	——	——	8.33	44.68	5.26	——
11	——	——	9.77	55.83	5.56	——
12	1.53	8.30	11.25	66.79	5.88	+
13	1.24	7.10	12.40	76.61	6.25	+
14	1.65	10.20	13.87	88.90	6.25	+
15	0.99	6.70	15.48	101.33	6.67	+

0 = no skirt

x = onset of skirt

+ = presence of skirt

TABLE D8. Experimental Results on Skirts for Rising Drops

1,1,1-Trichloroethane - 27.5°C

No.	Dimension-Less Skirt Length z/d	Skirt Length z, cm	Reynolds Number Re	Weber Number We	Skirt Number Sk	Presence of Skirt
1	——	——	1.05	0.75	0.72	0
2	——	——	1.45	1.19	0.82	0
3	——	——	3.03	4.04	1.33	0
4	——	——	2.49	2.34	0.94	0
5	——	——	4.46	6.94	1.56	0
6	——	——	5.52	9.52	1.75	0
7	0.08	0.50	7.13	14.08	1.96	x
8	——	——	7.16	14.04	1.96	——
9	0.34	2.10	7.44	14.95	2.00	+
10	0.35	2.20	7.89	16.36	2.08	+
11	0.34	2.20	8.11	16.83	2.08	+
12	0.26	1.70	8.52	18.29	2.13	+
13	0.34	2.40	9.40	20.87	2.22	+

0 = no skirt

x = onset of skirt

+ = presence of skirt

CHAPTER 7

CONCLUSIONS AND SUGGESTIONS FOR FUTURE RESEARCH

7.0 Terminal Velocity

The results obtained using three different approaches, Section 5.0, have been compared with experimental results in Figures 5.4.3 and 5.4.4. The results of the semi-empirical analysis have not been included since this approach proved to be fruitless. In contrast, the creeping flow analyses, methods (i) and (ii), produced results which show too steep a slope in the variation of the calculated velocities with the measured ones. For high measured velocities these analyses greatly overestimate the calculated velocities. For small measured velocities, the calculated velocities differ only slightly. This leads us to the following conclusions: analyses (i) and (ii) may be used to predict the terminal velocities for drops smaller than about 2 cm. sphere equivalent diameter. However, for larger drops, these analyses cease to conform. This result is expected in that it is physically inconsistent to disregard the inertial terms for a drop where Re $>$ 1 and yet hope to deal with deformed drops.

On the contrary, the results obtained by the potential flow analysis (method iv), seem to give results which agree well with the experimental results, except for the small drops. This is shown in Figure 5.4.4. For smaller drops,

$d<4$ cm, this theory slightly overestimates the true terminal velocity of a drop. Three possible reasons why this approach fails for drops with $d<4$cm are evident. Firstly, this analysis assumes an oblate spheroid which is not strictly true for smaller drops. Secondly, in smaller drops, the Reynolds number is too small for potential flow to be valid. Lastly, while the experimental technique, using cine photographs, made it possible to determine a, b, and U_0, the technique was not accurate enough for small drops and the eccentricity, $e = f(a,b)$, might contain considerable error.

However, agreement between our theoretically determined velocities and the measured values is so good that we can conclude that the potential flow technique using ellipsoidal coordinates predicts the terminal velocity of dimpled drops very accurately over the range of variables investigated.

7.1 Shape of Dimpled Drops

As stated in Section 4.2.0, we are unable to determine drop shape analytically or empirically.

However, other areas have produced interesting information. For example, a graph of C_D versus R_e, (Fig.4.4), indicates that the drag force acting on the surface of the drop is a very strong function of the shape of the drop. Observations revealed that the drop first develops a skirt. Waves then set in and, finally, the whole drop becomes unstable. Correspondingly, C_D first decreases, reaches a minimum, and then continues to increase. Further work is necessary to explain these phenomena more fully.

Another interesting case is the variation of Eö with Re, Figure 4.6. Here, efforts to correlate these groups along with the physical property groups M_1, M_2, and P failed to provide valuable information.

7.2 Skirts

For all the systems employed in this work, "skirts" were observed for drops beyond a certain size. The onset of skirt formation is a function of Re and of the skirt number $Sk = \mu U_0/\sigma$, and a graphical correlation, Figure 6.4, delineates the region where skirt formation occurs. A qualitative argument is presented to explain the onset and development of skirts and this argument is consistent with flow visualization experiments. For systems with a large density difference, $\Delta\rho$, skirts tended to be growing with time, to be asymmetric and to have waves travelling down them. Some photographs and sketches of these unsteady skirts are included.

7.3 Suggestions for Future Research

The present study is only a first step towards the more significant objective of a full understanding of the behaviour of dimpled drops. More work is certainly required in this field. The striking questions raised during our work, and the light that could potentially be shed on the dynamics of drop coalescence, break-up, and the mechanics of skirts, by further studies of this sort, make a continuation of the research most desirable. In this connection, attention is called to;

1. Comprehensive study of the internal circulation, the vortices in the wake, and the dimple formation in liquid drops.
2. Detailed analysis of the shape of large liquid drops for a wide range of values of $K = \mu'/\mu$; Development of either an empirical or analytical correlation which will enable one to predict the shape of a dimpled drop from the liquid physical properties.
3. The development of waves and the instability observed in skirts for large liquid drops rising through viscous media.
4. The interaction, coalescence, and break-up of large liquid drops moving through viscous media.

NOTATION

a	cm	semi-major axis.
a_o, b_o, c_o, d_o		constant coefficients used in Section 6.4.
A	cm^2	projected area in a horizontal plane at the waist of the drop.
A_n, B_n, C_n, D_n		constants in spherical coordinate solution.
Ai	cm^2	area of segment i of the drop (see Appendix D).
As	cm^2	total surface area of the drop.
b	cm	semi-minor axis
$\hat{B}$	cm	height of drop (see Fig.5.3 in Section 5.4).
c	cm	focal length of an ellipse.
$c_j \ldots, c_j' \ldots$		constant coefficients used in Section 5.2.3 (j=1,...4).
$C_n^{-\frac{1}{2}}$		Gegenbauer polynomical, order n, degree $-\frac{1}{2}$.
d	cm	sphere equivalent diameter.
e		eccentricity, $(1-(b/a)^2)^{\frac{1}{2}}$.
$E\ddot{o}$		Eötvos number, $\Delta\rho g d^2/\sigma$
f, f', f''		coefficients as defined in Section 5.1.3.
F, F', F''		coefficients as defined in Section 5.1.3.
h	cm	half width of skirt.
J		$(f'(z)\overline{f}'(\overline{z}))^{\frac{1}{2}}$ ⟨Milne-Thompson, p.473⟩.

K_o, K_1, K_2, K_3		parameters defined in Sections 5.1.3 and 5.5.2.
K_3^a, K_3^b		coefficients relating U_o to a and b in Section 5.5.2.
L	cm	characteristic length dimension
m		arbitrary constant
M		positive constant, $0 \leq M \leq 2$.
n		integer number in Section 6.5.
$P, P_\sigma, P_{hs}, P_{hd}, P_c$	$\frac{gm}{cm\ sec^2}$	pressure; outside drop, increment due to interfacial tension, hydrostatic, hydrodynamic, and due to internal circulation, respectively.
q_o	cm/sec	local velocity of the external liquid at the surface of the drop.
R	cm	sphere equivalent radius.
R_1, R_2, R_0	cm	two principal radii of curvature, and the radius of curvature at the stagnation point of a drop.
Re		Reynolds number, dU_o/ν.
S_1, S_2		symbols denoting rounded and concave surface of the drop in Section 5.0.
t		defined in Section 5.1.3.
u_x, u_y, u_z	cm/sec	velocity components in the x,y, and z directions.
U_o	cm/sec	terminal velocity of drop.
V_d	cm^3	total volume of drop.
We		Weber number, $\rho d U_o^2/\sigma$.
Sk		skirt number, $\mu U_o/\sigma$.
z		complex variable, $x + iy$.
Z	cm	length of skirt.

Greek Letters

ρ', ρ	gm/cc	density of dispersed and continuous phases.
$\Delta\rho$	gm/sec	density difference, $\lvert\rho-\rho'\rvert$.
μ', μ	dm/cm, sec	viscosity of dispersed and continuous phases.
σ	dynes/cm	interfacial tension.
$\mathcal{K}$		viscosity ratio, μ'/μ.
γ		density ratio, ρ'/ρ.
η, ξ		elliptical coordinate, η away from vertical.
$\psi_s, \psi_e, \psi_\phi$		functions of shape as defined in Sections 5.4.1, 5.4.2 and 5.4.3.
ψ		stream function.
λ		function defined in Section 5.2.3.
χ_1, χ_2, χ_3		functions defined in Section 5.2.3.
Δ_s, Δ_{TA}		functions derived by Sarto and Taylor and Acrivos given in Section 6.3.2.
$\tilde{\omega}$		cylindrical coordinate.

REFERENCES

Adam, N.K., 1949, The Physics and Chemistry of Surfaces, Lond. Oxf. Press.

Angelino, H., 1966, Hydrodynamique des grosses bulles dans les liquides visqueux, Chem. Eng. Sci. 21, p.541.

Batchelor, G.K., 1967, An Introduction to Fluid Dynamics, Camb. Univ. Press.

Bond, W.N., 1927, Bubbles, Drops and Stoke's Law, Phil. Mag. 4, p.889.

Boussinesq, J., 1913, Compt. Rend. Acad. Sci. 156, p.1124.

Chia-Shon Yih, 1965, Dynamics of nonhomogeneous fluids, Macmillan Series, NY.

Clift, R. and Grace, J.R., 1970, Chem. Eng. Prog. Symp. Series 66, No.105.

Collins, R., 1966, A second approximation for the velocity of a large gas bubble rising in infinite liquid, J. Fluid. Mech. 25, p.469.

Crabtree, J.R. and Bridgwater, J., 1967, The wakes behind 2-dim. air bubbles, Chem. Eng. Sci. 22, p.1517.

Davenport, W.G. et al., 1967, Behaviour of spherical-cap bubbles in liquid metals, J. Iron and Steel Inst. 25, p.1034.

Davies, R.M. and Taylor, G.I., 1950, The Mechanics of Large Bubbles Rising Through Extended Liquids and Through Liquids in Tubes, Proc. Roy. Soc. A200, p.375.

Dombrowski, N., 1954, Philos. Trans. Roy. Soc., A247, p.101.

Fararoui, A. and Kintner, R.C., 1961, Flow and shape of drops in non-Newtonian fluids, Trans. Soc. Rheol. 5, p.369.

Garner et al., 1957, Distortion of fluid drops in the Stokesian region, Nature, 180, p.331.

Garner, F.H. and Haycock, P.J., 1959, Circulation in Liquid Drops, Proc. Roy. Soc. A252, p.457.

Goldstein, S., 1957, Modern Developments in Fluid Dynamics, Oxf. Univ. Press.

Grace, J.R., 1972, Shapes and velocities of bubbles rising in infinite liquids (to be published).

Grace, J.R. and Harrison, D., 1967, The influence of bubble shape on the rising velocities of large bubbles, Chem. Eng. Sci. 22, p.1337.

Guthrie, R.I.L., 1967, Dynamic and mass transfer phenomena of spherical-capped bubbles, Ph.D. Thesis (Lond.).

Guthrie, R.I.L. and Bradshaw, A.V., 1969, The stability of gas envelopes trailed behind spherical-cap bubbles rising through viscous liquids, Chem. Eng. Sci., p.913.

Hadamard, J., 1911, Comp. Rend. Acad. Sci. 152, p.1735.

Harper, J.F. et al., 1967, The effect of surface tension with temp. of motion of bubbles and drops, J. Fluid Mech. 27, p.361.

Hill, M.J.M., 1894, Phil. Trans. Roy. Soc. A185, p.213.

Hughes, R.R. and Gilliland, E.R., 1954, The Mechanics of Drops, Chem. Eng. Prog. 48, p.497.

LeClair, B.P. and Hamielec, A.E., 1970, Flow behavior around a sphere accelerating in a viscous fluid, Fluid Dynamics Symposium, McMaster Univ. (1970, Aug.).

Levich, V.G., 1962, Physiochemical Hydrodynamics, Prentice-Hall.

Jones, D.R.M., 1965, Liquid analogies for fluidized beds, Ph.D. Thesis, Camb..

McCracken, D.D. and Williams, S.D., 1964, Numerical methods and Fortran programming, John Wiley.

Magarvery, R.H. and Maclatchy, C.S., 1968, AIChE J. 14, p.260.

Merrington, A.C. and Richardson, E.G., 1947, The break-up of liquid jets, Proc. Phys. Soc. (Lond.) 59, p.1.

Milne-Thomson, L.M., 1969, Theoretical Hydrodynamics, Macmillan Series, NY.

Oberbeck, H.A., 1876, J. Reine Angew. Math. 81, p.62.

Payne, L.E. and Pell, W.H., 1960, The Stokes flow problem for a class of anxially symmetric bodies, J. Fluid Mech. 7, p.529.

Pruppacher, H.R. and Pitter, R.L., 1971, A semi-empirical determination of the shape of cloud and raindrops, J. Atmos. Sci. 28, p.86.

Pruppacher, H.R. and Beard, K.V., 1970, Q.J. Roy. Meteor. Soc. 96, p.247.

Rybszinski, W., 1911, Bull. Acad. Sci. de Cracovie A, p.40.

Saito, S., 1913, Sci. Rep. Tohoku Imp. Univ., Sendai, Japan 2, p.179.

Savic, P., 1953, Circulation and distortion by liquid drops falling through a viscous media, Nat. Res. Council Canada, Rept. NRC-MT-22.

Shoemaker, P.D. and Chazal, L.E., 1969, Dimpled and skirted liquid drops moving through viscous media, Chem. Eng. Sci. 24, p.779.

Stokes, G.G., 1850, Trans. Camb. Phil. Soc. 9, p.8.

Tamotika, S., 1937, Aero. Res. Comn. Rept. and Memo., No. 1678, p.86.

Taylor, T.D. and Acrivos, A., 1964, On the deformation and drag of a falling viscous drop at low Reynolds number, J. Fluid. Mech. 18, p.466.

APPENDIX A. Calculation of Stream Function for Method (1)

From equations in Section 5.1, we have

$$E^4\psi = \frac{(\lambda^2+1)(1-t^2)}{c^4(\lambda^2+t^2)}\left\{4(F-\lambda F') + (\lambda^2+t^2)F''\right\} \qquad (i)$$

where $\quad F = (\lambda^2+1)f'' - 2f \qquad$ (ii)

and $\quad f = \dfrac{\psi}{1-t^2} \qquad$ (iii)

is a function only of λ.

In order for this equation to be satisfied for all t and λ, the second term in the bracket in Equation (i) must vanish,

i.e. $\quad 4(F-\lambda F') + (\lambda^2+t^2)F'' = 0 \qquad$ (iv)

We choose our solution such that F is a function of λ only. Thus, (iv) can occur only if the following relations are simultaneously satisfied;

$$F'' = 0 \qquad (v)$$

$$F-\lambda F' = 0 \qquad (vi)$$

From (v), $F = c_1\lambda + c_0$ where c_0 is an arbitrary constant which we can set equal to zero. Substitution of this expression into (ii) gives

$$(\lambda^2+1)f'' - 2f = c_1\lambda \qquad \text{(vii)}$$

The particular integral of solution of this equation is,

$$f = -\tfrac{1}{2}c_1\lambda \qquad \text{(viii)}$$

The remaining part of the solution of equation (vii), corresponds to the solution of the homogeneous equation,

$$(\lambda^2+1)f'' - 2f = 0 \qquad \text{(ix)}$$

This equation can be written as,

$$\frac{d}{d\lambda}\left\{(\lambda^2+1)f' - 2\lambda f\right\} = 0$$

which on integrating gives

$$(\lambda^2+1)f' - 2\lambda f = c_2 \qquad \text{(x)}$$

Again, Equation (x) can be written in the form,

$$\frac{d}{d\lambda}\left(\frac{f}{1+\lambda^2}\right) = \frac{c_2}{(1+\lambda^2)^2} \qquad \text{(xi)}$$

Integration of (xi) gives

$$f = c_2(\lambda^2+1)\int_0^\lambda \frac{d\lambda}{(1+\lambda^2)^2} + c_3(\lambda^2+1) \qquad \text{(xii)}$$

Integrating $\int_0^{\lambda} \frac{d\lambda}{(1+\lambda^2)^2}$ by parts we obtain

$$\int_0^{\lambda} \frac{d\lambda}{(1+\lambda^2)^2} = \tfrac{1}{2}(\frac{\lambda}{1+\lambda^2}) - \cot^{-1}\lambda)$$

and the solution of the homogeneous equation becomes

$$f = \tfrac{1}{2}\, c_2\{\lambda - (\lambda^2+1)\cot^{-1}\lambda\} - c_3(\lambda^2+1) \qquad \text{(xiii)}$$

Hence, the general equation becomes,

$$f = -\tfrac{1}{2}\, c_1\lambda + \tfrac{1}{2}\, c_2\left\{\lambda - (1+\lambda^2)\cot^{-1}\lambda\right\} - c_3(\lambda^2+1)$$

$$\text{.....(xiv)}$$

which gives the stream functions ψ and ψ' used in Section 5.1.3.

APPENDIX B. Evaluation of Limits

$$\lim_{e\to 0} K_1 = \lim_{e\to 0} \frac{1}{e}\sqrt{1-e^2} - \frac{1-2e^2}{e^2}\sin^{-1}e$$

$$= \lim_{e\to 0} \frac{\frac{1}{e}\left(1-\frac{e^2}{2} - \frac{e^4}{8} \; \ldots.\right) - \frac{1}{e^2}(1-2e^2)\left(e+\frac{e^3}{6} + \frac{3e^5}{40} + \ldots.\right)}{e}$$

$$= \lim_{e\to 0} \frac{\cancel{\frac{1}{e}} - \frac{e}{2} - \frac{e^3}{8} - \cancel{\frac{1}{e}} - \frac{e}{6} - \frac{3e^3}{40} + 2e + \frac{e^3}{3} + \frac{3e^5}{20}}{e}$$

$$= \lim_{e\to 0} \cancel{\frac{1}{e^2}} - \frac{1}{2} - \frac{e^2}{8} - \cancel{\frac{1}{e^2}} - \frac{1}{6} - \frac{3e^2}{40} + 2 + \frac{e^2}{3} + \frac{3e^4}{20}$$

$$= \frac{4}{3}$$

APPENDIX C. Evaluation of Stream Function for Method (ii)

From Equation (15) of Section 5.2 we set,

$$v_r = \chi_1(r)\cos\theta \qquad \text{(ia)}$$

$$v_\theta = \chi_2(r)\sin\theta \qquad \text{(ib)}$$

$$P-\pi = \mu\chi_3(r)\cos\theta \qquad \text{(ic)}$$

$$v_r' = \chi'_1(r)\cos\theta \qquad \text{(id)}$$

$$v_\theta' = \chi'_2(r)\sin\theta \qquad \text{(ie)}$$

$$p' = \mu'\chi_3'(r)\cos\theta \qquad \text{(if)}$$

Substituting these expressions into Equations (12)-(14) of Section 5.2 we obtain;

$$\frac{d^2\chi_1}{dr^2} + \frac{2}{r}\frac{d\chi_1}{dr} - \frac{4(\chi_1+\chi_2)}{r^2} = \frac{d\chi_3}{dr} \qquad \text{(ii)}$$

$$\frac{d^2\chi_2}{dr^2} + \frac{2}{r}\frac{d\chi_2}{dr} - \frac{2(\chi_1+\chi_2)}{r^2} = -\frac{\chi_3}{r} \qquad \text{(iii)}$$

$$\frac{d\chi_1}{dr} + \frac{2}{r}(\chi_1+\chi_2) = 0 \qquad \text{(iv)}$$

The equations for the inner fluid take a similar form. From (iv),

$$\chi_2 = -\frac{r}{2}\frac{d\chi_1}{dr} - \chi_1 \qquad \text{(v)}$$

Substituting for these in (iii), we get

$$\frac{\chi_3}{r} = \frac{d^2}{dr^2}\left(\frac{r}{2}\frac{d\chi_1}{dr} + \chi_1\right) + \frac{2}{r}\frac{d}{dr}\left(\frac{r}{2}\frac{d\chi_1}{dr} + \chi_1\right) - \frac{1}{r}\frac{d\chi_1}{dr} \qquad \text{.....(vi)}$$

i.e.

$$\chi_3 = \frac{1}{2} r^2 \frac{d^3\chi_1}{dr^3} + 3r \frac{d^2\chi_1}{dr^2} + 2\frac{d\chi_1}{dr} \qquad \text{(vii)}$$

Now substituting for χ_3 in (ii), we obtain

$$r^3 \frac{d^4\chi_1}{dr^4} + 8r^2 \frac{d^3\chi_1}{dr^3} + 8r \frac{d^2\chi_1}{dr^2} - 8\frac{d\chi_1}{dr} = 0 \qquad \text{(viii)}$$

This is the well-known Euler Equation. We choose a solution of the form,

$$\chi_1 = r^n \qquad \text{(ix)}$$

Then

$$n(n-1)(n-2)(n-3) + 8n(n-1)(n-2) + 8n(n-1) - 8n = 0 \qquad \text{.....(x)}$$

which, on simplifying, gives

$$n(n-2)(n+1)(n+3) = 0 \qquad \text{(xi)}$$

so that the roots are

$$n_1 = 0, n_2 = 2, n_3 = -1, \text{ and } n_4 = -3$$

Therefore, for X_1, X_3 and X_2, we have the following expressions;

$$X_1 = \frac{c_1}{r^3} + \frac{c_2}{r} + c_3 + c_4 r^2 \qquad \text{(xii)}$$

$$X_2 = \frac{c_1}{2r^3} - \frac{c_2}{2r} - c_3 - 2c_4 r^2 \qquad \text{(xiii)}$$

$$X_3 = \frac{c_2}{r^2} + 10c_4 r \qquad \text{(xiv)}$$

On substituting these back into equations for v_r, v_θ, P, v_r', v_θ', and P', we obtain the general solutions for Equations (9), (10) and (11) as given in Section 5.2.3.

APPENDIX D. Derivation of the Equations for Determining the Surface Area and Volume of Drop

The evaluation of surface area and volume of an axisymmetric drop given points on the boundary as r_i, z_i.

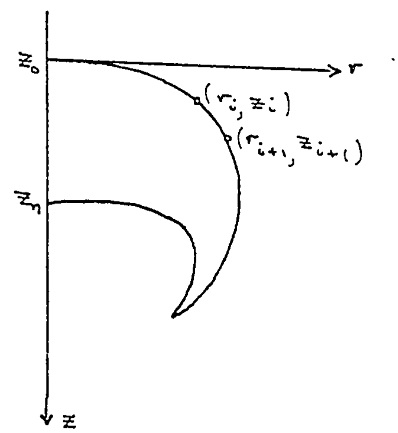

Referring to the above figure,

$$A_i = \int_{s_i}^{s_{i+1}} 2\pi r\, ds_i$$

But $ds^2 = dz^2 + dr^2$, $\therefore$ $ds = \left\{1 + \left(\frac{dr}{dz}\right)^2\right\}^{\frac{1}{2}}$

and $$A_s = 2\pi \int_{z_0}^{z_n} r\left(1+\left(\frac{dr}{dz}\right)^2\right) dz$$

Similarly,

$$V_i = \int_{z_i}^{z_{i+1}} \pi r^2 dz, \qquad \text{giving}$$

$$V_s = \pi \int_{z_0}^{z_n} r^2 dz$$

Here both integrals must be evaluated by going right round the boundary.

<u>Simple Approach - Trapezoidal Rule</u>

(a) In the Interval $z_i \leq z \leq z_{i+1}$, take r as a linear function of z, then

$$r = \frac{(r_i z_{i+1} - r_{i+1} z_i) + z(r_{i+1} - r_i)}{z_{i+1} - z_i}$$

and $$\frac{dr}{dz} = \frac{r_{i+1} - r_i}{z_{i+1} - z_i}$$

Thus $$A_i = 2\pi c_i \int_{z_i}^{z_{i+1}} (a_i + b_i z) dz$$

where $$c_i = \left(1 + \left(\frac{r_{i+1} - r_i}{z_{i+1} - z_i}\right)^2\right)^{\frac{1}{2}}$$

$$a_i = \frac{(r_i z_{i+1} - r_{i+1} z_i)}{z_{i+1} - z_i}$$

$$b_i = \frac{(r_{i+1} - r_i)}{z_{i+1} - z_i}$$

Therefore

$$A_i = 2\pi c_i \left| a_i z + \tfrac{1}{2} b_i z^2 \right|_{z_i}^{z_{i+1}}$$

$$= \pi c_i (r_{i+1} + r_i)(z_{i+1} - z_i)$$

Now the total surface area, A_s, becomes

$$A_s = \sum_{i=0}^{n-1} \pi (r_{i+1} + r_i)((z_{i+1} - z_i)^2 + (r_{i+1} - r_i)^2)^{\frac{1}{2}}$$

where we take $|z_{i+1} - z_i|$ to ensure that the re-entrant points of the surface are handled properly.

(b) For volume, we take r^2 as a linear function of z.

i.e. $$\frac{r^2 - r_i^2}{r_{i+1}^2 - r_i^2} = \frac{z - z_i}{z_{i+1} - z_i}$$

Since $$z_{i+1} - z = z - z_i$$

Therefore $$r^2 = \frac{(r_i^2 z_{i+1} - r_{i+1}^2 z_i) + z(r_{i+1}^2 - r_i^2)}{z_{i+1} - z_i}$$

But $$V_i = \pi \int_{z_i}^{z_{i+1}} r^2 dz ,$$ therefore,

$$V_i = \frac{\pi}{2} (r_{i+1}^2 + r_i)(z_{i+1} - z_i)$$

Then the total volume of the drop is given by,

$$V_d = \frac{\pi}{2} \sum_{i=0}^{n-1} (r_{i+1}^2 + r_i^2)(z_{i+1} - z_i)$$

Similarly, this equation takes care of the re-entrant part. To write it in a different form,

$$V_d = \frac{\pi}{2}\left\{r_n^2 z_n - r_0^2 z_0 + \sum_{i=0}^{n-1} (r_i{}^2 z_{i+1} - r_{i+1}{}^2 z_i)\right\}$$

i.e. $$V_d = \frac{\pi}{2}\sum_{i=0}^{n-1}(r_i{}^2 z_{i+1} - r_{i+1}{}^2 z_i)$$

Since $r_0 = r_n = 0$

(c) The trapezoidal rule will underestimate the surface area slightly due to the truncations. The error can be estimated by assuming the surface is spherical in each interval. In this case,

$$r_i{}^2 + (z_i - c_i)^2 = r_{i+1}{}^2 + (z_{i+1} - c_i)^2 = a_i^2$$

where the spherical element has radius a_i and centre c_i. Therefore,

$$c_i = \frac{r_i{}^2 + r_{i+1}{}^2 + z_i{}^2 - z_{i+1}{}^2}{2(z_i - z_{i+1})}, \qquad \text{hence, } a_i.$$

The trapezoidal rule can be reworked if required.

(d) The attached program will do these calculations. First input data with z_i and r_i should be printed on each card.

Nothing should be printed on the first and last cards, and then everything will take care of itself.

```
C         SURFACE AREA AND VOLUME OF DROP
C         GIVEN POINTS ON BOUNDARY

100       FORMAT (2F 10.5)
110       FORMAT (///5X, 'AREA OF DROP =  ',
                 E 15.5/5X, 'VOLUME OF DROP = ', E 15.5)

1         READ (5,100) Z1
          IF (Z1 . LT 0.0001) STOP
          A  =  0
          R1 =  0
          V  =  0
2         READ (5,100) Z2, R2
          A  =  A + (R1 + R2)* SQRT((Z2 - Z1)**2
                + (R2 - R1)**2)
          V  =  V + R1 * R1 * Z2 - R2 * R2 * Z1
          IF (R2 . GT . 0.0001) GO TO 2
C         OUTPUT ANSWER
          A  =  3.14159265 * A
          V  =  1.57079632 * V
          WRITE (6,110) A,V
          GO TO 1
          END
```

APPENDIX E(a). Evaluation of Limits

$$\lim_{e\to 0} K_3^b = \lim_{e\to 0}\left\{\frac{1}{e^3}\sin^{-1}e - \frac{1}{e^2}\sqrt{1-e^2}\right\}$$

$$= \lim_{e\to 0}\left\{\frac{1}{e^3}\left(e + \frac{e^3}{6} + \frac{1}{2}\cdot\frac{3}{4}\cdot\frac{e^5}{5} + \ldots\ldots\right)\right.$$

$$\left. - \frac{1}{e^2}\left(1 - \frac{e^2}{2} - \frac{e^4}{8}\ldots\ldots\right)\right\}$$

$$= \lim_{e\to 0}\left\{\cancel{\frac{1}{e^2}} + \frac{1}{6} + \frac{3e^2}{40} + \ldots\ldots\right.$$

$$\left. - \cancel{\frac{1}{e^2}} + \frac{1}{2} + \frac{e^2}{8}\ldots\ldots\right\}$$

$$= \frac{1}{6} + \frac{3}{6}$$

$$= \frac{2}{3}$$

APPENDIX E(b). Evaluation of Limits

$$\lim_{e\to 0} K_3^a = \lim_{e\to 0} \left\{ \frac{\sqrt[4]{1-e^2}}{e^3} \sin^{-1} e - \frac{4}{3}\frac{\sqrt{1-e^2}}{e^2} \right\}$$

$$= \lim_{e\to 0} \left\{ \frac{1}{e^3} \left(1 - \frac{e^2}{2} - \frac{e^4}{8} - \ldots\ldots\right)\left(e + \frac{e^3}{6} + \frac{3e^5}{40} + \ldots\ldots\right)\right.$$

$$\left. - \frac{1}{2} - 1 \right\}$$

$$= \lim_{e\to 0} \left\{ \frac{1}{e^3} \left(e + \frac{e^3}{6} + \frac{3e^5}{40} - \frac{e^3}{2} - \frac{e^5}{12} - \frac{3e^7}{80} + \frac{e^5}{8}\right.\right.$$

$$\left.\left. + \frac{e^7}{48} + \frac{3e^9}{320} + \ldots\ldots\right) - \frac{1}{e^2} + 1 \right\}$$

$$= \lim_{e\to 0} \left\{ \frac{1}{\cancel{e^2}} + \frac{1}{6} + \frac{3e^2}{40} - \frac{1}{2} - \frac{e^2}{2} + \ldots\ldots\right.$$

$$\left. - \frac{1}{\cancel{e^2}} + 1 \right\}$$

$$= \frac{1}{6} - \frac{1}{2} + 1 = 2/3$$

The values of K_3^b and k_3^a for various values of e are tabulated in Table E. The graphical representation is also included.

TABLE E. Variation of K_3^a and K_3^b with Eccentricity, e

No.	Eccentricity, e=c/a	K_3^b	K_3^a
1	0.01	0.667	0.667
2	0.1	0.669	0.665
3	0.2	0.675	0.661
4	0.3	0.686	0.654
5	0.4	0.702	0.643
6	0.5	0.725	0.628
7	0.6	0.757	0.606
8	0.7	0.803	0.574
9	0.8	0.874	0.524
10	0.9	0.998	0.435
11	1.0	1.571	0.000

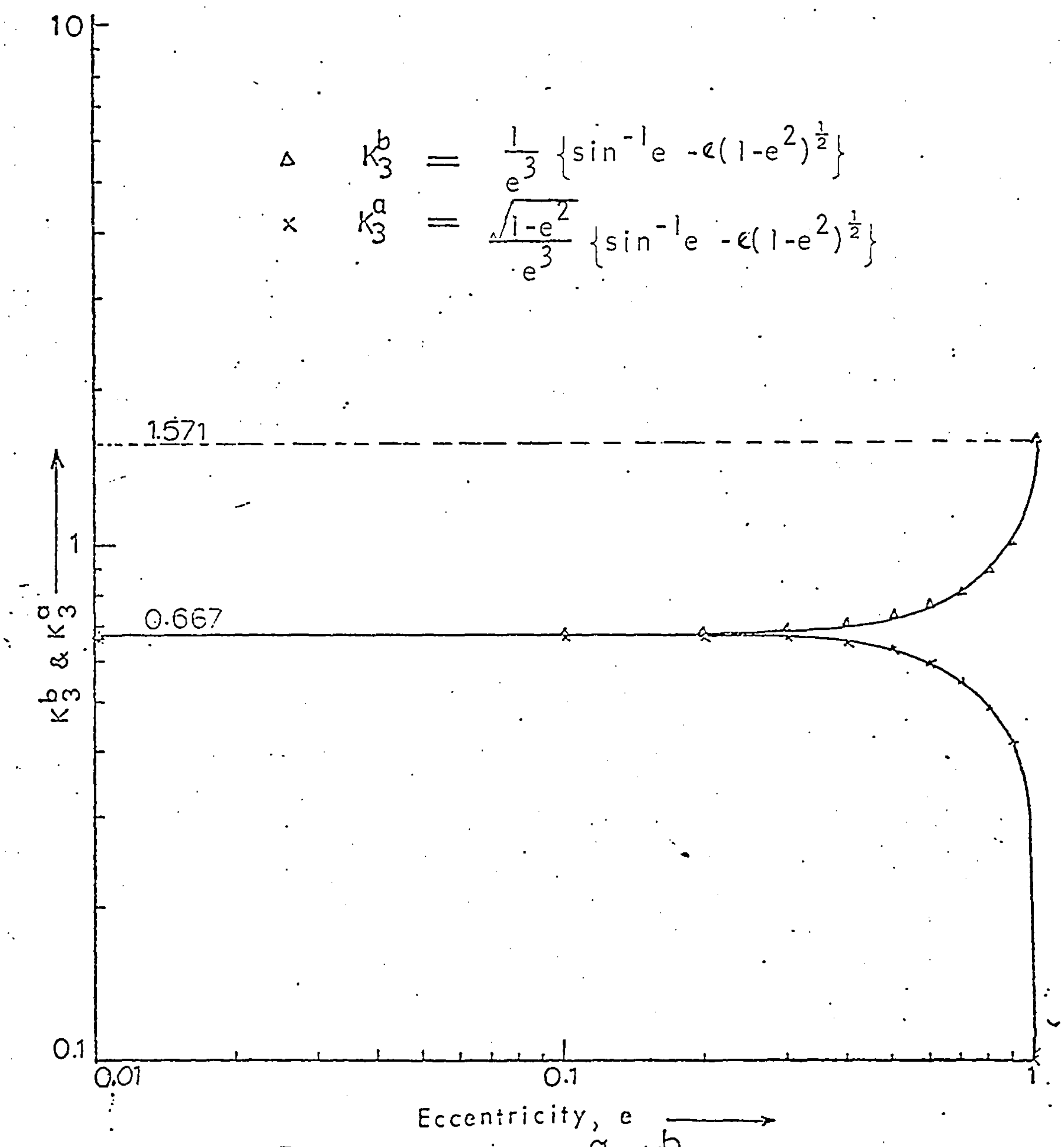

Dependence of K_3^a & K_3^b on e

APPENDIX F. Derivation of Equation for Tangential Velocity, U_F, used in Section 6.3

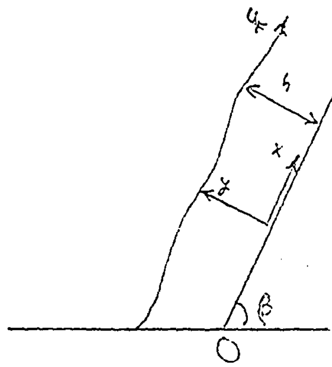

Fig. A

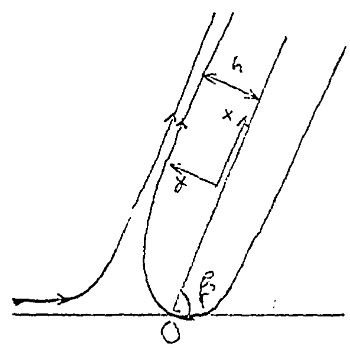

Fig. B

The formation of a skirt is an interesting case where both the surface tension and the viscosity play an important part. As it is shown above, Figure A and B, a skirt can be considered to behave like a thin liquid film flowing with velocity U_x at the interface. β is the angle of inclination to the horizontal. Three different regimes have been observed experimentally;

- i At low Reynolds numbers for a given system, the skirt is curved.
- ii At intermediate Reynolds numbers for a given system, the wave regime appears.
- iii Turbulent regime where the motion becomes unsteady.

We will restrict ourselves to case (i) where creeping flow assumptions can be applied. Also, we will assume that the skirt is so thin that the rate of change of velocity across half the skirt is much larger compared to that along it. Thus $\frac{\partial u_x}{\partial y} \gg \frac{\partial u_x}{\partial x}$ and $\frac{\partial^2 u_x}{\partial x^2}$ can be neglected with respect to $\frac{\partial^2 u_y}{\partial y^2}$.

The Navier-Stokes equations in Cartesian coordinates:

x-component:

$$\frac{\partial u_x}{\partial t} + u_x \frac{\partial u_x}{\partial x} + u_y \frac{\partial u_x}{\partial y} = -\frac{1}{\rho}\frac{\partial P}{\partial x} + \nu \frac{\partial^2 u_x}{\partial y^2} + \tilde{\pi} \qquad (1)$$

where $\tilde{\pi}$ is the body force per unit mass in the x-direction.

y-component:

$$\frac{\partial P}{\partial y} = 0 \qquad (2)$$

Continuity Equation:

$$\frac{\partial u_x}{\partial x} + \frac{\partial u_y}{\partial y} = 0 \qquad (3)$$

Boundary conditions:

$$u_x = u_y = 0 \quad \text{at} \quad y = 0 \qquad (4)$$

$$P = P_\sigma + F_1 \quad \text{at} \quad y = h(x) \qquad (5)$$

$$\mu \frac{\partial u_x}{\partial y} = F_2 \quad \text{at} \quad y = h(x) \tag{6}$$

In addition, we will assume that the difference between the normal and shear stress, F_1 and F_2 is small so that $F_1 \doteq F_2 \doteq F$. This assumption is arbitrary but is adopted for want of any better approach. Putting (5) into (1), we obtain

$$\frac{\partial u_x}{\partial t} + u_x \frac{\partial u_x}{\partial x} + u_y \frac{\partial u_x}{\partial y} = -\frac{1}{\rho}\frac{\partial}{\partial x}(P_\sigma + F) + \nu \frac{\partial^2 u_x}{\partial y^2} + \pi$$

.....(7)

For a thin skirt (Levich p.376), P_σ can be approximated by $-\sigma \frac{a^2 h}{\partial x^2}$ neglecting the second radii of curvature. Then (7) takes the form,

$$\frac{\partial u_x}{\partial t} + u_x \frac{\partial u_x}{\partial x} + u_y \frac{\partial u_x}{\partial y} = \frac{\sigma}{\rho}\frac{\partial^3 h}{\partial x^3} + \frac{\partial^2 u_x}{\partial y^2} + \pi \tag{8}$$

where h is the surface coordinate related to u_y by,

$$u_y = \frac{\partial h}{\partial t} + \frac{\partial h}{\partial x}\frac{ax}{at} = \frac{\partial h}{\partial t} + u_x \frac{\partial h}{\partial x} \doteq \frac{\partial h}{\partial t} \tag{9}$$

and to u_x by,

$$\frac{\partial h}{\partial t} = -\frac{\partial}{\partial x}\left(\int u_x d_y\right) \tag{10}$$

On substituting (9) and (10) into (8), we obtain,

$$\frac{\partial u_x}{\partial t} + u_x \frac{\partial u_x}{\partial x} - \left(\int \frac{\partial u_x}{\partial x}\, dy\right) \frac{\partial u_y}{\partial y} = \frac{\sigma}{\rho} \frac{\partial^3 h}{\partial x^3} + \frac{\partial^2 u_x}{\partial y^2} + \pi \qquad (11)$$

Equation (11) is a general equation of motion of liquid at the interface of a thin skirt. For a slow steady motion on which a constant normal stress,

$$F = \frac{\mu}{z}\left(\frac{\Delta\rho}{\rho} g \frac{V}{A} \sin\beta\right)^{\frac{1}{2}} *,$$

Dombrowski (1954), is acting on the skirt/wake interface, and there are no body forces, Equation (11) reduces to,

$$\frac{\partial^2 u_x}{\partial y^2} = 0 \qquad (12)$$

Integrating with boundary conditions (4) and (6) we obtain for u_F,

$$u_F = \frac{y}{z}\left(\frac{\Delta\rho}{\rho} g \frac{V}{A} \sin\beta\right)^{\frac{1}{2}} \qquad (13)$$

---

* This is an empirical correlation based on an equation given by Dombrowski (1954). No theoretical derivation of this equation has been given, but it has been found to work, at least in Dombrowski's case.